Research in Optoelectronics (A)

2021 Reprints of

Professor Larry A. Coldren

and Collaborators

ECE Technical Report 22-01

Department of Electrical & Computer Engineering
University of California, Santa Barbara

Heterogeneously Integrated O-band SG-DBR Lasers for Short Reach Analog Coherent Links

Stephen Misak[1*], Aaron Maharry[1], Junqian Liu[1], Ranjeet Kumar[2], Duanni Huang[2], Giovanni Gilardi[2], Richard Jones[2], Ansheng Liu[2], Larry Coldren[1], Clint Schow[1]
[1]*Department of Electrical and Computer Engineering, University of California, Santa Barbara, CA 93106, United States*
[2]*Intel Corporation, 2200 Mission College Blvd, Santa Clara, CA 95054, United States*
**smisak@ucsb.edu*

Abstract: We report record performance for a heterogeneously integrated O-band SG-DBR laser, achieving a tuning range of 48 nm, 50 dB MSR, >20 mW output power, and ~0.67 MHz apparent linewidth.

1. Introduction

Tunable lasers have applications in multiple areas, but this paper focuses on short reach, intra-datacenter communications. Intra-datacenter link performance is key because it accounts for over 70% of datacenter traffic [1]. Analog coherent links are generating interest to improve speed and reduce power consumption. The lasers in this paper are designed to act as the local oscillator (LO) for analog coherent links. An optical phase-locked loop (OPLL) is used in analog coherent links to frequency- and phase-lock the LO to the transmitter laser. This is accomplished by modulating a diode in the laser cavity with an error signal generated by feeding part of the received data signal through a Costas loop phase/frequency detector and loop filter. A diode phase section with sufficient bandwidth and tuning efficiency is required to maintain phase locking [2,3]. For fabricating the laser, the silicon photonics platform is advantageous for its large-scale manufacturability, reduced cost, and integration capabilities [4,5]. While silicon does not have a native light source, wafer bonding of III-V on silicon has matured, enabling high performance lasers on silicon and a large variety of photonic integrated circuits (PICs) to be manufactured at scale [6,7].

2. Device Design

Using Intel's silicon photonics platform, several sampled grating distributed Bragg reflector (SG-DBR) laser variants were designed. Fig. 1 shows the fabricated lasers and a design schematic. The gratings were designed to maximize output power with a low threshold and high mode suppression ratio (MSR). For high front output power, the front gratings were designed with low reflectivity by reducing the number of periods (Λ) per grating burst ($Z_1 = n\Lambda$) and the number of bursts. A long, high reflectivity back mirror was used for high MSR and low threshold. The cavity length needs to be optimized such that the phase section provides several GHz of tuning for frequency locking using the OPLL. To examine the impact on MSR, threshold, tuning efficiency, and output power, multiple grating designs and phase section lengths were fabricated.

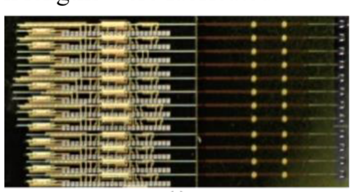

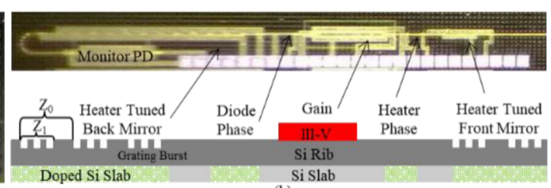

Fig. 1. (a) The full array of laser variants is shown. (b) A schematic view of the laser shows the details for the SG-DBR devices.

3. Measurement Results

For all measurements, a thermo-electric cooler is used for temperature stability, and a probe card is used for biasing. For one variant, labeled Design A, a tuning range of 48 nm (1273 to 1321 nm) and MSR of 50 dB, as shown in Fig 2, were measured by sweeping the voltage for the front and back mirror heaters while measuring a fraction of the output power with an optical spectrum analyzer (OSA). The low MSR band in Fig 2(b) is likely due to reduced gain, supported by the lower spontaneous emission at longer wavelengths in Fig. 2(c). Output power shown in Fig. 2(d) is measured using an integrating sphere with a power meter. The output power and threshold worsen as the wavelength increases, but >20 mW of power is achieved from 1280 to 1315 nm. To the author's best knowledge, this is a record for O-band SG-DBR lasers on silicon, and it is comparable to other O-band widely tunable lasers [8,9]. Although the laser has a large tuning range, Fig. 2 shows that continuous tuning is only achieved in a 1 to 3 nm range around each SG-DBR supermode, not across the entire tuning range. By sweeping the diode phase section current, tuning efficiency was

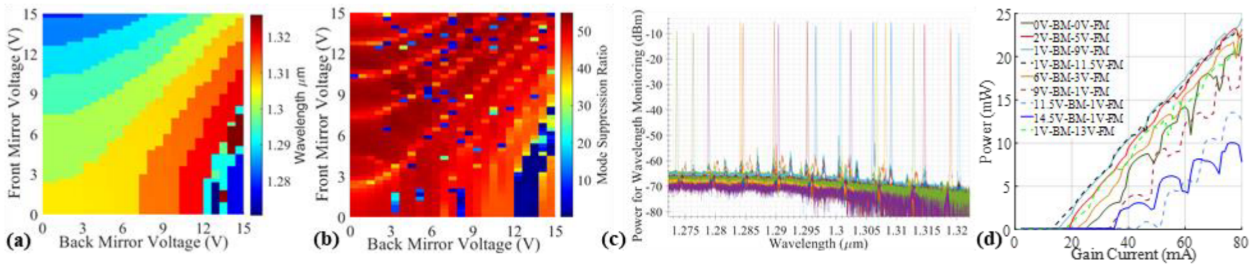

Fig. 2. For Design A, (a) wavelength map (b) MSR, (c) spectra, and (d) output power are measured at 20˚C

measured using an OSA as shown in Fig 3. The 400 µm length for Design A provides up to 0.75 GHz/mA tuning compared to 0.32 GHz/mA for the 200 µm length in Design B. The decrease in tuning efficiency at higher currents is likely caused by Joule heating. Using a delayed self-heterodyne (DSH) setup with a 25 km fiber delay and a 200 MHz acousto-optic modulator, a linewidth (LW) of ~ 0.67 MHz (broadened by flicker and other technical noise) was fitted for Design A. The frequency response of the diode phase tuner was measured by converting the optical frequency modulation to amplitude modulation (AM) using the edge of a bandpass optical filter. A photoreceiver connected to an electrical spectrum analyzer was used to measure the frequency response of the AM signal, yielding a ~100 MHz 3-dB BW, sufficient for operation in the analog coherent OPLL.

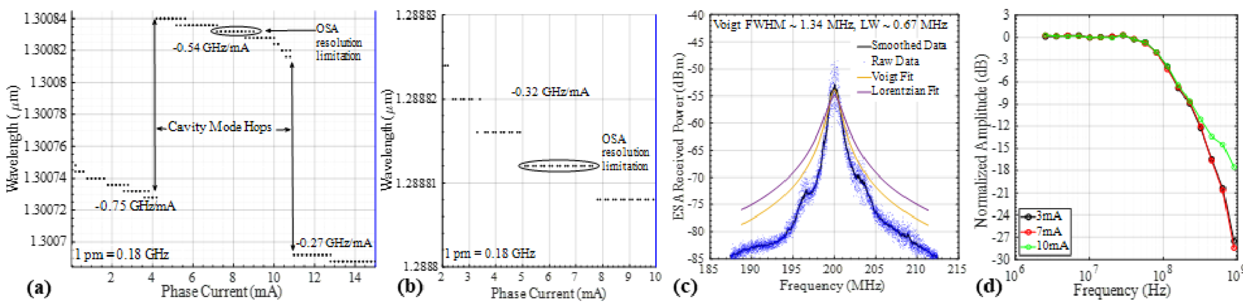

Fig. 3. Tuning efficiency is larger for (a) Design A compared to (b) Design B. Apparent LW (c) of Design A is ~0.67 MHz. (d) Diode phase tuner frequency response shows ~100 MHz 3-dB BW.

4. Conclusion

Record performance has been measured for heterogeneously integrated SG-DBR lasers with wavelengths from 1273 to 1321 nm and >20 mW of output power. A phase tuning efficiency of up to 0.75 GHz/mA is shown with ~100 MHz 3-dB BW. Spectral quality is demonstrated with 50 dB of MSR at most bias conditions and a DSH LW of ~0.67 MHz. This performance is adequate for integration into an analog coherent link with an OPLL.

5. Acknowledgements

The information, data, or work presented herein was funded in part by the Advanced Research Projects Agency-Energy (ARPA-E), U.S. Department of Energy, under Award Number DE-AR0000848. The views and opinions of authors expressed herein do not necessarily state or reflect those of the United States Government or any agency thereof. Thanks to Intel Silicon Photonics and Intel Labs for assistance with design and to Intel F11X for fabrication.

6. References

[1] White Paper: "Cisco 2020 Global Networking Trends Report," available: https://www.cisco.com/c/dam/m/en_us/solutions/enterprise-networks/networking-report/files/GLBL-ENG_NB-06_0_NA_RPT_PDF_MOFU-no-NetworkingTrendsReport-NB_rpten018612_5.pdf

[2] T. Hirokawa et al., "Analog Coherent Detection for Energy Efficient Intra-Data Center Links at 200 Gbps Per Wavelength," J. Lightwave Technol. **39**(2), 520-531 (2021).

[3] J. K. Perin, A. Shastri and J. M. Kahn, "Design of Low-Power DSP-Free Coherent Receivers for Data Center Links," J. Lightwave Technol. **35**(21), 4650-4662 (2017)

[4] R. Blum, "Silicon Photonics – The Key to Data Centre Connectivity", Optical Connections, Issue 10, Q3-2017

[5] C. Doerr and L. Chen, "Silicon Photonics in Optical Coherent Systems," Proc. of the IEEE **106**(12), 2291-2301 (2018).

[6] H. Park et al, "Hybrid Silicon evanescent laser fabricated with a Silicon waveguide and III-V offset quantum wells," Opt. Exp. **13**(23), 9460-9464 (2005).

[7] T. Komljenovic, D. Huang, P. Pintus, M. A. Tran, M. L. Davenport and J. E. Bowers, "Photonic Integrated Circuits Using Heterogeneous Integration on Silicon," Proc. of the IEEE **106**(12), 2246-2257 (2018)

[8] H. Duprez, C. Jany, C. Seassal, and B. Ben Bakir, "Highly tunable heterogeneously integrated III-V on silicon sampled-grating distributed Bragg reflector lasers operating in the O-band," Opt. Express **24**, 20895-20903 (2016).

[9] Aditya Malik, Joel Guo, Minh A. Tran, Geza Kurczveil, Di Liang, and John E. Bowers, "Widely tunable, heterogeneously integrated quantum-dot O-band lasers on silicon," Photon. Res. **8**, 1551-1557 (2020)

Dual Laser Indium Phosphide Photonic Integrated Circuit for Integrated Path Differential Absorption Lidar

Joseph Fridlander, Fengqiao Sang, Victoria Rosborough, Fabrizio Gambini, Simone Tommaso Šuran-Brunelli, Jeffrey R. Chen, Kenji Numata, Mark Stephen, Larry A. Coldren, *Life Fellow, IEEE*, and Jonathan Klamkin, *Senior Member, IEEE*

***Abstract*—An indium phosphide photonic integrated circuit (PIC) was demonstrated for integrated path differential absorption lidar of atmospheric carbon dioxide (CO_2). The PIC consists of two widely tunable sampled grating distributed Bragg reflector (SGDBR) lasers, directional couplers, a phase modulator, a photodiode, and semiconductor optical amplifiers (SOAs). One SGDBR laser, the leader, is locked to the center of an absorption line at 1572.335 nm using the on-chip phase modulator and a bench-top CO_2 Herriott reference cell. The other SGDBR laser, the follower, is stepped in frequency over ±15 GHz around 1572.335 nm to scan the target CO_2 absorption line. The follower laser is offset locked to the leader laser with an optical phase lock loop. An SOA after the follower laser generates a pulse at each frequency step to create a train of pulses that samples the target CO_2 absorption line. The PIC components and subsystem are characterized and evaluated based on target performance requirements. The leader laser demonstrated a 236-fold improvement in frequency stability standard deviation when locked compared to free running and the follower laser frequency stability standard deviation compared to the leader laser was 37.6 KHz at a 2 GHz programmed offset.**

***Index Terms*—indium phosphide, lidar, photonic integrated circuits, remote sensing, semiconductor lasers, spectroscopy**

I. Introduction

PRECISE and accurate remote sensing of atmospheric gases requires spectroscopy instruments with on-board lasers. Current passive instruments in orbit, such as the Orbiting Carbon Observatory 3 (OCO-3), rely on reflected sunlight to capture absorption information and do not provide adequate spatial and temporal coverage for future mission specifications [1]. A system developed at Goddard Space Flight Center (GSFC) for NASA's Active Sensing of CO_2 Emissions over Nights, Days, and Seasons (ASCENDS) mission is based on an integrated path differential absorption (IPDA) lidar architecture to measure CO_2 concentrations to approximately 1 ppm precision [2-5]. The system, assembled from commercial off-the-shelf (COTS) components, has been verified through airborne campaigns [6-8].

IPDA lidar measures the optical absorption of a target species using multiple wavelengths of laser light that propagate to a reflective surface and return. By probing with multiple wavelengths on and off the absorption line of interest, the shape of the line is mapped. The initial GSFC lidar system developed for ASCENDS probes the 1572.335 nm absorption line of CO_2. This relatively weak absorption line enables sufficient return signal and can leverage mature L-band optical components developed for the telecommunications industry.

There is growing interest to deploy systems based on photonic integrated circuits (PICs) in space-based communication and remote sensing applications [9-19]. Spaceborne laser instruments are extremely complex optical systems that are costly, bulky, and power hungry. PICs, on the other hand, allow integration of the required optical functions on a single chip. Furthermore, a variety of integration platforms, materials, and devices exist that allow a high degree of flexibility to meet stringent specifications.

Therefore, PIC technology can significantly reduce system cost, size, weight, and power (CSWaP). Improved reliability is also expected due to the reduced number of fiber connections between components and the significant reduction in mass. A PIC and its closely packaged control electronics could be contained in a single ruggedized module enabling deployment on small space platforms.

In this work, a PIC designed to integrate all the photonic components for an IPDA CO_2 lidar system is presented. The PIC consists of two tunable lasers, directional couplers, a phase modulator, a photodiode, and semiconductor optical amplifiers (SOAs). The PIC is fabricated on an indium

Manuscript received March 31, 2021. This work was supported by the NASA ROSES Advanced Component Technology Program. J. Fridlander, F. Sang, V. Rosborough contributed equally to this work.

J. Fridlander, F. Sang, V. Rosborough, S. T. S. Brunelli. L. Coldren, and J. Klamkin are with the Department of Electrical and Computer Engineering, University of California Santa Barbara, Santa Barbara, CA 93106 USA (email: jfridlander@ucsb.edu; fsang@ucsb.edu; rosborough@ucsb.edu; ssuranbrunelli@ucsb.edu; coldren@ucsb.edu; klamkin@ucsb.edu).

F. Gambini was with the Department of Electrical and Computer Engineering, University of California Santa Barbara, Santa Barbara, CA 93106 USA. He is currently with the University of Maryland Baltimore County, Baltimore, MD 21250 USA and NASA Goddard Space Flight Center/CRESST II, Greenbelt, MD 20771 USA (email: fabrizio.gambini@nasa.gov).

J. R. Chen, K. Numata, and M. Stephen are with NASA Goddard Space Flight Center, Greenbelt, MD 20771 USA (email: jeffrey.r.chen@nasa.gov; kenji.numata-1@nasa.gov; mark.a.stephen@nasa.gov).

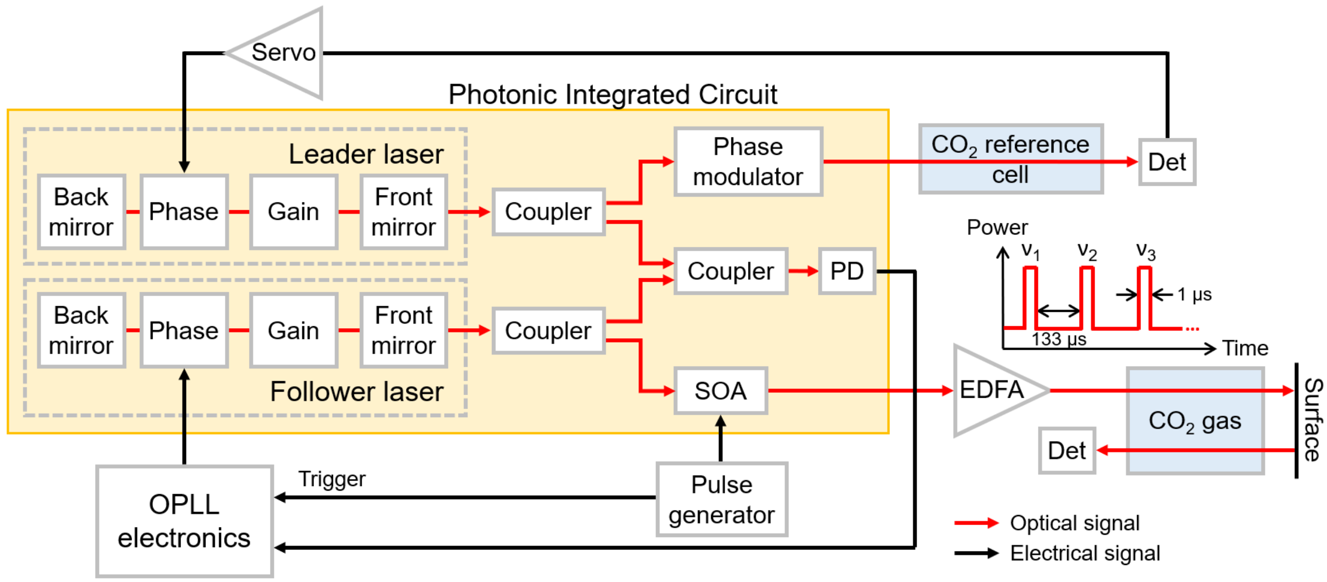

Fig. 1. PIC architecture and concept for IPDA lidar system. The SGDBR leader laser is stabilized to 1572.335 nm using a frequency modulation technique. The SGDBR follower laser is offset locked to the leader laser with an OPLL. A pulse is generated at each follower laser wavelength step resulting in a train of pulses at ν_1, ν_2, ν_3, etc. Through repeated scans, the amplified pulse train maps the CO_2 absorption line shape. Det: detector; EDFA: erbium-doped fiber amplifier.

phosphide (InP) platform that enables inclusion of active components, such as lasers and amplifiers, along with passive components, such as directional couplers. InP PICs were developed for telecommunications applications and have recently been pursued for other applications including free space laser communications and 3D mapping lidar [9-11]. This platform is ideally suited for IPDA lidar systems that require high performance tunable lasers.

II. Lidar System Architecture

A. Integrated Path Differential Absorption Lidar Operation

The lidar architecture and operation is illustrated in Fig. 1. A leader laser is locked to the 1572.335 nm CO_2 absorption line using a frequency modulation technique similar to Pound-Drever-Hall stabilization [20]. The integrated leader laser is a multi-section sampled grating distributed Bragg reflector (SGDBR) laser designed for emission near 1572 nm. A directional coupler designed for an 80/20 splitting ratio routes most of the leader laser light to a phase modulator operated at 125 MHz and with modulation depth of π radians. The phase modulated light is coupled to a CO_2 Herriott gas cell that serves as an absolute wavelength reference. Side bands generated by the phase modulator experience different absorption and dispersion due to the shape of the absorption line. Phase sensitive detection of a beat note at the output of the reference cell generates a frequency-discriminating error signal. The filtered error signal is then applied to the phase section of the leader laser to maintain the center wavelength.

To sample at multiple wavelengths, a follower SGDBR laser is offset-locked to the leader laser via an optical phase lock loop (OPLL). The follower laser is stepped along several sampling points over ±15 GHz in frequency around 1572.335 nm. The directional couplers that follow the leader and follower lasers direct a portion of their light to an integrated high-speed photodiode. The detected beat note between the leader and follower lasers is processed by the OPLL electronics. The OPLL charge pump output is filtered and fed to the phase section of the follower laser for stabilization at each programmed offset wavelength.

After the follower laser steps to a new wavelength, the SOA at the output is driven by a pulse generator to produce a 1 µs pulse. Communication between the pulse generator and OPLL electronics coordinates the triggering of the pulse. The pulses are separated by 133 µs to prevent crosstalk between wavelengths due to cloud scattering.

TABLE I
PIC Performance Metrics for Lidar System

Parameter	Target Value
Center wavelength	1572.335 nm
Side-mode suppression ratio	40 dB
Linewidth (1 µs)	<50 MHz
Center wavelength drift (1 s)	<100 MHz
Center wavelength standard deviation	<3 MHz
Follower laser wavelength tuning	±15 GHz
Pulse width	1 µs
Repetition rate	7.5 kHz
Pulse extinction ratio	35 dB
Peak output power	10 mW

Target performance specification derivations can be found in [2-5].

B. Photonic Components and Design

Table 1 lists key performance metrics that the PIC components and subsystem must satisfy for the IPDA CO_2 lidar. As described, an InP material platform was chosen for the PIC due to its maturity and ability to integrate high performance tunable lasers with other active components and with passive components. An SGDBR laser design was

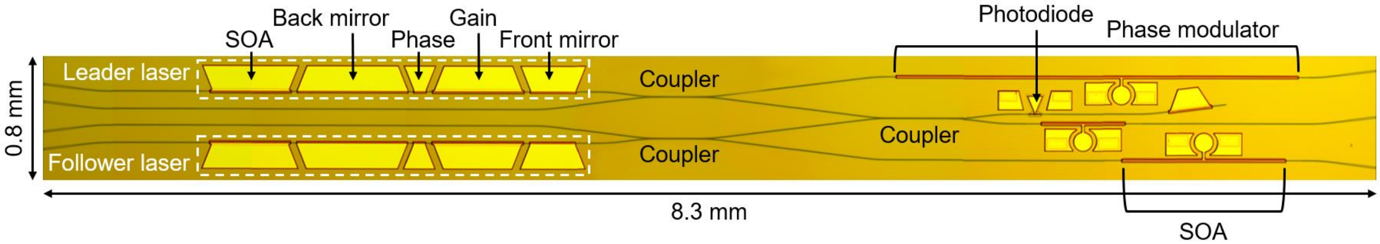

Fig. 2. Microscope image of fabricated PIC.

selected for the leader and follower lasers because of its wide continuous wavelength tunability (approximately 40 nm) and multi-section format that enables various locking approaches. Large changes in wavelength are achieved by injecting current into the front and back mirror sections of the SGDBR laser, while the phase section makes fine wavelength adjustments using electronic feedback. The tunability of these lasers makes them tolerant to fabrication variations for an application requiring a precise wavelength target. Furthermore, InP SGDBR lasers have been demonstrated to have sufficient linewidth and side mode suppression ratio (SMSR) to meet the specifications reported in Table 1 [10].

Directional couplers were selected over multimode interference (MMI) couplers in order to control the fraction of light tapped from the lasers for the OPLL photodiode. Additionally, MMI couplers can produce undesirable reflections that may have impacted system performance. The directional couplers were designed to have 2 μm wide waveguides with a 1 μm gap in between. To enable sufficient power output for coupling to the CO_2 reference cell and for sufficient peak pulse power, about 80% of the light from the leader and follower lasers was routed to the phase modulator and SOA, respectively. To achieve 80% power at the through port, the length of the directional couplers was chosen to be 180 μm based on simulations in Lumerical using an eigenmode expansion method.

An SOA was chosen for encoding pulses to maximize the pulse extinction ratio (ER) and peak power. While high ER has been demonstrated with electro-absorption modulators in InP, they exhibit significant insertion loss. It is difficult to reach an ER of 35 dB using an InP Mach-Zehnder phase modulator (MZM), another alternative, and they also add some insertion loss. Since the repetition rate for the lidar system is low and the pulses are wide, current injection into an SOA is sufficiently fast.

III. Integration Platform and Fabrication

A microscope image of the fabricated PIC, comprised of the leader and follower SGDBR lasers, directional couplers, phase modulator, photodiode, and SOAs, is shown in Fig. 2. PICs were fabricated using an offset quantum well (OQW) platform [21]. A sideview cross section describing this platform is illustrated in the top of Fig. 3. The initial epitaxial structure was grown using metalorganic chemical vapor deposition (MOCVD) on an n-doped InP substrate. Following growth of an n-type buffer, a 350-nm thick indium gallium arsenide phosphide (InGaAsP) waveguide layer followed by an InGaAsP multi-quantum well (MQW) structure with seven quantum wells (QWs) is grown. The compressively strained quantum wells were designed for emission near 1565 nm.

The passive sections (used for the laser mirrors, phase section, phase modulator, and passive routing and coupling) are formed by selectively etching the QWs. Next, the gratings forming the laser mirrors are etched into the waveguide layer. The scanning electron microscope (SEM) image in Fig. 3(a) shows the etched gratings, which are patterned using electron

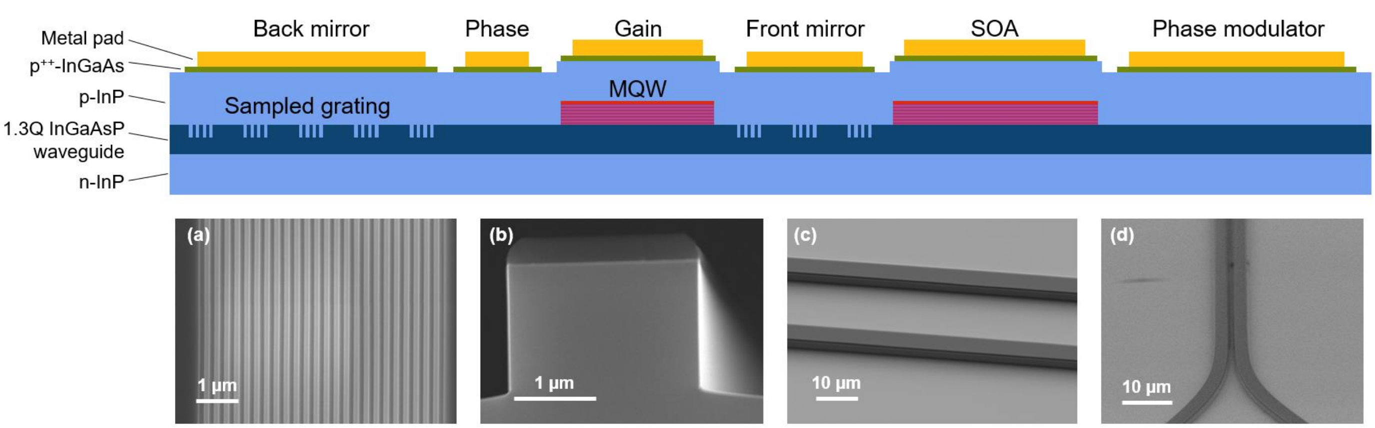

Fig. 3. Top: Sideview cross section of the OQW integration platform. Active-passive integration is accomplished by selectively etching the QWs to form passive regions. The laser mirror gratings are etched into the waveguide core layer. This is followed by a p-cladding and p-contact layer regrowth, ridge formation, and metal contact formation. Bottom: SEM images of (a) etched laser mirror gratings, (b) a ridge waveguide cross section, (c) two parallel passive ridge waveguides, and (d) a directional coupler.

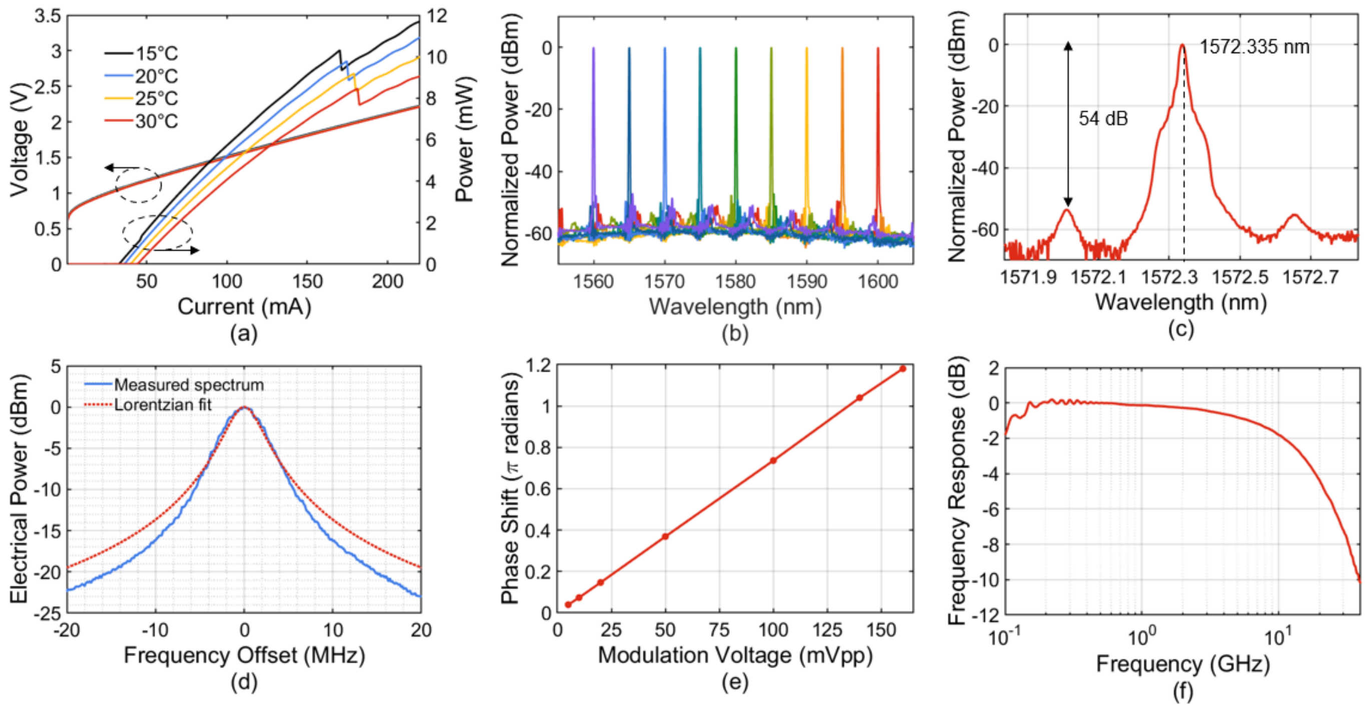

Fig. 4. (a) LIV characteristics of follower laser for varying TEC temperatures. (b) Overlaid laser spectra showing a 40 nm tuning range. (c) Leader laser spectrum when tuned to 1572.335 nm and demonstrating a SMSR of 54 dB. (d) Delayed self-heterodyne beat note demonstrating 2.1 MHz 3-dB linewidth. The resolution bandwidth was 3 MHz and the sweep time was 5 ms. (e) Phase modulator efficiency for a bias of 25 mA. (f) Example integrated photodiode normalized frequency response measurement demonstrating 15 GHz 3-dB bandwidth.

beam lithography. This is followed by an MOCVD regrowth to form the p-InP cladding and p-indium gallium arsenide (InGaAs) contact layer. Ridge waveguides are then formed with a combination of dry and wet etching. Figure 3(b) shows an SEM cross section image of a ridge structure. Figure 3(c) shows an image of two passive waveguide ridges and Fig. 3(d) shows the output of a directional coupler.

Following ridge formation, the p-InGaAs contact layer is selectively removed between devices to provide some electrical isolation. While not implemented for the PIC in this work, further electrical isolation can be achieved via proton implantation of the waveguide ridge between devices. Vias are then etched and p-metal contacts and pads are deposited. Finally, the wafer is thinned to approximately 150 µm, backside contacts are deposited and annealed, PICs are cleaved for separation and to form facets, and anti-reflection coatings are applied to these facets.

IV. PIC Component Characterization

A. Widely Tunable Laser

The leader and follower lasers are both widely tunable SGDBR lasers designed for emission near 1572 nm. The back mirror consists of twelve 6.1 µm long grating bursts with a sampling period of 61.34 µm. The front mirror consists of five 4.15 µm long bursts with a sampling period of 68.71 µm. The grating period for both the back and front mirrors is 244 nm and the continuous grating coupling coefficient, κ, is 368.2 cm^{-1}. A 500 µm long SOA behind the back mirror can be reverse biased to absorb light and serve as a monitor for light emitted from the back of the laser or it can be operated in forward bias to amplify light emitted from the back mirror and couple it off-chip. The gain section of the laser is 550 µm long and the phase section is 75 µm long.

The light-current-voltage (LIV) characteristics of the follower laser for varying thermoelectric cooler (TEC) temperatures are shown in Fig. 4(a). The laser power was measured out of the front mirror using the SOA after the follower laser as a detector. The responsivity of the reverse biased SOA was assumed to be 1 A/W, which is typical for this type of device. The discontinuity in the light-current characteristic between 150 and 200 mA is due to an expected laser mode hop. The threshold current was measured to be 33 mA at a temperature of 15°C. Figure 4(b) shows overlapped spectra from the laser for various combinations of current applied to the front and back mirrors. The lasers demonstrate 40 nm of tuning from 1560 nm to 1600 nm. For all the spectra shown in Fig. 4(b), the laser gain section was biased at 150 mA and the phase section was biased at 10 mA. To achieve the tuning, the bias on the rear mirror was varied between 5 and 10 mA and the front mirror was biased up to approximately 30 mA. To tune the leader laser to 1572.335 nm, the bias on the rear mirror, phase section, gain section, and front mirror was 6 mA, 8.7 mA, 150 mA, and 23 mA, respectively.

Figure 4(c) shows the spectrum for the leader laser tuned to 1572.335 nm. At this wavelength of interest, the SMSR is 54 dB. The follower laser linewidth was characterized using a self-heterodyne method with a 25 km long fiber delay line. As shown in Fig. 4(d) the resulting beat note yields a 3-dB linewidth of 2.1 MHz. A resolution bandwidth of 3 MHz and a sweep time of 5 ms were used to capture this measurement.

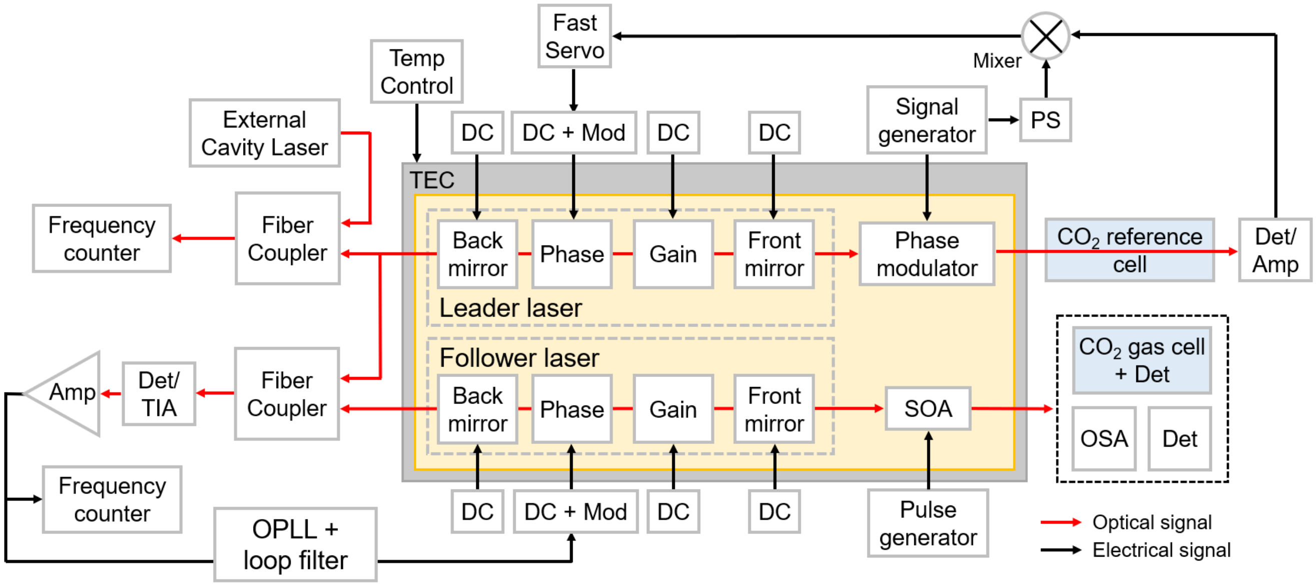

Fig. 5. Test setup for characterizing PIC subsystem. PS: electrical phase shifter; OSA: optical spectrum analyzer; TIA: transimpedance amplifier.

B. Phase Modulator

Figure 4(e) plots the modulation efficiency of the 2.5 mm long phase modulator in forward bias at a bias current of 25 mA. The efficiency was measured using a setup similar to that reported in [22], which transfers the optical modulation to the RF domain where it is demodulated with a homodyne IQ receiver. The drive levels in Fig. 4(e) assume 50 Ω loads. The phase modulator was operated in forward bias rather than reverse bias to take advantage of the higher efficiency and linearity, and to help minimize residual amplitude modulation (RAM) by avoiding electro-absorption due to the Franz-Keldysh effect. RAM is a significant source of noise in frequency modulation locking and future work will include analysis of the effect of RAM on the leader laser wavelength stabilization.

C. Photodiode

For the PIC characterized in this work and shown in Fig. 2, a fabrication defect resulting in optical loss in the coupler preceding the 60 µm long photodiode prevented the demonstration of on-chip beat note detection for the OPLL. Therefore, light was coupled off-chip to generate the beat note externally. It is worth noting, however, that similar photodiodes from other PICs and samples exhibited a 3-dB bandwidth of approximately 15 GHz, as shown in Fig. 4(f). This bandwidth would allow the follower laser to tune across the desired range of frequency steps to sample the CO_2 absorption line of interest.

V. SUBSYSTEM CHARACTERIZATION

The test setup used to characterize operation of the PIC subsystem is illustrated in Fig. 5. A precision TEC maintains the PIC temperature to prevent performance variations due to heating.

A. Leader Laser Stabilization

The leader laser is tuned to near 1572.335 nm by injecting current into the back and front mirrors and phase section. Feedback is applied to the phase section to maintain the wavelength at 1572.335 nm. The frequency-discriminating error signal used to stabilize the leader laser and the transmission of the CO_2 reference cell plotted in Fig. 6(a) were obtained by sweeping the frequency modulated leader laser across the CO_2 absorption line. To characterize the leader laser stability, a beat note is generated with a benchtop external cavity laser that serves as a frequency standard. The resulting beat frequency with and without feedback is measured and reported in Fig 6(b) for 60 minutes with 1 second gate times. Without feedback, the peak-to-peak frequency stability was 607 MHz and the frequency standard deviation was 90.5 MHz. With feedback, the peak-to-peak stability was 2.75 MHz and the standard deviation was 384 kHz, representing a 221- and 236-fold improvement, respectively.

B. Follower Laser Offset Locking

To lock the follower laser to the leader laser, the beat note between them was detected off chip as illustrated in Fig. 5. As with the leader laser, a DC bias applied to each of the laser mirrors and the phase section maintains the follower laser wavelength near 1572.335 nm. Feedback from the OPLL is applied to the phase section of the follower laser for stabilization at each programmed offset. Figure 6(c) shows the beat note between the leader and follower lasers with and without OPLL operation over 60 minutes for 1 second gate times at a programmed frequency offset of 2 GHz. Without the OPLL, the peak-to-peak frequency stability was 1.23 GHz and the frequency standard deviation was 162 MHz. With the OPLL, the peak-to-peak stability was 295 kHz and the standard deviation was 37.6 kHz. The mean frequency offset from the leader laser was measured to be 1.999911243 GHz.

Figure 6(d) shows overlapped spectra of the locked leader and follower lasers for follower laser frequency offsets of 1 to 15 GHz, demonstrating mode-hop-free tuning around 1572.335 nm. These results demonstrate the overall operation of the dual laser PIC for CO_2 absorption with use of an absolute wavelength reference.

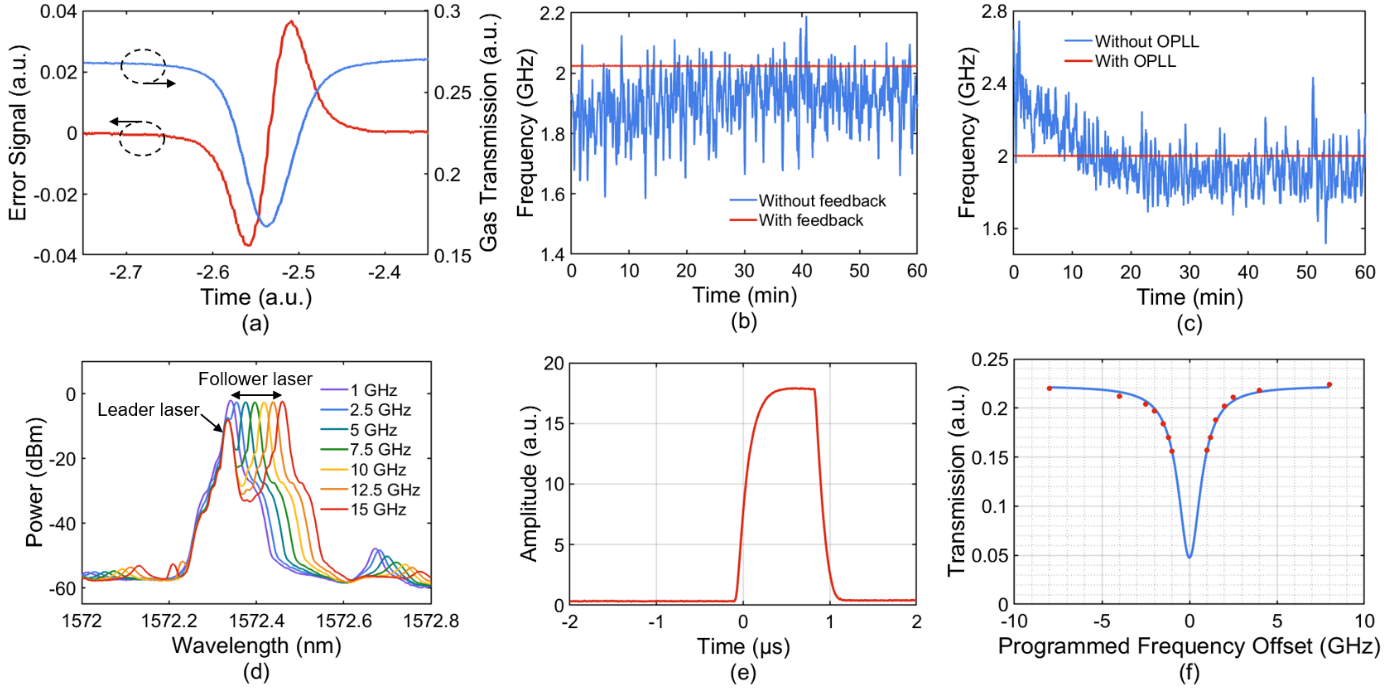

Fig. 6. (a) CO_2 reference cell absorption and the frequency-discriminating error signal used to lock the leader laser to the absorption line center. (b) Beat note between the leader laser and an external cavity laser with and without feedback to the leader laser phase section. (c) Beat note between the leader and follower laser with and without the OPLL engaged. (d) Overlaid spectra measured from the leader and follower laser as the follower laser is tuned from 1 – 15 GHz offset from the center wavelength. (e) 1 μs pulse generated by sweeping the bias on the SOA pulse carver from 0 to 100 mA. The pulse rise time is 262 ns and the fall time is 169 ns. (f) Measured absorption of a CO_2 test cell at several wavelengths overlaid with a Lorentzian fit. The FWHM of the fit is 1.6 GHz. Each point is an average of 1000 measurements taken over 100 μs.

C. Follower Laser Pulse Generation

Figure 6(e) shows a 1 μs pulse generated with the 1 mm long SOA after the follower laser. The SOA bias was ramped from 0 to 100 mA to achieve an ER of over 40 dB. The ER was estimated using a DC measurement because the power level in the off state was below the noise floor of the photodiode/TIA used to measure the pulse. Future work will include triggering the pulse generator after each follower laser wavelength step to create a train of pulses in frequency.

The peak pulse power coupled off chip was approximately 2 mW, which does not meet the desired 10 mW peak power. The main source of loss is the free space coupling between the output waveguide and lensed fiber. In future, this will be improved by attaching a fiber optic array to the PIC. The peak power could also be improved by increasing the current applied to the laser gain section and pulsed SOA. Newer design implementations will include PICs with a second amplifier SOA for power boosting in addition to the SOA for pulse generation.

D. Initial Gas Sampling and Sensing Measurement

Finally, sampling of the CO_2 absorption line with the follower laser was demonstrated. A second CO_2 gas cell set to a different pressure than the one used for the absolute wavelength reference was used as a sample for sensing. Figure 6(f) shows the results for points sampled at programmed offsets of ±1, 1.2, 1.5, 2, 2.5, 4, and 8 GHz with a Lorentzian fit overlaid. Each point is an average of 1000 measurements taken over 100 μs. The differences in transmission levels for points on either side of the absorption peak are most likely due to variations in PIC output power as the follower laser is tuned. This variation can be addressed by measuring the power level leaving the PIC at each frequency point. The limited bandwidth of the detector hardware built into the CO_2 cell prevented measurement during pulsed operation. Future work, which requires new hardware, will perform similar sampling but with generated pulses.

The sampled absorption spectrum shape captured here is quite reasonable for enabling accurate concentration measurement extraction from this data. This demonstration, whereby the leader laser was locked to the CO_2 reference, the follower laser was locked to the leader laser, and the follower laser was tuned to programmed frequency offsets to sample CO_2 in a separate cell, represents a significant advance toward realizing PIC based remote gas sensing for low CSWaP and eventual deployment on small airborne and space platforms.

VI. CONCLUSION

An InP PIC for a dual laser IPDA lidar architecture was demonstrated and used to perform an initial CO_2 gas sensing experiment. The PIC consists of leader and follower SGDBR lasers, directional couplers for splitting and coupling to various elements, a phase modulator for the leader laser stabilization to an absolute wavelength reference, a photodiode for beat note detection and follower laser locking, and an SOA for pulse generation. The PIC component and subsystem performance were evaluated against metrics developed for precision spectroscopy. Sampling of CO_2 gas at various frequency offsets was also demonstrated. This work represents a significant advance toward compact gas sensing lidar systems for airborne and space applications. Future work will include implementing the triggered frequency switching and pulsing of the follower laser output, the development of and integration with small form-factor printed-circuit board electronics, and the development of a compact wavelength reference to replace the bulky Herriott cell.

Acknowledgment

The authors acknowledge Parminder Ghuman, Amber Emory and Sergio Pinna for technical discussions. A portion of this work was performed in the UCSB Nanofabrication Facility.

References

[1] S. M. R. Crowell, S. R. Kawa, E. V. Browell, D. M. Hammerling, B. Moore, K. Schaefer, and S. C. Doney, "On the ability of space-based passive and active remote sensing observations of CO_2 to detect flux perturbations to the carbon cycle," *J. Geophys. Res. Atmos.*, 123, pp. 1460—1477, Jan. 2018.

[2] K. Numata, J. R. Chen, and S. T. Wu, "Precision and fast wavelength tuning of a dynamically phase-locked widely-tunable laser," *Opt. Express*, vol. 20, no. 13, pp. 14234—14243, Jun. 2012.

[3] K. Numata, J. R. Chen, S. T. Wu, J. B. Abshire, and M. A. Krainak, "Frequency stabilization of distributed-feedback laser diodes at 1572 nm for lidar measurements of atmospheric carbon dioxide," *Appl. Optics*, vol. 50, no. 7, pp. 1047—1056, Mar. 2011.

[4] J. R. Chen, K. Numata, and S. T. Wu, "Error analysis for lidar retrievals of atmospheric species from absorption spectra," *Opt. Express*, vol. 27, no. 25, pp. 36487—36504, Dec. 2019.

[5] J. R. Chen, K. Numata, and S. T. Wu, "Error reduction in retrievals of atmospheric species from symmetrically measured lidar sounding absorption spectra," *Opt. Express*, vol. 22, no. 21, pp. 26055—26075, Oct. 2014.

[6] G. R. Allan, J. B. Abshire, H. Riris, J. Mao, W. E. Hasselbrack, K. Numata, J. Chen, R. Kawa, M. Rodriguez, and M. Stephen, "Lidar measurements of CO2 column concentrations in the Arctic region of North America from the ASCENDS 2017 airborne campaign," *Proc. SPIE*, vol. 10779, Oct. 2018.

[7] J. B. Abshire, A. K. Ramanathan, H. Riris, G. R. Allan, X. Sun, W. E. Hasselbrack, J. Mao, S. Wu, J. Chen, K. Numata, S. R. Kawa, M. Y. M. Yang, and J. DiGangi, "Airborne measurements of CO2 column concentrations made with a pulsed IPDA lidar using a multiple-wavelength-locked laser and HgCdTe detector," *Atmos. Meas. Tech.*, vol. 11, pp. 2001—2025, Apr. 2018.

[8] J. Mao, A. Ramanathan, J. B. Abshire, S. R. Kawa, H. Riris, G. R. Allan, M. Rodriguez, W. E. Hasselbrack, X. Sun, K. Numata, J. Chen, Y. Choi, and M. Y. M. Yang, "Measurement of atmospheric CO_2 column concentrations to cloud tops with a pulsed multi-wavelength airborne lidar," *Atmos. Meas. Tech.*, vol. 11, pp. 127—140, Jan. 2018.

[9] H. Zhao, S. Pinna, F. Sang, B. Song, S. T. S. Brunelli, L. A. Coldren, and J. Klamkin, "High-power indium phosphide photonic integrated circuits," *IEEE J. Sel. Topics Quantum Electron.*, vol. 25, no. 6, Nov. 2019.

[10] H. Zhao, S. Pinna, B. Song, L. Megalini, S. T. S. Brunelli, L. A. Coldren, and J. Klamkin, "Indium phosphide photonic integrated circuits for free space optical links," *IEEE J. Sel. Topics Quantum Electron.*, vol. 24, no. 6, Nov. 2018.

[11] B. J. Isaac, B. Song, S. Pinna, L. A. Coldren, and J. Klamkin, "Indium phosphide photonic integrated circuit transceiver for FMCW LiDAR," *IEEE J. Sel. Topics Quantum Electron.*, vol. 25, no. 6, Nov. 2019.

[12] J. K. Doylend and S. Gupta, "An overview of silicon photonics for LIDAR," *Proc. SPIE*, vol. 11285, Feb. 2020.

[13] J. Fridlander, V. Rosborough, F. Sang, M. Nickerson, J. Chen, K. Numata, P. Verrinder, F. Gambini, S. Pinna, S. Kawa, M. Stephen, L. Coldren, and J. Klamkin, "Photonic integrated circuits for precision spectroscopy," *CLEO*, SF3O.3, 2020.

[14] M. Krainak, M. Stephen, E. Troupaki, S. Tedder, B. Reyna, J. Klamkin, H. Zhao, B. Song, J. Fridlander, M. Tran, J. E. Bowers, K. Bergman, M. Lipson, A. Rizzo, I. Datta, N. Abrams, S. Mookherjea, S. T. Ho, Q. Bei, Y. Huang, Y. Tu, B. Moslehi, J. Harris, A. Matsko, A. Savchenkov, G. Liu, R. Proietti, S. J. B. Yoo, L. Johansson, C. Dorrer, F. R. Arteaga-Sierra, J. Qiao, S. Gong, T. Gu, O. J. Ohanian, X. Ni, Y. Ding, Y. Duan, H. Dalir, R. T. Chen, V. J. Sorger, T. Komljenovic, "Integrated photonics for NASA applications," *Proc. SPIE*, vol. 10899, Mar. 2019.

[15] J. Klamkin, H. Zhao, B. Song, Y. Liu, B. Isaac, S. Pinna, F. Sang, L. Coldren, "Indium phosphide photonic integrated circuits: technology and applications," *2018 IEEE BCICTS*, 18305096, Oct. 2018.

[16] J. Fridlander, S. Pinna, V. Rosborough, S. Estrella, L. Johansson, and J. Klamkin, "RZ-DPSK photonic integrated transmitter for space optical communications," *Proc. SPIE*, vol. 10524, Feb. 2018.

[17] J. Fridlander, V. Rosborough, F. Sang, S. Pinna, S. Estrella, L. Johansson, and J. Klamkin, "High-speed RZ-DPSK photonic integrated transmitter for space optical communications," *Proc. SPIE*, vol. 11133, Sept. 2019.

[18] V. Rosborough, F. Gambini, J. Snyder, L. Johansson, and J. Klamkin, "Integrated transmitter for deep space optical communications," *IEEE AVFOP*, 16544752, oct. 2016.

[19] V. Rosborough, F. Gambini, J. Snyder, L. Johansson, and J. Klamkin, "Integrated indium phosphide pulse position modulation transmitter for free space communications," *OSA Advanced Photonics Congress*, ITu2A.3, July 2016.

[20] G. C. Bjorklund, "Frequency-modulation spectroscopy: a new method for measuring weak absorptions and dispersions," *Opt. Lett.*, vol. 5, no.1, pp. 15—17, Jan. 1980.

[21] T. G. B. Mason, "InP based photonic integrated circuits," *Dissertation*, June 1999.

[22] B. Arar, M. Schiemangk, H. Wenzel, O. Brox, A. Wicht, A. Peters, and G. Tränkle, "Method for in-depth characterization of electro-optic phase modulators," *Appl. Optics*, vol. 56, no. 4, pp. 1246—1252, Feb. 2017.

Joseph Fridlander received the B.S. and M. Eng degrees in electrical and computer engineering from Cornell University in 2012 and 2013 respectively. From 2013 to 2016 he was an RF Microwave engineer at the Jet Propulsion Laboratory where he developed ground system communications for NASA's Deep Space Network. He is currently pursuing his Ph.D. degree as a member of the Integrated Photonics Laboratory at UCSB where his research interests include photonic integrated circuits for free space optical communications and lidar remote sensing instruments.

Fengqiao Sang received the B.S. degree from Drexel University, Philadelphia, PA, USA, and the M.S. degree from University of California, Santa Barbara (UCSB). Currently, he is working toward the Ph.D. degree at UCSB. His research interests include semiconductor photonic integrated circuits and integrated Lidar.

Victoria Rosborough received the B.S. degree in physics from Mary Baldwin University, Staunton, VA, USA in 2012 and the M.S. degree in applied physics from the University of Oregon, Eugene, OR, USA in 2013. She is currently working toward the Ph.D. degree in the Integrated Photonics Lab, Department of Electrical and Computer Engineering, University of California Santa Barbara, Santa Barbara, CA, USA. Her research interests include semiconductor photonic integrated circuits for free space communications and sensing.

Fabrizio Gambini was born in Piacenza (Italy) in 1987. He received the B.S. degree and M.S. degree in telecommunication engineering from Politecnico of Milan, Milan, Italy in 2010 and 2012, respectively. In 2016 he received the Ph.D. degree from Scuola Superiore Sant'Anna, Pisa, Italy where his main activities were the study, design and characterization of photonic integrated devices based on silicon on insulator and indium phosphide technology platforms. In 2016 he was a visitor in the Integrated Photonics Laboratory at the University of California Santa Barbara (UCSB), Santa Barbara, CA, USA. He also worked with CNIT, Pisa, Italy, as a research assistant within the European Project IRIS, developing a high-capacity and reconfigurable wavelength-division multiplexing (WDM) photonic switch based on ring resonators. In 2018 he joined the Integrated Photonics Laboratory at UCSB as a Postdoctoral Research Associate working on the design, fabrication, and characterization of photonic integrated devices for data center interconnects, free space communications, and remote sensing for Earth science applications. In 2021 he joined the CRESST II program at NASA's Goddard Space Flight Center, as an Assistant Research Engineer through University of Maryland Baltimore County. He is developing photonic integrated circuits and mapping lidars for remote sensing and space applications.

Simone Tommaso Šuran-Brunelli was born in 1986 and is originally from Rovinj, Croatia and moved to Italy to receive the B.S. degree in industrial engineering with a thesis on semiconductor quantum dots and the M.S. degree in materials engineering with a thesis focused on atomic layer deposition, both at the Università degli Studi di Trieste, Italy. He was a process engineer for hot-rolled steel metallurgy at Danieli s.p.a. and a Research Fellow at Elettra Sincrotrone Trieste working on carbon nanotube synthesis and photoelectron spectroscopy before joining the University of California, Santa Barbara, Santa Barbara, CA, USA as a Ph.D. student. His current interests and duties revolve around metal organic chemical vapor deposition of III-V semiconductors for nanoelectronic and photonic applications

Jeffrey R. Chen received the Ph.D. degree in solid state physics in 1996 from the University of New York at Buffalo, Buffalo, New York, USA. He has been working for NASA Goddard Space Flight Center since 2005 on remote sensing lidars for measurement of atmospheric species as well as for altimetry. Before joining NASA, he worked for various US companies on the development of solid state and fiber lasers, as well as other active and passive optical components.

Kenji Numata received the Ph.D. degree in physics in 2003 from the University of Tokyo, Japan. He has been working for NASA Goddard Space Flight Center since then. He is playing key engineering roles in precision space laser systems, including the LISA (Laser Interferometer Space Antenna) mission and gas sensing lidars. Additionally, he has led a number of R&D projects involving advanced opto-electronic components and original concepts. His research interests include precision laser technology, laser metrology, control systems, solid-state and fiber lasers, remote sensing, nonlinear optics, and thermal noise.

Mark Stephen was born in the United States in 1970. He received the B.S. degree in physics from the University of Delaware in 1992 and the M.S. and Ph.D. degrees in applied physics from the University of Maryland Baltimore County in 2003 and 2008, respectively. He has worked at NASA's Goddard Space Flight Center since 1991 developing laser and electro-optics technologies for space-based applications. His research activities have included lasers, optical components and laser instruments. Dr. Stephen developed diode-pumped solid-state laser systems with an emphasis on laser diode array pumps and the space-qualification of these components, the use of fiber amplifier technology for gas detection and remote sensing using laser spectroscopy and new laser architectures including waveguides. He led the development of a fiber-based laser transmitter system to measure carbon dioxide in the Earth's atmosphere. Dr. Stephen worked on several satellite programs including: the Geoscience Laser Altimeter System (GLAS), the Mercury Laser Altimeter (MLA) and the Lunar Orbiter Laser Altimeter (LOLA). He was the product development lead for the Advanced Technology Laser Altimeter System (ATLAS) Laser, which is currently flying aboard ICESat-2. He is currently working on photonic integrated circuits and mapping lidars for space applications.

Larry A. Coldren (S'67–M'72–SM'77–F'82—LF'12) received the B.S. in electrical engineering and the B.A. in physics from Bucknell University, and joined Bell Laboratories in 1968. Under Bell Lab's support he then attended Stanford University and received the M.S. and Ph.D. degrees in electrical engineering in 1969 and 1972, respectively. Following 13 years in the research area with Bell Laboratories, he joined the ECE Department of the University of California at Santa Barbara (UCSB) in 1984. In 1986 he was a founding member of the Materials Department. He became the Fred Kavli Professor of Optoelectronics and Sensors in 1999. From 2009 to 2011, he was acting Dean of the College of Engineering, and in 2017 he became Prof. Emeritus and a Distinguished Research Prof.

In 1990, he co-founded Optical Concepts, later acquired as Gore Photonics, to develop novel VCSEL technology, and, in 1998, he co-founded Agility Communications, later acquired by JDSU (now Lumentum), to develop widely-tunable integrated transmitters. At UCSB, he has worked on multiple-section widely-tunable lasers and efficient vertical-cavity surface-emitting lasers (VCSELs). He continues to research high-performance InP-based photonic integrated circuits and high-speed, high-efficiency VCSELs for various applications.

Prof. Coldren has authored or coauthored over a thousand journal and conference papers, eight book chapters, a widely-used textbook, and 63 issued patents. He is a fellow of IEEE, OSA, IEE, and the National Academy of Inventors as well as a member of the National Academy of Engineering. He has been a recipient of the 2004 John Tyndall, the 2009 Aron Kressel, the 2014 David Sarnoff, the 2015 IPRM, and the 2017 Nick Holonyak, Jr. Awards.

Jonathan Klamkin Jonathan Klamkin (SM'15) received the B.S. degree from Cornell University, Ithaca, NY, USA, and the M.S. and Ph.D. degrees from the University of California Santa Barbara (UCSB), Santa Barbara, CA, USA. From 2008 to 2011, he was a member of the Technical Staff in the Electro-Optical Materials and Devices Group, MIT Lincoln Laboratory, Lexington, MA, USA. From 2011 to 2013, he was an Assistant Professor with the Institute of Communication, Information and Perception Technologies, Scuola Superiore Sant'Anna, Pisa, Italy. From 2013 to 2015, he was an Assistant Professor of Electrical and Computer Engineering (ECE) and Materials at Boston University, Boston, MA, USA. In 2015, he joined the ECE Department, University of California Santa Barbara, where he is currently a Professor and Director of the UCSB Nanotech. He has authored or coauthored 200 journal and conference papers. He or his group members were the recipient of best paper awards at the 2006 Conference on Optoelectronic and Microelectronic Materials and Devices, 2007 Microwave Photonics Conference, and 2017 and 2019 Asia Communications and Photonics Conference. He was the recipient of the NASA Early Career Faculty Award, the DARPA Young Faculty Award, and the DARPA Director's Fellowship.

A 50 Gbps 9.5 pJ/bit VCSEL-based Optical Link

Aaron Maharry[1*], Luis A. Valenzuela[1], Hector Andrade[1], Itshak Kalifa[2], Isabelle Cestier[2], Matan Galanty[2], Boaz Atias[2], Anna Sandomirsky[2], Elad Mentovich[2], Larry Coldren[1], James F. Buckwalter[1], and Clint L. Schow[1]

[1]Department of Electrical and Computer Engineering, University of California, Santa Barbara, 93106, USA

[2]*NVIDIA Networking, Hakidma 26, Ofer Industrial Park, Yokneam, Israel, Zip code 2069200*

[*]*amaharry@ucsb.edu*

***Abstract*—We present an 850 nm VCSEL-based NRZ optical link operating at 50 Gbps. The full link uses no external equalization and has a power efficiency of 9.5 pJ/bit.**

Keywords—VCSEL, optical link, transmitter, receiver

I. Introduction

There is increasing demand for high speed, low cost, and power efficient optical links to meet the demand created by data center network traffic growth. There have been demonstrations of non-return-to-zero (NRZ) VCSEL links operating at speeds up to 71 Gbps with bit error rate (BER) < 10^{-12} [1]. VCSEL links have also been demonstrated with low power consumption of 1 pJ/bit at 25 Gbps and 2.7 pJ/bit at 35 Gbps [2]. Operation at 56 Gbps below the 7% forward error correction (FEC) BER level was shown with an efficiency of 4.5 pJ/bit [3]. We report here a full 50 Gbps NRZ VCSEL link with BER of 1.7×10^{-4} and power efficiency of 9.5 pJ/bit.

II. Design

The transmitter (Tx) and receiver (Rx) assemblies for this link use the transimpedance amplifier (TIA) design described and characterized in earlier work [4]. The TIA was found to provide sufficient current to drive the VCSEL. Since the VCSEL driver has significantly more gain than is typical, an input signal of just 65 mVppd is sufficient to drive the link. While this additional gain in the Tx contributes to higher full-link power consumption, the reduced input swing reduces power consumption in the SERDES electronics. An array of NVIDIA VCSELs was copackaged with the driver chip on a custom PCB to form the Tx assembly, shown in Fig. 1(a). The NVIDIA VCSELs are 28 Gbaud NRZ or PAM4 compatible laser array consisting of four 850 nm GaAs/InGaAs QW VCSELs with 25 GHz BW, shown in Fig. 1(c). VCSEL anodes were wirebonded to the differential driver outputs, and cathodes were connected to independent supplies. The VCSEL used for data transmission was biased at 7.5 mA, and the unused VCSEL was turned off for power savings. The driver has a continuous time linear equalizer (CTLE) on the output stage to extend the link bandwidth. The total Tx power consumption was 268 mW. The Rx assembly consists of a 12 µm photodiode (Albis 40C1-TW2) copackaged with the Rx TIA on a separate custom PCB, shown in Fig. 1(b). The unused input of the differential TIA was left unconnected. The total Rx power consumption was 207 mW.

III. Experimental Results

For link characterization, a bit pattern generator (SHF 12105A) generates a PRBS31 pattern, which drives the Tx IC and VCSEL. Lensed multimode fiber is coupled to the VCSEL on the Tx assembly and the photodiode on the Rx assembly. The Rx TIA output is then either connected to a sampling oscilloscope (Tektronix DSA8300) with 70 GHz sampling module (Tektronix 80E11) for eye diagram measurements, or to a bit error rate tester (SHF 11104A) for BER measurements. An optical eye of a 50 Gbps waveform at the Tx output is shown in Fig. 2(a) and was measured with a reference receiver (Picometrix DG-32xr) with 28 GHz bandwidth, which is contributing to significant eye closure. Electrical eye diagrams at the Rx output for full-link operation up to 50 Gbps are shown in Fig. 2(b), (c), and (d). The measured full-link BER vs. average optical power (assuming infinite extinction ratio) at the receiver is shown in Fig. 2(e), and the corresponding BER bathtub curves measured at maximum optical modulation amplitude (OMA) are shown in Fig. 2(f). As there is no indication of a BER floor at these datarates, the achieved BER of 1.7×10-4 at 50 Gbps is limited by the achievable OMA, the full link BER can be expected to improve commensurately with increased Tx output OMA or coupling efficiency.

(a) (b) (c)

Fig. 1. The assembled transmitter (a) and receiver (b). The NVIDIA VCSEL array (c).

The information, data, or work presented herein was funded in part by the Advanced Research Projects Agency-Energy (ARPA-E), U.S. Department of Energy, under Award Number DE-AR0000848. The views and opinions of authors expressed herein do not necessarily state or reflect those of the United States Government or any agency thereof.

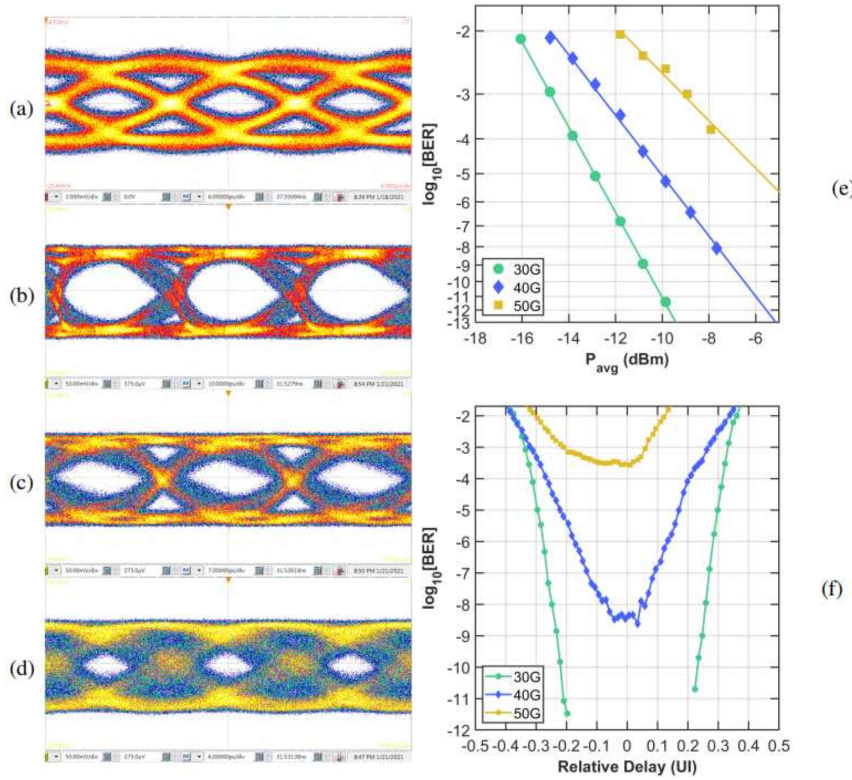

Fig. 2. The optical eye diagram at the Tx output at 50 Gbps (a) with a scale of 3 mV/div. Electrical eye diagrams at the Rx output showing full-link operation at 30 (b), 40 (c), and 50 (d) Gbps, with scales of 50 mV/div. Full-link BER vs. average optical power received (assuming infinite extinction ratio) at various datarates (e). Measured full-link BER bathtub curves at various datarates (f).

Table 1. State-of-the-art comparison.

Reference	[1]	[2]		[3]	This Work
Technology	130 nm SiGe	32 nm SOI CMOS		130 nm SiGe	130 nm SiGe
DR (Gbps)	71	25	35	56	50
Energy Efficiency (pJ/bit)	25.5	1.0	2.7	4.5	9.5
Equalization	2-Tap FFE	No Eq.		No Eq.	CTLE
BER	10^{-12}	10^{-12}		5×10^{-4}	1.7×10^{-4}
Driver Input Swing (Vppd)	800	200		650	65

IV. Conclusion

We have demonstrated a full VCSEL link operating at 50 Gbps with a BER of 1.7×10^{-4} and power efficiency of 9.5 pJ/bit. A comparison of this result with state-of-the-art VCSEL-based full link demonstrations is shown in Table 1. Notably, this link operates with only 65 mVppd driver input swing, a significant improvement over the state-of-the-art.

Acknowledgment

The authors acknowledge Nikos Argyris, Dimitrios Kalavrouziotis, Paraskevas Bakopoulos, and Anders Larsson for their contribution on VCSEL link simulations. The authors thank Ned Cahoon and Mike Peters at GlobalFoundries for access to the SiGe 8XP process.

References

[1] D. M. Kuchta et al., “A 71-Gb/s NRZ Modulated 850-nm VCSEL-Based Optical Link,” IEEE Photonics Technology Letters, vol. 27, no. 6, pp. 577–580, Mar. 2015.

[2] J. E. Proesel et al., “35-Gb/s VCSEL-Based Optical Link using 32-nm SOI CMOS Circuits,” in Optical Fiber Communication Conference/National Fiber Optic Engineers Conference 2013 (2013), paper OM2H.2, Mar. 2013, p. OM2H.2.

[3] N. Ledentsov Jr. et al., "Energy efficient 850-nm VCSEL based optical transmitter and receiver link capable of 56 Gbit/s NRZ operation," Proc. SPIE 10938, Vertical-Cavity Surface-Emitting Lasers XXIII, 109380J (1 March 2019).

[4] L. A. Valenzuela et al., "A 108-Gbps, 162-mW Cherry-Hooper Transimpedance Amplifier," in 2020 IEEE BiCMOS and Compound semiconductor Integrated Circuits and Technology Symposium (BCICTS), Monterey, CA, USA, 2020, pp. 1-4.

Gallium Arsenide Photonic Integrated Circuit Platform for Tunable Laser Applications

Paul A. Verrinder, Lei Wang, Joseph Fridlander, Fengqiao Sang, Victoria Rosborough, Michael Nickerson, Guangning Yang, Mark Stephen, Larry Coldren, *Life Fellow, IEEE,* Jonathan Klamkin, *Senior Member, IEEE*

***Abstract*—An active-passive integration technique for operation near a wavelength of 1030 nm has been developed on a gallium arsenide (GaAs) photonic integrated circuit platform. The technique leverages quantum wells (QWs) that are slightly offset vertically from the center of the waveguide, and selectively removed prior to upper cladding regrowth to form active and passive regions. The active region consists of indium gallium arsenide (InGaAs) QWs, gallium arsenide phosphide (GaAsP) barriers, GaAs separate confinement heterostructure layers, and aluminum gallium arsenide (AlGaAs) cladding. Fabry Perot lasers with various widths were fabricated and characterized, exhibiting high injection efficiency of 98.8%, internal active loss of 3.44 cm^{-1}, and internal passive loss of 4.05 cm^{-1} for 3 µm wide waveguides. The 3 µm, 4 µm, and 5 µm wide lasers demonstrated greater than 50 mW output power at 100 mA continuous wave (CW) current and threshold current as low as 9 mA. 20 µm wide broad area lasers demonstrated 240 mW output power, 35.2 mA threshold current under CW operation, and low threshold current density of 94 A/cm^2 for 2 mm long lasers. Additionally, these devices exhibit transparency current density of 85 A/cm^2 and good thermal characteristics with T_0 = 205K, and T_η = 577K.**

***Index Terms*—InGaAs quantum well, LiDAR, photonic integrated circuits (PIC), quantum well lasers, semiconductor lasers, tunable laser**

I. Introduction

Since their invention, semiconductor laser diodes have become ubiquitous as compact, highly efficient, coherent light sources for a wide variety of applications, particularly within the telecommunications industry. In continual pursuit of reduced cost, size, weight, and power (CSWaP), additional optical components such as modulators, optical amplifiers, and photodetectors have been monolithically integrated with laser light sources to generate photonic integrated circuits (PICs) [1], [2]. The primary application of PIC technology to date has been for optical data communications, where indium phosphide (InP) based platforms have achieved the highest level of integration in order to leverage the low-loss optical fiber spectral regions around 1310 nm and 1550 nm [1]-[3]. Building on the maturation of PIC technology, PICs have also been pursued for other applications including free space laser communications, microwave photonics, 3D mapping light detection and ranging (Lidar), and remote gas sensing Lidar [4]-[6]. Additionally, there are applications outside of the traditional optical communications wavelength regions that could benefit from the CSWaP reduction offered by PIC technology. The focus of this work is on development of a PIC platform operating with a wavelength near 1030 nm for use in Lidar, specifically for airborne and space applications where deployment on small platforms is highly desirable. Wavelengths such as 1030 nm or 1064 nm are common choices for topographical Lidar systems owing to low atmospheric absorption and the existence of high-quality detectors, such as silicon or indium gallium arsenide (InGaAs) avalanche photodiodes (APDs), for this spectral range [7], [8]. CSWaP is of critical importance for any airborne or space-based system, and PIC technology at this wavelength would allow for multiple optical components to be integrated onto a single compact platform, while still leveraging the advantages of this wavelength for Lidar and sensing.

Gallium arsenide (GaAs) lasers based on strained layer InGaAs/GaAs quantum wells (QWs) have been used to build efficient laser diodes with high power output near 1 µm for many years [9] and are an obvious choice for this application. However, to date most laser development in this wavelength regime has focused on high power Fabry Perot [10], [11], distributed Bragg reflector (DBR), and distributed feedback (DFB) laser diodes [12], [13]. These were constructed primarily with large optical cavities and thick waveguide layers making them unsuitable for the active-passive integration necessary for PICs. Little work has been pursued for integrating 1 µm lasers with other active and passive optical components on a compact PIC platform analogous to InP PICs, or to develop widely tunable lasers near 1030 nm. In this paper, we demonstrate an active-passive integration technique on GaAs, for operation near 1030 nm, to enable PICs with widely tunable lasers. We also present designs and development for widely tunable lasers with sampled grating DBR (SGDBR) mirrors for extended tuning range, and integrated semiconductor optical amplifiers (SOA). This work provides a path for future PIC development

The authors acknowledge funding support from the NASA ESTO Advance Component Technology program. A portion of this work was carried out in the UCSB Nanofabrication Facility. (*Corresponding author: Paul A. Verrinder.)*
P. A. Verrinder, L. Wang, J. Fridlander, F. Sang, V. Rosborough, M. Nickerson, L. A. Coldren, and J. Klamkin are with the Department of Electrical and Computer Engineering, University of California, Santa Barbara, CA 93106 USA (email: pverrinder@ucsb.edu; leiwang@ucsb.edu; jfridlander@ucsb.edu; fsang@ece.ucsb.edu; rosborough@ucsb.edu; nickersonm@ece.ucsb.edu; coldren@ece.ucsb.edu; klamkin@ece.ucsb.edu).
G. Yang, and M. Stephen are with NASA Goddard Space Flight Center, Greenbelt, MD 20771 USA (email: guangning.yang-1@nasa.gov; mark.a.stephen@nasa.gov)

on GaAs and demonstrates that passive optical components can be integrated with active devices without sacrificing the well-known benefits of strained InGaAs/GaAs QW lasers [9].

II. Material Design and Device Fabrication

The PIC platform presented leverages an etch and regrowth process whereby the active QWs are etched selectively to form active and passive regions, and the upper cladding and p-contact are formed in a subsequent regrowth step. Table I presents the details of the epitaxial layers, with the layers formed during the regrowth step indicated, as well as the layers that were selectively removed to create passive regions. Lattice mismatched $In_xGa_{1-x}As$ QWs are the most common choice for wavelengths between 0.88 µm and 1.1 µm [9], however the high indium (In) content required to reach longer wavelengths introduces significant strain. To maintain an acceptable cumulative strain in the active region of this multi-QW (MQW) design, 5 nm $In_xGa_{1-x}As$ QWs were used with x = 0.271, and 8 nm gallium arsenide phosphide ($Ga_{1-x}AsP_x$) barriers were included with x = 0.1 (instead of GaAs barriers) to provide strain compensation. This 3 QW active region is surrounded by GaAs separate confinement heterostructure (SCH) layers, and aluminum gallium arsenide (AlGaAs) is used for both the upper and lower cladding layers. Prior to fabrication and regrowth, the photoluminescence (PL) spectrum of the wafer was measured, and the results are presented in Fig. 1 where the peak PL emission wavelength is 1038 nm. The peak near 870 nm is emission from the GaAs substrate.

TABLE I
Epitaxial layers for Active-Passive Integration

	Material	Thickness (nm)	Doping (cm^-3)
Regrowth Layers	GaAs	200	(p) 5e19
	$Al_{0.4}GaAs$	800	(p) 7e17
	$Al_{0.4}GaAs$	200	(p) 5e17
	$Al_{0.4}GaAs$	300	(p) 2e17→5e17
	$Al_{0.2}GaAs$	50	(p) 2e17
Selectively removed for passive sections	GaAs	20	(p) 1e17
	GaAs	20	UID
	$GaAsP_{0.1}$	8	UID
	$In_{0.271}GaAs$	5	UID
	$GaAsP_{0.1}$	8	UID
	$In_{0.271}GaAs$	5	UID
	$GaAsP_{0.1}$	8	UID
	$In_{0.271}GaAs$	5	UID
	$GaAsP_{0.1}$	8	UID
Base Structure	GaAs	90	UID
	$Al_{0.2}GaAs$	100	(n) 1e17
	$Al_{0.75}GaAs$	1600	(n) 1e18
	GaAs	500	(n) 1e18
	GaAs	625+/-20 µm	(n) 2-5e18

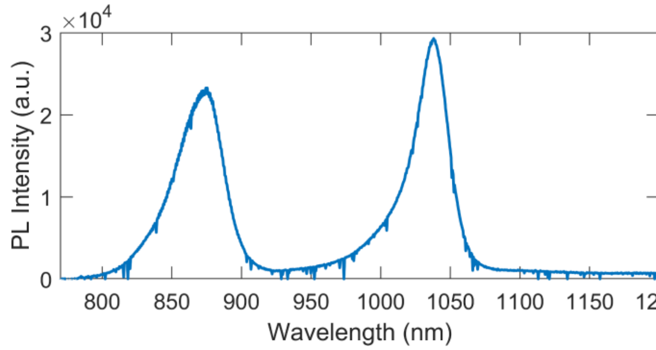

Fig. 1. PL spectrum of epitaxial material prior to fabrication and regrowth.

Fig. 2 shows schematic diagrams illustrating the primary fabrication process steps, along with simulated mode profiles for the active and passive regions for a 3 µm wide rib waveguide. The active QW material was selectively removed, to form passive regions, using inductively coupled plasma reactive ion etching (ICP-RIE) with chlorine (Cl_2) and nitrogen (N_2) gas chemistry. Following regrowth of the upper cladding layer and p-contact layer by metalorganic chemical vapor deposition (MOCVD), the rib waveguides were etched also using a Cl_2/N_2 ICP-RIE process. The etch depth for this step is 1.35 µm, stopping in the upper p-cladding to form a rib waveguide structure as illustrated in Fig. 2(d). The device was passivated by depositing 100 nm of silicon nitride (SiN) followed by 300 nm of silicon dioxide (SiO_2). This was followed by via formation by etching the dielectric layers to expose the GaAs p-contact layer. Ti/Pt/Au (10/40/1000 nm) was used to form the topside p-contacts, and Ti/Pt/Au (20/40/500 nm) was used for the backside n-contact. The GaAs substrate was thinned to approximately 150 µm before depositing the n-contact metal, and then laser bars were cleaved to form facets and to facilitate characterization. Both all-active and active-passive lasers were fabricated and characterized.

The active-passive platform was designed to enable efficient coupling of light between the active and passive sections, and in turn to minimize reflection at the interface. Based on optical mode profile simulations for the 3 µm wide rib waveguide, 96% of the optical power from the active region is coupled directly to the fundamental mode of the passive region waveguide. For the fundamental TE mode, the effective index difference between the active and passive waveguides is only 0.0548, and the active-passive interface is angled at 67° with respect to the waveguide propagation direction so that any reflections back into the active region waveguide are minimized. To maximize optical coupling between active and passive regions in the offset QW design, the QWs should be placed near the top of the active layer stack to minimize the height of the “step” illustrated in Fig. 2(b). However, this comes with a tradeoff, as the fractional overlap of the optical mode with the thin QW layers, i.e., the confinement factor Γ_{QW}, should be maximized to allow for sufficient gain in the active region. The design presented in Table I vertically places the QWs in the upper half of the active region, with thinner GaAs and AlGaAs SCH layers above, allowing for efficient active-passive coupling while still achieving an overall confinement factor Γ_{QW} of 5.02% for all three QWs. Considering the large material gain characteristic of the InGaAs QWs, this is sufficient for realizing highly efficient laser operation.

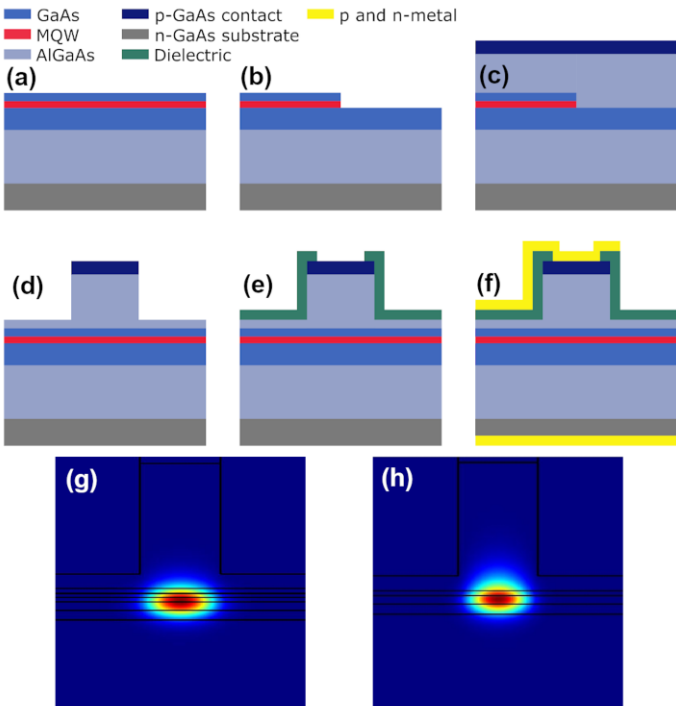

Fig. 2. Summary of primary fabrication steps including (a) initial epitaxial layers, (b) active-passive etch, (c) upper cladding and p-contact layer regrowth, (d) ridge waveguide etch, (e) surface passivation and p-contact via formation, (f) p-metal and n-metal contact formation. Modal simulations for (g) active region and (h) passive region. (a)-(c) are side view illustrations of the active and passive regions. (d)-(f) are cross sections of the active region.

Laser devices were fabricated with varying waveguide widths. These included 2 µm, 2.5 µm, 3 µm, 4 µm, and 5 µm wide all-active Fabry Perot (FP) lasers, and active-passive FP lasers, as well as broad area laser diodes with widths of 10 µm, 20 µm, 50 µm, and 100 µm. Fig. 3 shows a scanning electron microscope (SEM) image of the etched active-passive transition prior to regrowth, a SEM tilted cross-section image of a 3 µm wide fabricated laser facet, and a microscope image of completely fabricated active-passive laser and all-active laser. Figure 3(b) shows both the base epitaxial layers and the upper cladding layer, with no apparent defects or discontinuities at the regrowth interface.

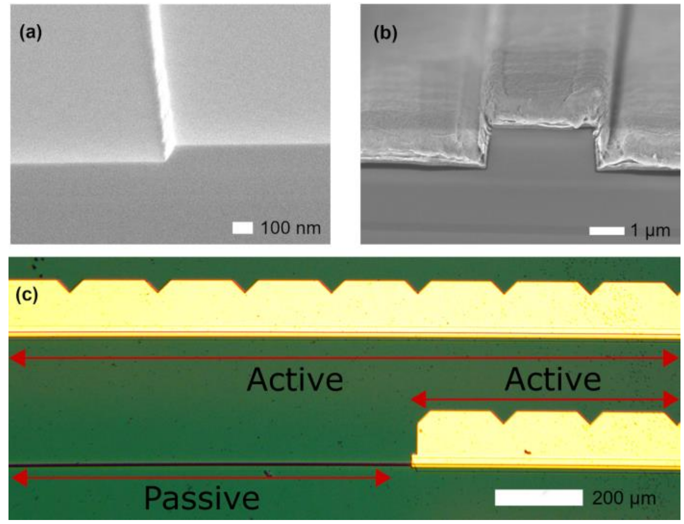

Fig. 3. SEM image of (a) etched active-passive transition prior to regrowth, (b) active side cleaved facet of 3 µm wide fabricated laser, and (c) top view microscope image of completed devices on the processed wafer.

III. Device Testing and Characterization

To characterize the gain material and the passive waveguides, multiple cleaved-facet FP lasers of various widths and lengths were tested. These devices include all-active lasers and active-passive lasers. Light-current-voltage (LIV) characteristics were measured for the devices under both continuous wave (CW) and pulsed current operation using 500 ns pulse widths at 0.5% duty cycle. Fig. 4(a) shows a typical LIV characteristic measured from one side of a 20 µm wide cleaved facet broad area laser with 800 µm long cavity under CW applied current. This device exhibits 120 mW output power from a single side (240 mW total) with a peak wall-plug efficiency of 16%, differential efficiency of 57.8% (from both sides), and threshold current of 35.2 mA. Additional measurements on a 20 µm wide laser with a 2 mm long cavity exhibited threshold current density as low as 94 A/cm^2. Similarly, Fig. 4(b) shows single-sided LI curves for five different 600 µm long FP lasers with widths from 2 µm to 5 µm. These lasers all exhibit threshold current below 12.6 mA with the lowest threshold being 9 mA for the 2.5 µm wide laser. Additionally, the 3 µm, 4 µm, and 5 µm wide devices output greater than 25 mW of optical power from each facet at 100 mA CW current. The differential efficiencies from both facets are approximately 55% for all three of these laser geometries.

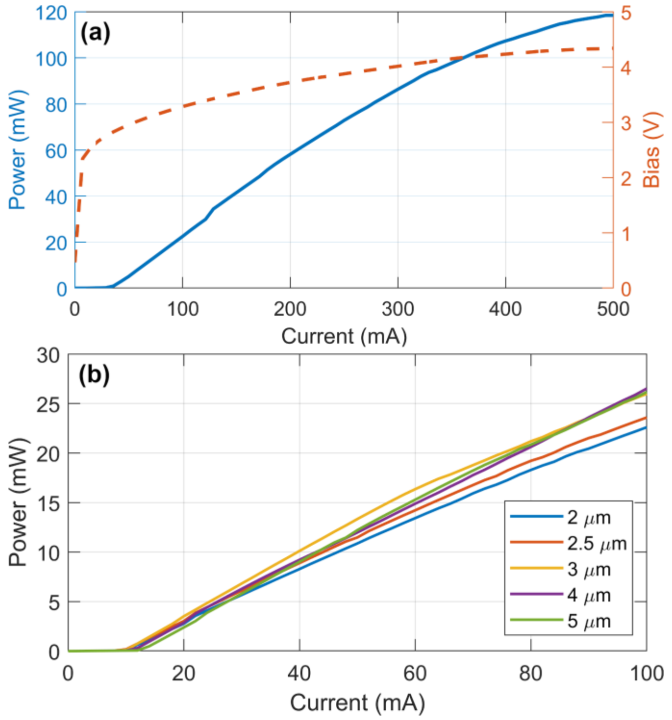

Fig. 4. Light-current characteristics for (a) 20 µm wide by 800 µm long broad area laser and (b) 600 µm long lasers between 2 µm and 5 µm wide under CW current injection.

A. Measurement and Extraction of Laser and Material Properties

The internal quantum efficiency, η_i, and internal loss, $\langle\alpha_i\rangle$, were extracted by measuring the differential efficiency, η_d, for multiple device lengths for FP lasers that are otherwise identical. The following relationship was used to extract material parameters:

$$\frac{1}{\eta_d} = \frac{\langle\alpha_i\rangle}{\eta_i \ln\left(\frac{1}{R}\right)} L + \frac{1}{\eta_i}, \tag{1}$$

where R is the total reflection coefficient accounting for both mirrors and L is the length of the laser cavity.

For the 20 µm wide broad area lasers, measurements were performed under pulsed current operation, with 500 ns pulses at 0.5% duty cycle, to mitigate self-heating effects and obtain accurate material parameters. Light-current (LI) characteristics were obtained for devices with lengths of 2800 µm, 2400 µm, 2000 µm, 1600 µm, 1200 µm, 1000 µm, 400 µm, and 200 µm, and the differential efficiency was extracted for each LI curve and plotted as a function of cavity length in Fig. 5. A linear curve fit to (1) was used to extract an η_i of 98.8% and $\langle\alpha_i\rangle$ of 3.44 cm^{-1}. These devices exhibit state of the art performance in terms of efficiency and loss when compared to results from similar devices with strained InGaAs QWs on GaAs [14]-[17].

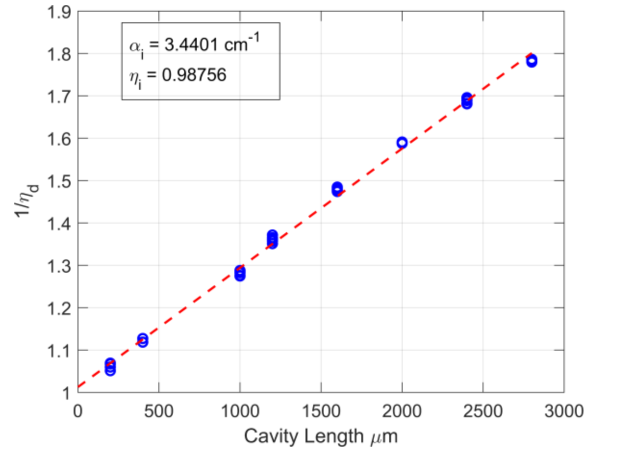

Fig. 5. Inverse differential efficiency as a function of cavity length for 20 µm wide broad area lasers under pulsed current operation with linear fit to extract loss and efficiency.

For comparison to the LI characteristics in Fig. 4(b) for all-active lasers, Fig. 6(a) shows LI characteristics for active-passive FP lasers with various waveguide widths, all with a 400 µm long gain section coupled to a 400 µm long passive section as shown in the schematic of Fig. 6(b), and the device image of Fig. 3(c). The laser optical power was measured from both sides of the devices as reported in Fig. 6(a). The slightly lower power from the active side is to be expected as the active layers create a more reflective cleaved facet mirror due to the slightly higher effective index in this section. The kinks in output power at high current injection are due to mode hopping, as these waveguides are not single transverse mode. Compared to the data for the all-active lasers shown in Fig. 4, the active-passive devices demonstrate comparable performance in terms of power output, differential efficiency, and threshold current. All five of the active-passive lasers measured exhibit threshold currents below 10.7 mA and as low as 7 mA for the 2 µm wide laser. The total output power from both sides was measured to be greater than 50 mW for all devices and as high as 62 mW for the 5 µm wide laser at 100 mA CW current.

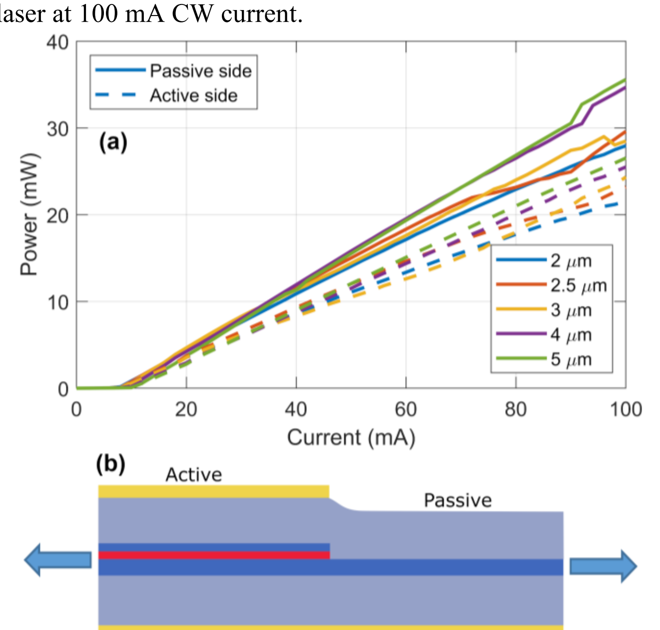

Fig. 6. (a) LI characteristics for active-passive lasers with 400 μm long active section and 400 μm long passive section. (b) Side-view schematic diagram of a generic active-passive laser cavity.

Similar to the procedure for extracting $\langle\alpha_i\rangle$, the loss in the passive section can be extracted by obtaining LI measurements for multiple active-passive devices with a constant active section length but varying passive section lengths. For a laser cavity with both active and passive sections, the total differential efficiency from both sides is given by [18]:

$$\eta_d = \eta_i \eta_{da} \eta_{dp}, \quad (2)$$

where,

$$\eta_{da} = \frac{ln\sqrt{\frac{1}{R_1 R_2}}}{\langle\alpha_i\rangle_{xy}^{a} L_a + ln\sqrt{\frac{1}{R_1 R_2}}}, \quad (3)$$

and

$$\eta_{dp} = \frac{\frac{1-R_1}{\sqrt{R_1}} + \frac{1-R_3}{\sqrt{R_3}}}{\frac{1-R_1}{\sqrt{R_1}} + \frac{1-R_3 e^{-2\alpha_{ip} L_p}}{\sqrt{R_3} e^{-\alpha_{ip} L_p}}}, \quad (4)$$

R_1 is the reflection coefficient at the active-air interface, R_2 is the reflection coefficient at the active-passive interface, R_3 is the reflection coefficient at the passive-air interface, L_a is the gain section length, L_p is the passive section length, $\langle\alpha_{ia}\rangle$ is the internal loss in the active region (3.44 cm^{-1} as extracted from all-active lasers), and α_{ip} is the internal loss in the passive region. For the purpose of calculations, R_1, R_2, and R_3 were obtained from simulations as, 0.290, 6.86e-5, and 0.284, respectively.

LI measurements were performed under pulsed current operation for 3 μm wide active-passive FP lasers with a 400 μm long active section length and a passive section that was cleaved back in increments from 2800 μm to 600 μm. Power output was measured from both sides at each length to obtain the total differential efficiency, η_d, for each laser, and these data points were plotted as a function of passive section length as shown in Fig. 7. Combining equations (3) and (4) with equation (2) and using the internal loss and injection efficiency from the all-active laser measurements, α_{ip} is the only unknown quantity and therefore can be extracted. To obtain an accurate value for α_{ip}, a fit to equation (2) was applied to the experimental data points as in Fig. 7. The extracted internal passive loss was 4.05 cm^{-1}.

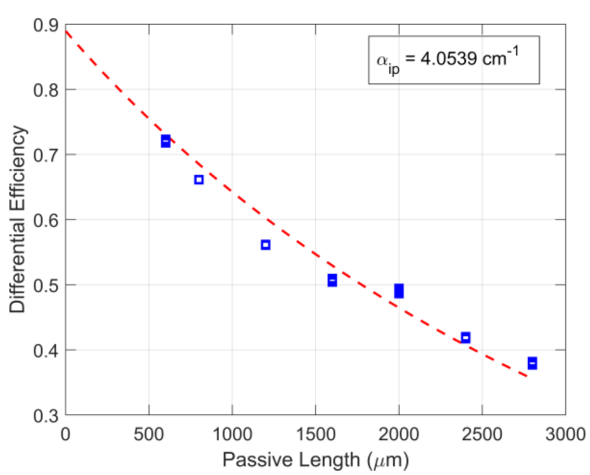

Fig. 7. Differential efficiency as a function of passive section length for 3 μm wide active-passive FP lasers with 400 μm long gain sections.

It may initially seem counterintuitive that the passive waveguide loss is higher than the active internal loss. Although the epitaxial layer structure was originally designed for higher (75%) aluminum (Al) content for the $Al_xGa_{1-x}As$ p-cladding layer, 40% Al was instead used because of the immaturity of the high Al content growth. The lower Al content leads to higher refractive index (3.236 at 1030 nm for $Al_xGa_{1-x}As$ with $x = 0.4$), and therefore lower index contrast between the core and cladding. The lower index contrast reduces the optical mode confinement leading to more overlap with the p-doped cladding, leading to additional loss from free-carrier absorption [19]. The Al content for the upper cladding can be increased for future devices and PICs to overcome this issue. Optical mode simulations for a design with 60% Al in the p-cladding show significant improvement in mode confinement, decreasing the amount of overlap with the p-cladding significantly. A calculation of theoretical free-carrier absorption loss [19] indicates that increasing the Al to 60% to improve confinement will decrease the overall passive loss to 3.6 cm^{-1}. Further adjustments, such as increasing the thickness of the GaAs waveguide layer and optimizing the p-doping profile could reduce the passive internal loss further.

The threshold current was also measured for each of the device lengths reported in Fig. 5, and these values were used to calculate each threshold current density. Using the internal loss extracted, the threshold modal gain, Γg_{th}, was also calculated for each length and plotted as a function of current density in Fig. 8. The threshold modal gain is given by:

$$\Gamma g_{th} = \alpha_{ia} + \frac{1}{L} ln\left(\frac{1}{R}\right), \quad (5)$$

where L is the cavity length, and R is the total reflection coefficient. Gain versus current density data can be fitted to an exponential two-parameter curve,

$$J = J_{tr} e^{\frac{g}{g_0}}, \quad (6)$$

where J_{tr} is the transparency current density, and g_0 is a fitting parameter. The experimental data points shown in Fig. 8 were fitted to this characteristic curve to extract a transparency current density of 85.54 A/cm^2 and g_0 of 1055 cm^{-1}. These values compare favorably to similar state-of-the-art lasers reported in the literature.

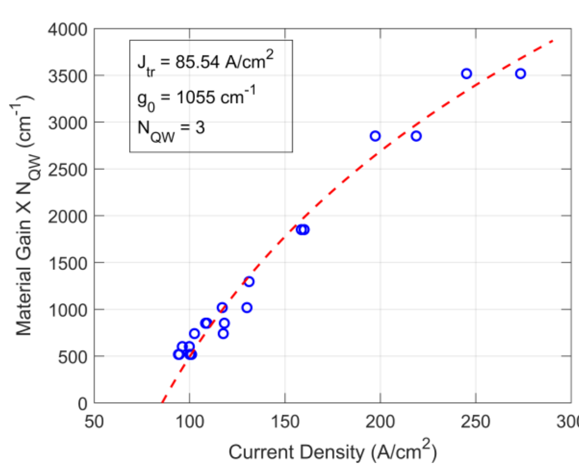

Fig. 8. Material gain as a function of current density for three 5 nm $In_xGa_{1-x}As$ ($x = 0.271$) QWs with 8 nm $Ga_{1-x}AsP_x$ ($x = 0.1$) barriers, obtained from 20 µm wide lasers measured under pulsed current operation.

B. Laser Spectral Measurements and Thermal Performance

The light output from a 3 µm wide active-passive laser with 400 µm long active and passive sections (800 µm total length) was coupled to a lensed optical fiber and connected to an optical spectrum analyzer (OSA) to measure the laser output spectrum at different current injection levels. These spectra are shown in Fig. 9. The spectrum is slightly red-shifted compared to the PL emission from Fig. 1, showing a lasing peak near 1045 nm near lasing threshold (8 mA current), compared to the PL emission wavelength of 1038 nm. This is expected because thermal activation during PL measurements can cause an increase in bandgap, shifting the emission spectrum slightly to shorter wavelengths. Conversely, under CW current injection, self-heating causes the laser output to shift to longer wavelength as observed in Fig. 9. It should also be noted that this waveguide is not a single mode waveguide, as evidenced by the two distinct peaks in the lasing spectrum particularly at higher current injection levels. This multi-mode behavior was expected based on simulation and is not a concern since future applications planned for this platform will include grating mirrors that provide some mode filtering.

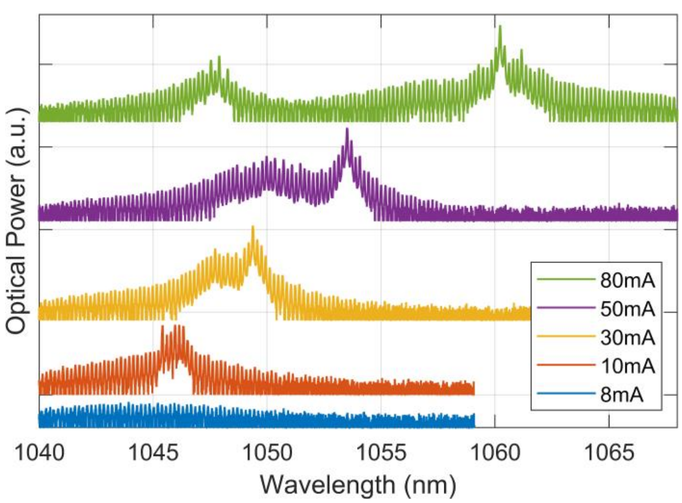

Fig. 9. Lasing spectra for 3 µm wide active-passive laser with 400 µm long gain section and 400 µm long passive section under various levels of CW current injection.

The effect of heating on the lasing wavelength is observed more directly in Fig. 10 where the same device was characterized under constant CW current injection at 40 mA while the temperature was varied from 10°C to 70°C. The peak lasing wavelength shifts predictably to longer wavelengths at a rate of 0.32 nm/°C as the temperature is increased.

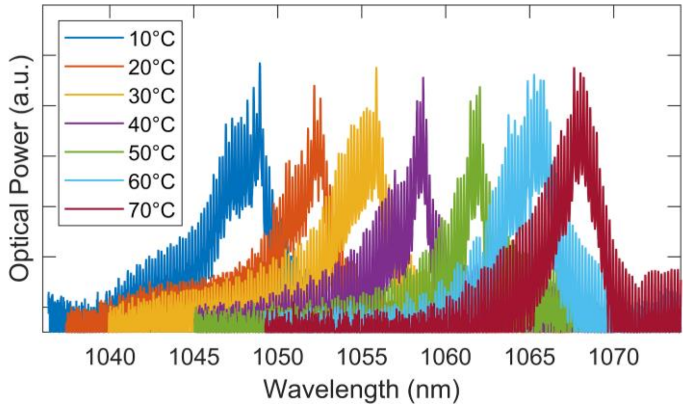

Fig. 10. Lasing spectra for various temperatures for 3 µm devices at 40 mA CW current.

Additional measurements were taken to determine thermal characteristics of these devices. Both the threshold current and differential efficiency exhibit an exponential dependence on temperature, with an increase in temperature leading to higher threshold and lower differential efficiency. The relative change in threshold current can be expressed by [18],

$$\frac{I_{th1}}{I_{th2}} = exp\left(\frac{T_1 - T_2}{T_0}\right), \tag{6}$$

where T_1 and T_2 are the initial and final temperatures, I_{th1} and I_{th2} are initial and final threshold currents, and T_0 is the overall characteristic temperature. LIV measurements were obtained at different temperatures to observe the change in threshold current with heating and to obtain a value for characteristic temperature, resulting in T_0 = 205 K, which is consistent with commonly reported values for InGaAs QW lasers on GaAs [14]. Fig. 11 reports the experimentally determined threshold current as a function of temperature for the data points used with (6) to obtain T_0. Similarly, heating also has a deleterious effect on laser efficiency, with greater current required to obtain the same output power at higher temperature. There is a characteristic temperature for differential efficiency, T_η, which can be obtained by calculating the ratio of differential efficiencies at different temperatures,

$$\frac{\eta_{d1}}{\eta_{d2}} = exp\left(-\frac{T_1 - T_2}{T_\eta}\right). \tag{7}$$

where η_{d1} and η_{d2} are the initial and final differential efficiencies, and T_η is the characteristic temperature. From the same measurements used to calculate T_0, differential efficiency as a function of temperature was also obtained and plotted in Fig. 11, and (7) was used to extract a T_η = 577 K from the experimental data points. This data was obtained from a 20 µm wide, 400 µm long laser that was tested under pulsed current operation while the temperature was varied with a thermoelectric cooler (TEC).

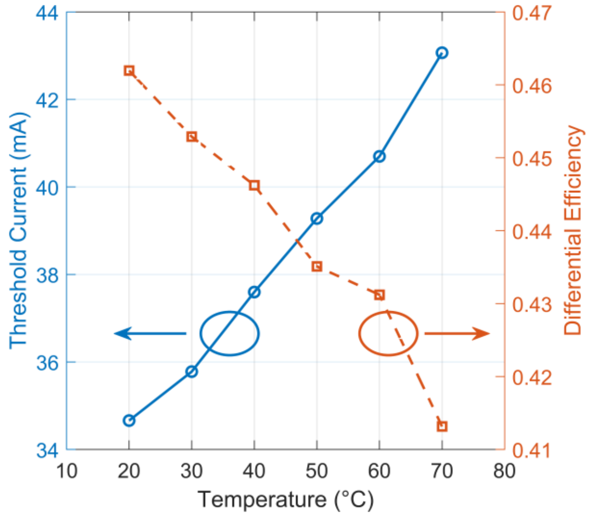

Fig. 11. Threshold current and single-sided differential efficiency as a function of temperature for a 20 µm wide, 400 µm long broad area laser. Measurements were performed with pulsed current to mitigate self-heating, while the stage temperature was varied from 20°C to 70°C.

Both the all-active FP lasers from Fig. 4 and the active-passive FP lasers from Fig. 6 exhibit state-of-the-art performance in terms of threshold current, efficiency, loss, gain characteristics, and temperature dependence when compared to similar devices reported in literature [14]-[17]. This demonstrates that the offset QW design, active-passive etch, and subsequent upper cladding regrowth process presented here offers a suitable platform for active-passive photonic integration without sacrificing the well-known performance advantages of the InGaAs/GaAs material system for optical gain. This platform is viable for advanced monolithic PICs that incorporate lasers with other active and passive components.

IV. Tunable Laser Design and Development

The platform presented can be used for constructing PICs with integrated single frequency and tunable lasers such as DBR or DFB lasers. To extend the tunable range for topographical Lidar applications, we are pursuing sampled grating DBR (SGDBR) laser designs [20]. Fig. 12 shows a side-view schematic of a generic SGDBR laser that includes a gain section, phase section, and front and back SGDBR mirrors. These devices can optionally include a semiconductor optical amplifier (SOA) that follows the front mirror for amplification. Such a PIC tunable laser can be realized with our nominal 1030 nm active-passive integration technique.

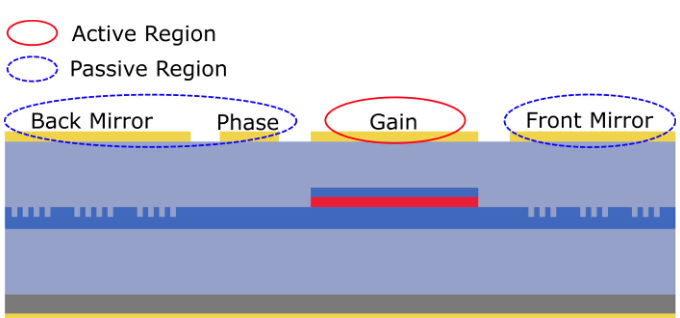

Fig. 12. Schematic diagram of four section SGDBR laser.

The viability of this platform for active-passive integration has already been demonstrated with the FP laser results presented. With some modifications to the regrowth layers for performance improvement, the only additional step required for a tunable SGDBR laser such as that illustrated in Fig. 12 is the formation of the grating mirrors. Initial development has been carried out, and Fig. 13 shows a simulation of front and back mirror reflectivity spectra for a tunable SGDBR laser design. The grating etch depth is 35 nm resulting in a coupling coefficient for the unsampled gratings of $\kappa = 486\ \mathrm{cm}^{-1}$, obtained from simulations. This mirror design is expected to tune over a range of at least 23 nm, and possibly as much as 30 nm depending on the effective index change that can be achieved via current injection.

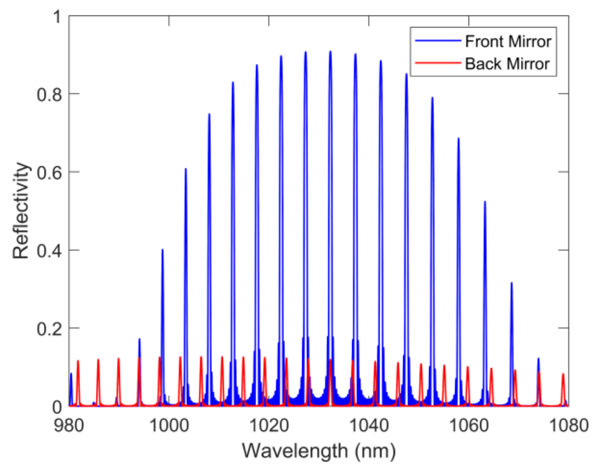

Fig. 13. SGDBR front and back mirror reflectivity spectra.

Gratings were patterned with electron beam lithography (EBL). The grating pitch is 157 nm with a 50% duty cycle for a Bragg wavelength at 1032.5 nm. The gratings were etched using ICP-RIE and the same regrowth procedure developed for the active-passive lasers was utilized to overgrow the gratings and form the p-cladding in both the active and passive sections. Fig. 14(a) shows the free running output spectrum from a laser with these gratings, and Fig. 14(b) shows an SEM image of the gratings prior to regrowth. This result is preliminary, and further fabrication and characterization is being carried out in pursuit of widely tunable lasers, however this demonstrates that the active-passive integration process presented here is feasible for lasers with grating mirrors. To the best of the authors knowledge, this would be the first realization of in-plane extended tuning range lasers on GaAs centered around 1030 nm and would provide a viable path toward widely tunable laser PICs for Lidar and other applications requiring low system CSWaP.

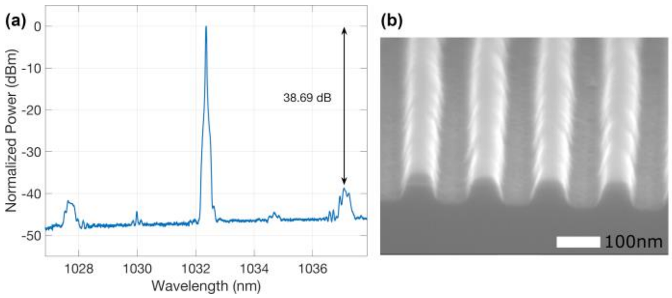

Fig. 14. (a) Output spectrum of free running SGDBR laser and (b) SEM image of etched gratings.

V. CONCLUSIONS

An active-passive PIC platform on GaAs was demonstrated for operation near 1030 nm. This platform integrates active sections with gain, with passive sections, while maintaining state-of-the-art FP laser performance for this material system. The design and fabrication development for widely tunable lasers that will leverage this platform were also reported. Such a tunable laser PIC platform is valuable for airborne Lidar applications that require low system CSWaP for deployment on small platforms. Future work will include modification of the upper cladding regrowth design to decrease the passive section loss; by increasing the Al content in the p-cladding to 60%, which will decrease the refractive index of this layer, the optical mode will be more confined in the waveguide core layers thus decreasing free-carrier absorption loss due to the modal overlap with the p-doped cladding. By etching the tunable laser gratings following the active-passive etch, the same regrowth process can be leveraged to simultaneously overgrow the gratings and form the upper cladding for the active and passive sections. This fairly elegant active-passive platform can therefore realize highly complex PICs for applications with an operating wavelength near 1030 nm.

REFERENCES

[1] F. Kish *et al.,* “From visible light-emitting diodes to large-scale iii-v photonic integrated circuits,” *Proceedings of the IEEE*, vol. 101, no. 10, pp 2255–2270, Oct. 2013

[2] J. Klamkin *et al*., "Indium Phosphide Photonic Integrated Circuits: Technology and Applications," 2018 IEEE BiCMOS and Compound Semiconductor Integrated Circuits and Technology Symposium (BCICTS), San Diego, CA, USA, 2018, pp. 8-13, doi: 10.1109/BCICTS.2018.8550947.

[3] F. A. Kish *et al.*, “Current status of large-scale InP photonic integrated circuits,” *IEEE J. Sel. Top. Quantum Electron.*, vol. 17, no. 6, pp. 1470–1489, 2011, doi: 10.1109/JSTQE.2011.2114873.

[4] B. J. Isaac, B. Song, S. Pinna, L. A. Coldren, and J. Klamkin, “Indium Phosphide Photonic Integrated Circuit Transceiver for FMCW LiDAR,” *IEEE J. Sel. Top. Quantum Electron.*, vol. 25, no. 6, pp. 1–7, 2019, doi: 10.1109/JSTQE.2019.2911420.

[5] J. Fridlander *et al.*, “Photonic integrated circuits for precision spectroscopy,” Conference on Lasers and Electro-Optics (CLEO) 2020.

[6] H. Zhao *et al.*, “Indium Phosphide Photonic Integrated Circuits for Free Space Optical Links,” *IEEE J. Sel. Top. Quantum Electron.*, vol. 24, no. 6, pp. 1–6, 2018, doi: 10.1109/JSTQE.2018.2866677.

[7] M. A. Krainak, X. Sun, G. Yang, and W. Lu, “Comparison of linear-mode avalanche photodiode lidar receivers for use at one-micron wavelength” *in Proc. SPIE Defense, Security, and Sensing,* Orlando, FL, USA, 2010

[8] A. W. Yu *et al.*, “A 16-beam non-scanning swath mapping laser altimeter instrument” in *Proc. SPIE LASE,* San Francisco, CA, USA, 2013

[9] J. J. Coleman, “Strained-Layer InGaAs Quantum-Well,” *IEEE Journal on Seected Topics in Quantum Electronics,* vol. 6, no. 6, pp. 1008–1013, 2000.

[10] A. Pietrzak, M. Zorn, R. Huelsewede, J. Meusel, and J. Sebastian, “Development of highly-efficient laser diodes emitting around 1060nm for medical and industrial applications,” in *Proc. SPIE LASE*, San Francisco, CA, USA, 2019

[11] W. Gao *et al.*, “High-power 1060-nm InGaAs/GaAs single-mode laser diodes,” in *Proc. SPIE LASE,* San Jose, CA, USA, 2005

[12] S. Spieberger, M. Schiemangk, A. Wicht, H. Wenzel, G. Erbert, and G. Tränkle, “DBR laser diodes emitting near 1064 nm with a narrow intrinsic linewidth of 2 kHz,” *Appl. Phys. B Lasers Opt.*, vol. 104, no. 4, pp. 813–818, 2011, doi: 10.1007/s00340-011-4644-7.

[13] H. Wenzel, J. Fricke, A. Klehr, A. Knauer, and G. Erbert, “High-power 980-nm DFB RW lasers with a narrow vertical far field,” *IEEE Photonics Technol. Lett.*, vol. 18, no. 6, pp. 737–739, 2006, doi: 10.1109/LPT.2006.871127.

[14] Z. Qiao *et al.*, “High-performance 1.06-μm InGaAs/GaAs double-quantum-well semiconductor lasers with asymmetric heterostructure layers,” *Semicond. Sci. Technol.*, vol. 34, no. 5, 2019, doi: 10.1088/1361-6641/ab110b.

[15] X. Li, L. H. Duan, Y. Zhou, A. P. Liu, and Z. R. Wei, “Strained InGaAs/GaAs quantum-well laser emitting at 1054 nm,” *J. Supercond. Nov. Magn.*, vol. 23, no. 6, pp. 937–939, 2010, doi: 10.1007/s10948-010-0741-9.

[16] S. Y. Hu, D. B. Young, S. W. Corzine, A.C. Gossard, L. A. Coldren, “High-efficiency and low-threshold InGaAs/AlGaAs quantum-well lasers”, *Journal of Applied Physics,* vol. 76, no. 6, pp. 3932-3934, 1994

[17] N. Tansu, L. J. Mawst, “High-Performance Strain-Compensated InGaAs-GaAsP-GaAs (λ = 1.17 μm) Quantum-Well Diode Lasers,” *IEEE Photonics Technology Letters,* vol. 13, no. 3, pp. 179–181, 2001.

[18] L. A. Coldren, *Diode Lasers and Photonic Integrated Circuits,* 2nd ed. Hoboken, NJ, USA: Wiley, 2012.

[19] K. A. Bulashevich, V. F. Mymrin, S. Y. Karpov, D. M. Demidov, and A. L. Ter-Martirosyan, “Effect of free-carrier absorption on performance of 808 nm AlGaAs-based high-power laser diodes,” *Semicond. Sci. Technol.*, vol. 22, no. 5, pp. 502–510, 2007, doi: 10.1088/0268-1242/22/5/008.

[20] V. Jayaraman, Z. M. Chuang, and L. A. Coldren, “Theory, Design, and Performance of Extended Tuning Range Semiconductor Lasers with Sampled Gratings,” *IEEE J. Quantum Electron.*, vol. 29, no. 6, pp. 1824–1834, 1993, doi: 10.1109/3.234440.

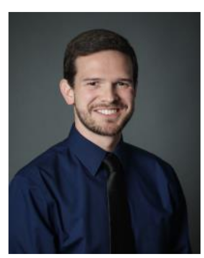

Paul A. Verrinder received the B.S. degree in electrical engineering from California State University Fresno in 2015, and the M.S. degree in electrical and computer engineering from University of California, Santa Barbara (UCSB) in 2020. From 2015 to 2018 he was an electrical engineer for NAVAIR at China Lake. He is currently pursuing a Ph.D. in the Electrical and Computer Engineering department at UCSB. His interests are in integrated photonics for optical communications and LIDAR.

Lei Wang received the B.S. degree in physics from Shandong University, China in 2014, and the M.S. degree in electrical and computer engineering from University of California, Santa Barbara (UCSB) in 2019. From 2014 to 2017, he was a project research assistant affiliated by Shandong University and the Institute of Semiconductors, Chinese Academy of Sciences. He is currently a Ph.D. graduate in the Electrical and Computer Engineering department at UCSB. His research interests include quantum dot lasers, and silicon photonics.

Joseph Fridlander received the B.S. and M.Eng degrees in electrical and computer engineering from Cornell University in 2012 and 2013 respectively. From 2013 to 2016 he was an RF Microwave engineer at the Jet Propulsion Laboratory where he developed ground system communications for NASA's Deep Space Network. He is currently pursuing his Ph.D. degree as a member of the Integrated Photonics Laboratory at UCSB where his research interests include photonic integrated circuits for free space optical communications and lidar remote sensing instruments.

Fengqiao Sang received the B.S. degree from Drexel University, Philadelphia, PA, USA, and the M.S. degree from University of California, Santa Barbara (UCSB). Currently, he is working toward the Ph.D. degree at UCSB. His research interests include semiconductor photonic integrated circuits and integrated Lidar.

Victoria Rosborough received the B.S. degree in physics from Mary Baldwin University, Staunton, VA, USA in 2012 and the M.S. degree in Applied Physics from the University of Oregon, Eugene, OR, USA in 2013. She is currently working toward the Ph.D. degree in the Integrated Photonics Lab, Department of Electrical and Computer Engineering, University of California Santa Barbara, Santa Barbara, CA, USA. Her research interests include semiconductor photonic integrated circuits for free space communications and sensing.

Michael Nickerson is currently a Ph.D. student in the Electrical and Computer Engineering Department at UCSB. He received his bachelor's degree in Physics from the University of Washington, after which he spent several years at JILA in Boulder, Colorado and at MIT Lincoln Laboratory in Lexington, Massachusetts. His interests are in integrated photonics for free-space optical communications and optical phased arrays**.**

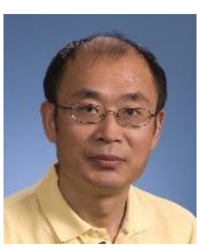

Guangning Yang received his BS in physics from Sichuan University, Chengdu, China and PhD in Electrical Engineering from Drexel University. He worked at Tyco Submarine Systems as lead design engineer for the first 10GBPS transmitter for trans-oceanic optical communication. In 2000, he worked as the Technical Section Lead for high speed optical communication terminal for Dorsal/Corvis Networks. He has worked at NASA Goddard Space Flight Center (GSFC) since 2008 on lidar and laser ranging and communication. He was the Product Development Lead on photon counting detector for the ATLAS Laser Altimeter instrument on ICESAT-2 Mission. He is currently working on next generation space lidar altimeter and optimetrics experiment on Laser Communications Relay Demonstration (LCRD).

Mark Stephen was born in the United States in 1970. He received the B.S. degree in Physics from the University of Delaware in 1992 and the M.S. and Ph.D. degrees in applied physics from the University of Maryland Baltimore County in 2003 and 2008, respectively.

He has worked at NASA's Goddard Space Flight Center since 1991 developing laser and electro-optics technologies for space-based applications. His research activities have included lasers, optical components and laser instruments. Dr. Stephen developed diode-pumped solid-state laser systems with an emphasis on laser diode array pumps and the space-qualification of these components, the use of fiber amplifier technology for gas detection and remote sensing using laser spectroscopy and new laser architectures including waveguides. He lead the development of a fiber-based laser transmitter system to measure carbon dioxide in the Earth's atmosphere. Dr. Stephen worked on several satellite programs including: the Geoscience Laser Altimeter System (GLAS), the Mercury Laser Altimeter (MLA) and the Lunar Orbiter Laser Altimeter (LOLA). He was the product development lead for the Advanced Technology Laser Altimeter System (ATLAS) Laser, which is currently flying aboard ICESat-2. He is currently working on photonic integrated circuits and mapping lidars for space applications.

Larry A. Coldren (S'67–M'72–SM'77–F'82—LF'12) received the BS in Electrical Engineering and BA in Physics from Bucknell University, and joined Bell Laboratories in 1968. Under Bell Lab's support he then attended Stanford University and received the MS and PhD degrees in Electrical Engineering in 1969 and 1972, respectively. Following 13 years in the research area with Bell Laboratories, he joined the ECE Department of the University of California at Santa Barbara (UCSB) in 1984. In 1986 he was a founding member of the Materials Department. He became the Fred Kavli Professor of Optoelectronics and Sensors in 1999. From 2009 to 2011, he was acting Dean of the College of Engineering, and in 2017 he became Prof. Emeritus and a Distinguished Research Prof.

In 1990, he co-founded Optical Concepts, later acquired as Gore Photonics, to develop novel VCSEL technology, and, in 1998, he co-founded Agility Communications, later acquired by JDSU (now Lumentum), to develop widely-tunable integrated transmitters and transponders. At UCSB, he has worked on multiple-section widely-tunable lasers and efficient vertical-cavity surface-emitting lasers (VCSELs). He continues to research high-performance InP-based photonic integrated circuits and high-speed, high-efficiency VCSELs for various applications.

Prof. Coldren has authored or coauthored over a thousand journal and conference papers, eight book chapters, a widely-used textbook, and 63 issued patents. He is a fellow of IEEE, OSA, IEE, and the National Academy of Inventors as well as a member of the National Academy of Engineering. He has been a recipient of the 2004 John Tyndall, the 2009 Aron Kressel, the 2014 David Sarnoff, the 2015 IPRM, and the 2017 Nick Holonyak, Jr. Awards.

Jonathan Klamkin (SM'15) received the B.S. degree from Cornell University, Ithaca, NY, USA, and the M.S. and Ph.D. degrees from the University of California Santa Barbara (UCSB), Santa Barbara, CA, USA. From 2008 to 2011, he was a member of the Technical Staff in the Electro-Optical Materials and Devices Group, MIT Lincoln Laboratory, Lexington, MA, USA. From 2011 to 2013, he was an Assistant Professor with the Institute of Communication, Information and Perception Technologies, Scuola Superiore Sant'Anna, Pisa, Italy. From 2013 to 2015, he was an Assistant Professor of Electrical and Computer Engineering (ECE) and Materials at Boston University, Boston, MA, USA. In 2015, he joined the ECE Department, University of California Santa Barbara, where he is currently a Professor and Director of the UCSB Nanotech. He has authored or coauthored 200 journal and conference papers. He or his group members were the recipient of best paper awards at the 2006 Conference on Optoelec-tronic and Microelectronic Materials and Devices, 2007 Microwave Photonics Conference, and 2017 and 2019 Asia Communications and Photonics Conference. He was the recipient of the NASA Early Career Faculty Award, the DARPA Young Faculty Award, and the DARPA Director's Fellowship.

JVST A
Journal of Vacuum Science & Technology A

Review of key vertical-cavity laser and modulator advances enabled by advanced MBE technology

Cite as: J. Vac. Sci. Technol. A **39**, 010801 (2021); https://doi.org/10.1116/6.0000574
Submitted: 23 August 2020 . Accepted: 04 November 2020 . Published Online: 30 November 2020

Larry A. Coldren

JVST A
Journal of Vacuum Science & Technology A

REVIEW

avs.scitation.org/journal/jva

Review of key vertical-cavity laser and modulator advances enabled by advanced MBE technology

Cite as: J. Vac. Sci. Technol. A **39**, 010801 (2021); doi: 10.1116/6.0000574
Submitted: 23 August 2020 · Accepted: 4 November 2020 ·
Published Online: 30 November 2020

View Online Export Citation CrossMark

Larry A. Coldren[a)]

AFFILIATIONS

Electrical and Computer Engineering and Materials Departments, University of California, Santa Barbara, California 93106

Note: This paper is part of the Special Topic Collection: Honoring Dr. Art Gossard's 85th Birthday and his Leadership in the Science and Technology of Molecular Beam Epitaxy.

[a)]**Electronic mail:** coldren@ucsb.edu

ABSTRACT

In this special issue honoring Professor Arthur Gossard, I am delighted to be able to review a small segment of the work he has enabled while at UCSB on the subject of the title, but further limited to devices grown all-epitaxially. When he arrived in 1987 from Bell Labs, he had already been consulting on the installation of our new Gen-II MBE that we intended to use for vertical-cavity Fabry–Pérot modulators, devices somewhat similar to those he had grown at Bell Labs. However, within a couple of years, we obtained leading results on reflection modulators, moving the on/off contrast from prior values of less than 5:1 to more than 50:1 with insertion losses of less than 2 dB, required voltages in the 2–4 V range, and changes in reflection per volt to ~20%/V. These had multiple-quantum-well (MQW) active regions to phase shift and partially absorb the resonant lightwaves within a cavity formed between two distributed-Bragg-reflector (DBR) mirrors all formed in the AlGaAs/GaAs system. Also in this same period, novel vertical-cavity surface-emitting laser (VCSEL) structures analogous to the modulators were developed. They had strained InGaAs/GaAs MQW actives and AlGaAs/GaAs DBRs and operated near 980 nm. The initial new idea was to place active quantum wells only at the maxima of the cavity E-field standing wave, which provides nearly a doubling of the modal gain they contribute. These designs quickly led to leading results in threshold current ($<1\ \mathrm{kA/cm^2}$—1990 and $I_{th} < 1$ mA with $P_o > 1$ mW—1991), power out (up to 113 mW cw—1993), and temperature stability with gain offset (constant output over 50 °C—1993). Additional notable results in the 1990s included a selective oxidation of AlGaAs to form lens-like intra-cavity apertures for dramatic reductions in optical cavity loss; the first strained layer InGaAlAs/GaAs 850 nm VCSELs; and an 8-wavelength division multiplexing VCSEL array integrated within a 60 μm diameter for direct emission into a multimode fiber. In the 2000s, results included all-epitaxially grown 1310 nm and 1550 nm VCSELs that employed AlGaAsSb DBRs and AlGaInAs actives with tunnel junctions to enable two n-type contacts on InP for low thermal and electrical resistance; multi-terminal VCSELs for polarization modulation to double the information output on a single optical beam; and a novel high-speed, high-efficiency design that incorporated sophisticated bandgap engineering in the DBRs and carbon doping for low optical loss and electrical resistance, midlevel Al-content mirror layers near the cavity for deep oxidation to reduce capacitance, and a redesigned lens-like aperture for reduced mode volume. This latter design gave record modulation bandwidth and efficiency results then, and it is still being used around the world for the leading results today. In the most recent decade, InGaAsSb/AlGaAsSb/GaSb materials for VCSELs and photonic ICs have been studied for emission in the 2–4 μm wavelength range.

I. INTRODUCTION

Professor Arthur Gossard has had, and continues to have, an extraordinary impact on semiconductor materials and device physics and technology, primarily through his work with molecular beam epitaxy (MBE). In this paper, I will review some highlights of the leading work he has enabled at UCSB on vertical-cavity optical modulators and lasers in which I have been involved. This represents a relatively small component of his overall contributions over the past three-plus decades but, in my opinion, a component that has had a major impact on society. Some of his other contributions are mentioned in other articles in this issue.

Our first Varian Gen-II (system-A) had arrived shortly before Art in 1987 and was being used for AlGaAs and InGaAs/GaAs; the second one (system-B), which was interconnected to the first along with a processing chamber via a transfer tube a couple of years later, had an Sb source for AlGaAsSb and eventually phosphorus capability for InP.

Our initial projects involved vertical-cavity reflection modulators,[1–7] so my students, now also guided by Art, worked on MBE system-A to grow multilayer stacks consisting of a bottom AlAs/$Al_{0.2}Ga_{0.8}As$ multilayer DBR mirror, a GaAs/$Al_{0.2}Ga_{0.8}As$ MQW active, and finally a top AlAs/$Al_{0.2}Ga_{0.8}As$ multilayer DBR mirror. The number and thickness of layers in each were varied for various designs. As will be detailed below, record-high on/off contrasts, with record-low drive voltages and insertion losses were developed within a few years. As codiscoverer of the quantum-confined Stark-effect (QCSE),[8] a primary effect used in these devices, Art gave much more guidance than just on the MBE growth during this time.

In 1988, partially due to our modulator work, we came to the realization that a significant improvement could be made to the design of vertical-cavity surface-emitting-lasers (VCSELs) if the quantum-well gain layers were only placed at the cavity optical E-field standing wave maxima, and any losses were placed at the nulls.[9–11] In fact, this improvement changed the world of VCSEL design—for some number of quantum wells, the gain given to the optical mode would now be *doubled*, compared to a uniform placement of the wells along the standing wave. In practice, this meant

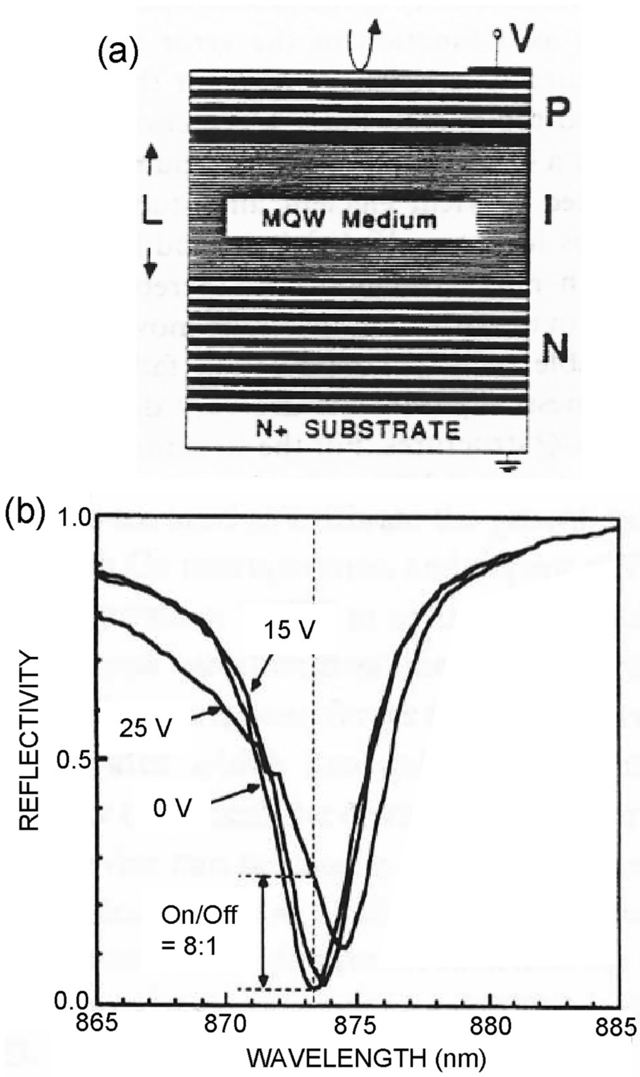

FIG. 1. (a) Schematic of MQW index modulator. Here, the top DBR mirror has five AlAs-$Al_{0.2}Ga_{0.8}As$ periods, active MQW has 103—10 nm GaAs QWs with 10 nm $Al_{0.2}Ga_{0.8}As$ barriers and the bottom DBR has 8.5 AlAs-$Al_{0.2}Ga_{0.8}As$ periods. (b) Reflection spectra for reverse bias voltages of 0, 15, and 25 V. Adapted with permission from Simes *et al.*, Appl. Phys. Lett. **53**, 637 (1988). Copyright 1988, AIP Publishing LLC.

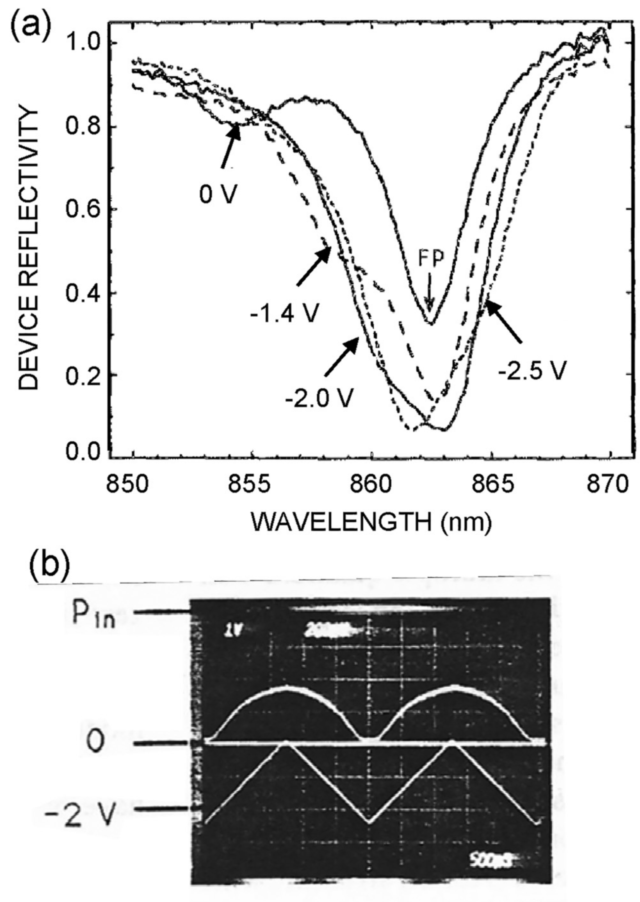

FIG. 2. (a) Reflection spectra with four reverse bias voltages from 0 to 2.5 V. (b) Sweeps of reflected power (top) and reverse bias (bottom) vs time; (500 μs/div.) Device schematic as in Fig. 1(a). Top and bottom mirror stacks had 5 and 20.5 periods of AlAs/$Al_{0.2}Ga_{0.8}As$, respectively; active MQW had 24 periods of 10 nm GaAs QWs with 10 nm $Al_{0.2}Ga_{0.8}As$ barriers. Adapted with permission from Yan *et al.*, Appl. Phys. Lett. **56**, 1626 (1990). Copyright 1990, AIP Publishing LLC.

that the number of wells could be cut in half to reach threshold gain, the threshold current could be halved, the threshold power dissipation cut to a quarter, and most importantly, devices that could not work at all due to heating would now work well. Other researchers picked up on this invention, and the race was on to demonstrate the first practical VCSELs using it. Although we convincingly demonstrated the concept with optical pumping of VCSELs grown with active regions having either uniform gain or properly placed segmented gain regions of the same net length,[12] we lost the race to demonstrate low threshold electrically pumped lasers by a couple of months to a joint Bell Labs—Bellcore effort.[13]

However, our devices were more advanced because we had added probe pads and antireflecting (AR)-coatings, which provided more power out.[14] So, with our advanced MBE and processing capability together with a team of outstanding graduate students, we were able to generate many of the leading results in low-threshold, high-output power, and temperature-stable VCSELs over the next couple of years.[15–19] Additional innovations which followed included: strained-layer InGaAlAs/GaAs 850 nm VCSELs;[20] a lens-like intracavity aperture for a dramatic reduction in optical cavity loss;[21,22] an 8-wavelength wavelength division multiplexing (WDM) VCSEL array;[23] all-epitaxially grown 1310 nm and 1550 nm VCSELs that employed AlGaAsSb DBRs and AlGaInAs actives on InP;[24,25] multiterminal VCSELs for polarization modulation;[26,27] and a novel high-speed, high-efficiency design that incorporated sophisticated bandgap engineering and carbon doping in the DBRs for low optical loss and electrical resistance, deep oxidation layers near the active to reduce capacitance, and a reduced mode volume.[28–30] Results from all of the above will be reviewed below.

Most recently, InGaAsSb/AlGaAsSb/GaSb materials for VCSELs and photonic ICs have been studied for emission in the 2–4 μm wavelength range.[31] These materials were grown in our Gen-III machine in collaboration with Prof. Palmstrøm.

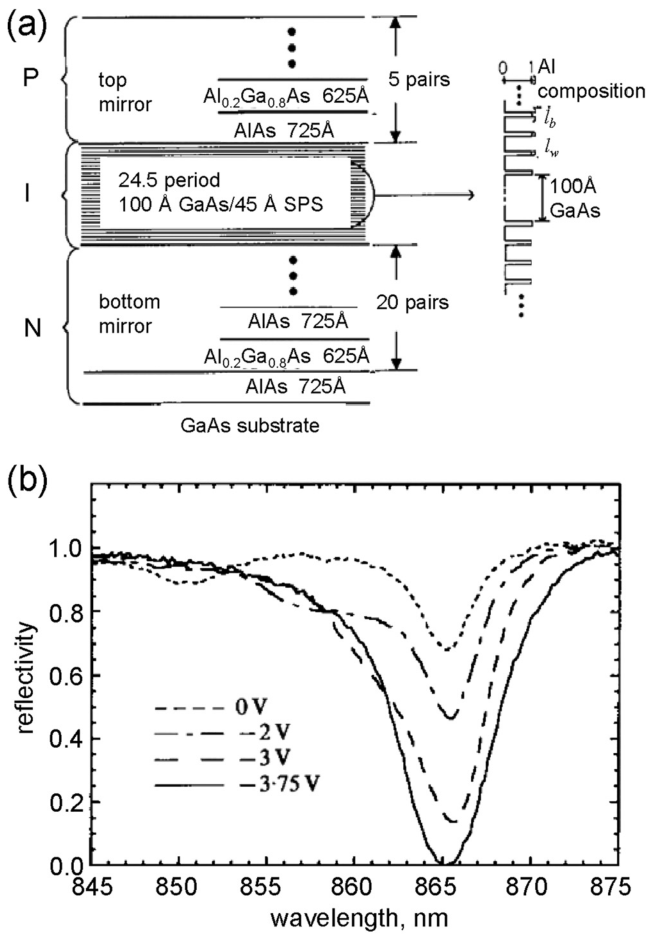

FIG. 3. (a) Schematic of an ASFP reflection modulator with short-period superlattice barriers in the 24.5 period active absorber region, which has 10 nm GaAs quantum wells and SPS barriers that are each a total thickness of 4.5 nm consisting of four $l_b = 0.34$ nm AlAs barrier layers spaced by three $l_w = 1.05$ nm GaAs well layers. The mirrors are similar to Fig. 2. (b) Reflection spectra of the ASFP modulator at the four labeled biases. Adapted with permission from Law *et al.*, Electron. Lett. **27**, 1863 (1991). Copyright 1991, IEE.

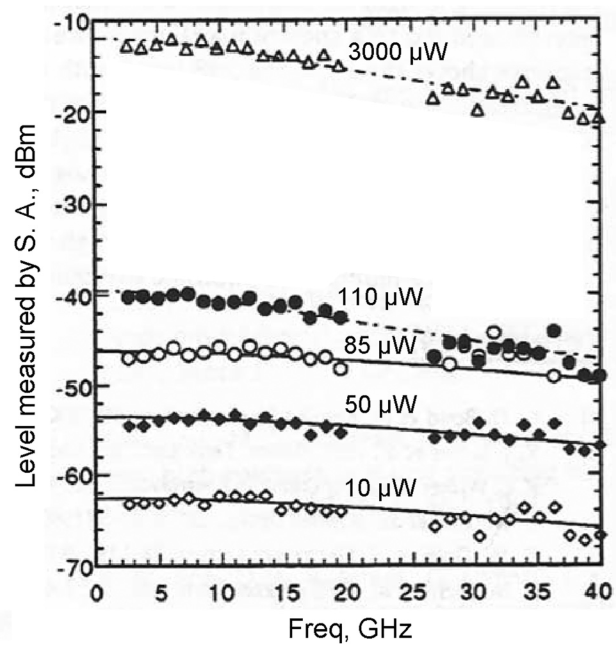

FIG. 4. High-speed, large-signal modulation from an ASFP with mm-wave contact pads, a semi-insulating substrate, a 2-period top mirror, and a 25-period bottom mirror, both containing quarter-wave $AlAs/Al_{0.2}Ga_{0.8}As$ undoped DBR layers. The MQW active has 80 periods of 10 nm GaAs QWs and 4.5 nm $Al_{0.3}Ga_{0.7}As$ barriers. Device lateral dimensions are $16 \times 20\,\mu$m and the cross section is as in Fig. 1(a) except for the addition of *p* and *n* contact layers immediately above and below the MQW active. Data are for increasing incident optical power levels as labeled. Theoretical RC-curve fits have 3 dB cut-offs at 37 GHz (solid) and 18 GHz (dashed). $\lambda = 864$ nm; bias = −12 V. Adapted with permission from *Device Research Conference,* Paper VIB-9, Santa Barbara, Jun. 23,1993 (IEEE, Washington, DC, 1993); *ibid. IEEE LEOS'93*, Paper SP1.2, San Jose, Nov. 15, 1993 (IEEE, Washington, DC, 1993). Copyright 1993, IEEE.

In what follows, I will review the early vertical-cavity modulator results of the late 1980s and early 1990s that helped establish our MQW MBE program at UCSB. Then, I will continue with the early VCSEL work that grew out of the modulator work and required the need for good conduction through the DBR mirrors as well as good carrier injection into the QW active regions. The VCSEL discussion will then continue into the more recent efforts. Finally, I will conclude with what was learned and summarize its impact.

II. RESULTS ON MODULATORS

By the time Prof. Gossard arrived in 1987, my grad student, Rob Simes, had already grown early versions of a multiple-quantum-well (MQW) reflection modulator based on index modulation in our system A. This was accomplished in collaboration with Prof. Gossard and John English while they were still at Bell Labs. The results were submitted to the CLEO conference that Fall.[3] Due to some imbalance, the device exhibited a 2:1 on/off contrast with 25 V of reverse bias and a minimum reflectivity of 15% at a wavelength of 882 nm, which at the time was still state-of-the-art.

With some improvements in the growth as well as moving the Fabry–Pérot resonance closer to the GaAs absorption edge (873 nm), where the QCSE is stronger, the result shown in Fig. 1 was obtained.[4] In this case, the zero-bias reflection was only 3%, the contrast at 25 V was now 8:1, and there was also clear evidence of some absorption in addition to the index shift of the resonance with applied field.

The observation of the absorption effect led one of my students, R. H. Yan, to propose the primary use of absorption in addition to index in an asymmetric Fabry–Pérot (ASFP) reflection modulator design, which could require much lower drive voltage.[5,6] The basic concept is to have a top mirror with modest reflection and a back mirror with a very high reflection, and then add loss to the cavity to make the back mirror "appear" to have a reflection like the front, and thus create a "balanced" cavity for zero reflection. To make it work all that was necessary was to modify the prior design by lengthening the back mirror and shifting the wavelength even closer to the absorption edge of the GaAs MQW. With a couple of iterations, it was found that fewer quantum-wells were needed in the active and thus, even lower voltages were obtainable. Figure 2 gives a result[6] with only 24 quantum wells to lower the necessary drive voltage to 2 V, giving a reflection change of about 40% and an on/off contrast of >15.

Further refinements in the ASFPs included the exploration of novel superlattice active regions. One interesting example is illustrated in Fig. 3.[7] Here, the AlGaAs barriers are replaced by relatively thin (4.5 nm) short-period superlattices (SPS) of AlAs/GaAs, and

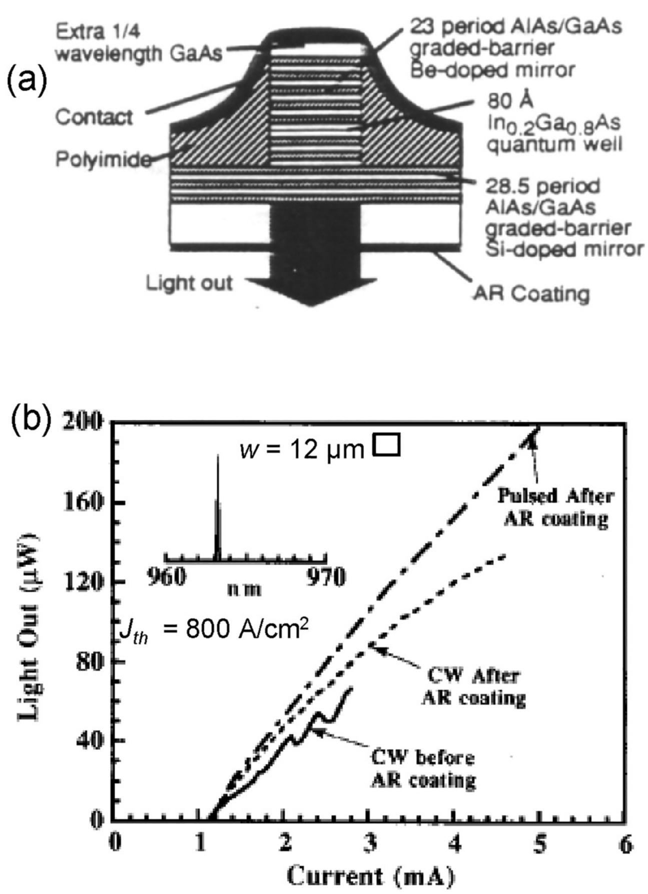

FIG. 5. Initial electrically pumped VCSEL results. (a) Schematic. Top p-doped mirror contained 23 AlAs-GaAs DBR periods; bottom n-doped mirror contained 28.5 AlAs-GaAs periods. Mirror interfaces were graded over 18 nm with digital superlattices. Doping was 4×10^{18}. Cavity had a single 8 nm $In_{0.2}Ga_{0.8}As$ QW surrounded by undoped 50 nm $Al_{0.5}Ga_{0.5}As$ layers on each side, and then this sandwich clad by p- or n-doped 80 nm $Al_{0.5}Ga_{0.5}As$ layers prior to the respective mirrors. (b) Light-out vs current-in results at 963 nm before and after AR-coating—CW, and pulsed after coating. Adapted with permission from Geels *et al.*, *Proceedings of Optical Fiber Communication Conference,* Paper PD31-1, San Francisco, Jan. 24, 1990 (OSA, Washington, DC, 1990). Copyright 1990, OSA.

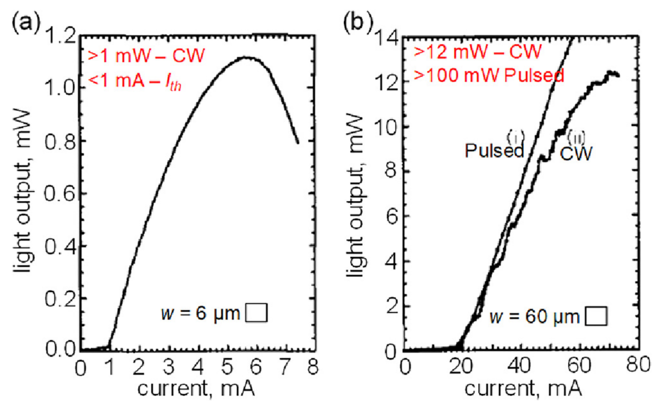

FIG. 6. VCSEL design similar to Fig. 5(a), except the number of periods in the top and bottom DBRs were 16 and 18.5, respectively, and the doping was reduced to 1e18, except in graded interfaces, where it increased to 5e18. Also, three 8 nm thick $In_{0.2}Ga_{0.8}As$ QWs were used. Parts (a) and (b) illustrate light-current results from two square mesa devices measuring either 6 or 60 μm on a side. $\lambda \sim 980$ nm. Adapted with permission from Geels and Coldren, Electron. Lett. **27**, 1984 (1991). Copyright 1991, IEE.

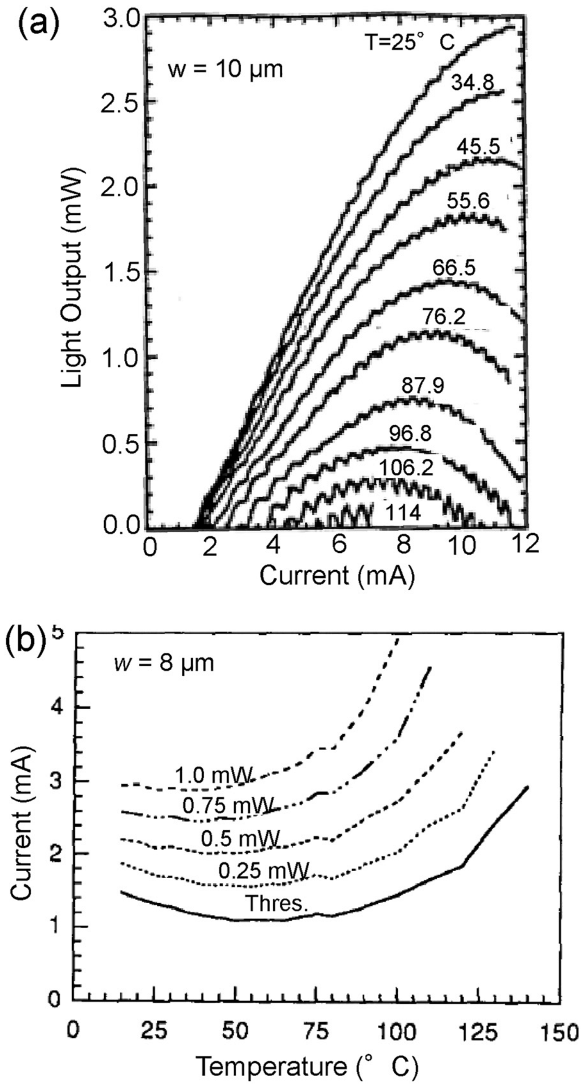

FIG. 7. Offset gain VCSELs. (a) Light-current characteristic for a VCSEL similar to a VCSEL described in Fig. 6, but with some gain offset introduced by slightly adjusting the cavity thickness during MBE growth. Adapted with permission from Geels *et al.*, *Proceedings of Optical Fiber Communication Conference*, Paper WB3, San Jose, Feb. 2,1992 (OSA, Washington, DC, 1992). Copyright 1992, OSA (ripple due to imperfect AR coating). (b) Currents for various powers out for an improved gain-offset VCSEL with top and bottom AlAs-GaAs top and bottom DBRs having 18 and 17.5 periods, respectively, as well as with high-barrier $Al_{0.5}Ga_{0.5}As$ surrounding three $In_{0.185}Ga_{0.815}As$ QWs. The PL emission was at 972 nm, while the cavity mode was at 997 nm at 25 C, yielding a 25 nm gain offset in this case. Adapted with permission from Young *et al.*, IEEE Photonics Technol. Lett. **5**, 129 (1993). Copyright 1993, IEEE.

the resonant wavelength is selected at a point where the absorption is low, the F-P cavity is imbalanced, and the reflection is high at zero bias. Then, as a bias is applied the absorption increases to the point where the cavity is balanced for zero reflection.

These reflection modulators are also capable of very high-speed modulation if designed and fabricated appropriately, because of their inherently low capacitance. To demonstrate this, ASFP devices were grown on semi-insulating substrates with mm-wave probe pads connecting to *intra-cavity p* and *n* contact layers grown immediately above and below the MQW active region. The wafers were then processed so that the probe pads rested only on the semi-insulating substrate with short traces running to the contact layers with the *n*-layer grounded and the *p*-layer to the signal line. The devices were tested with a Ti-sapphire laser, a high-speed photodetector, and a millimeter wave network analyzer. The results, shown in Fig. 4, indicate a 3 dB optical bandwidth of nearly 40 GHz with incident optical powers up to 100 μW. With higher incident powers, carrier generation in the quantum wells reduced the bandwidth to a little less than 20 GHz.[32]

III. RESULTS ON VCSELs

A. Early VCSEL highlights

As outlined in Sec. I above, our initial electrically pumped VCSELs were processed with planarizing polyimide layers around the VCSEL mesa for contacts and silicon nitride antireflecting (AR) coatings on the rear substrate surface for better optical emission. A schematic is shown in Fig. 5 along with the initial results for a 12 μm mesa.[14] The threshold current density of 800 A/cm^2 was the lowest reported for a VCSEL at the time.

As illustrated in Fig. 6, within a year (1991), the VCSEL effort had progressed to where CW output powers were over 1 mW with threshold currents less than 1 mA on small devices, and CW powers on larger devices exceeded 12 mW with pulsed outputs exceeding 100 mW[15] (not shown). Fewer mirror periods

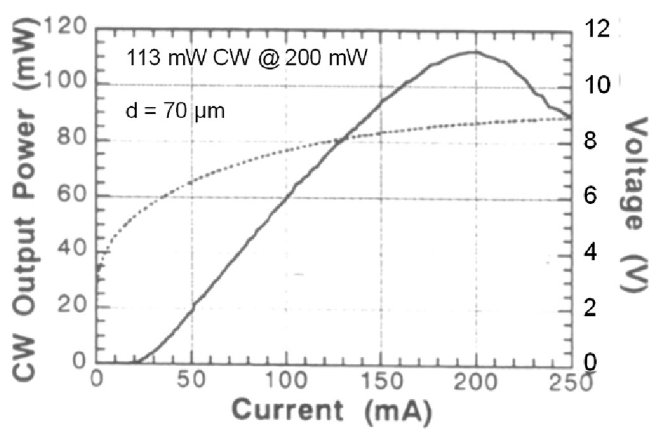

FIG. 8. CW output power and terminal voltage vs current for a 70 μm diameter device from the same material as in Fig. 7(b) mounted on a gold-plated diamond heat sink with indium solder. The diamond was mounted to a brass submount that rested on a thermo-electric cooler. VCSEL thinned to ~100 μm; diamond ~250 μm thick; brass heat sink temperature was 20 °C. Adapted with permission from Peters *et al.*, Electron. Lett. **29**, 200 (1993). Copyright 1993, IEE.

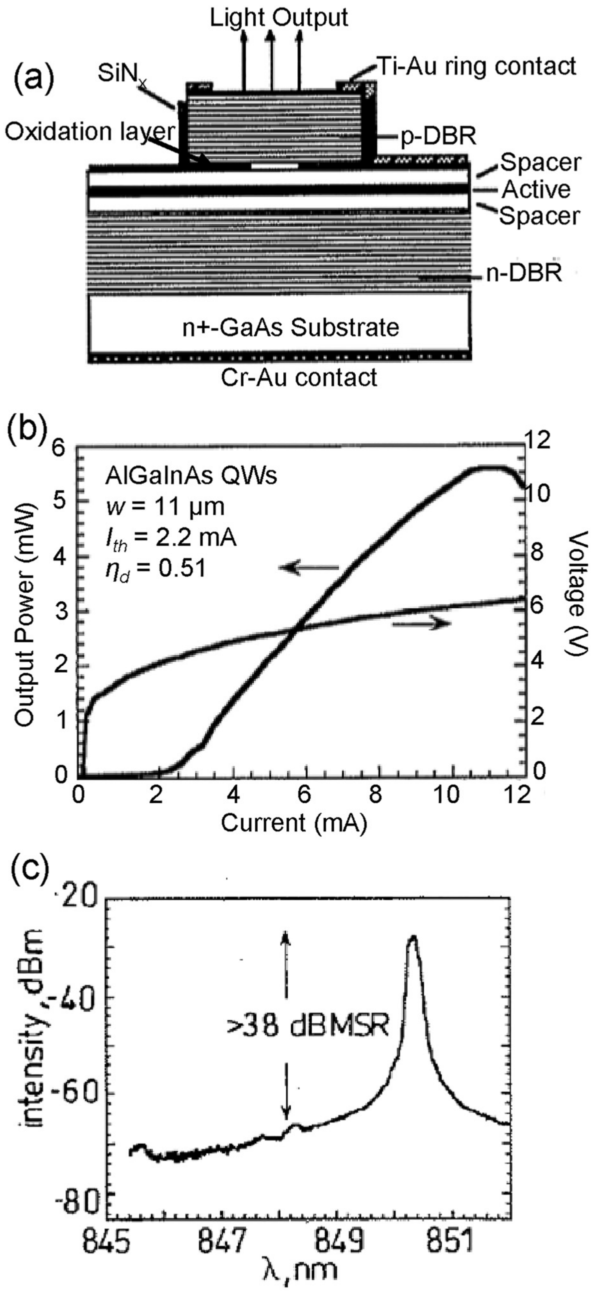

FIG. 9. Initial strained-layer, top-emitting, AlGaInAs QW VCSEL emitting at ∼850 nm. (a) Bottom n-DBR had 25.5 periods of AlAs-$Al_{0.1}Ga_{0.9}As$ and top p-DBR had 19 periods of $Al_{0.9}Ga_{0.1}As$—$Al_{0.1}Ga_{0.9}As$ with graded interfaces. The active MQW used three 8 nm $Al_{0.12}Ga_{0.66}In_{0.22}As$ wells with 50 nm $Al_{0.2}Ga_{0.8}As$ barriers surrounded by 50 nm $Al_{0.3}Ga_{0.7}As$ carrier confinement barriers and $Al_{0.5}Ga_{0.5}As$ layers on each side to complete the one-wavelength cavity. (b) Output power and voltage vs applied current with inset spectrum at twice threshold. (c) Spectrum taken well above threshold. Adapted with permission from Ko *et al.*, *IEEE LEOS Annual Meeting*, Paper TuDD3, Boston, Nov. 19,1996 (IEEE, Washington, DC, 1996). Copyright 1996, IEEE.

with lower doping were used, and three strained active quantum wells were employed.

In another few months, the concept of "gain offset" was introduced to improve the high temperature performance as shown in Fig. 7. This enabled VCSELs to operate to higher temperatures,[16] but importantly, it also provided for nearly temperature independent

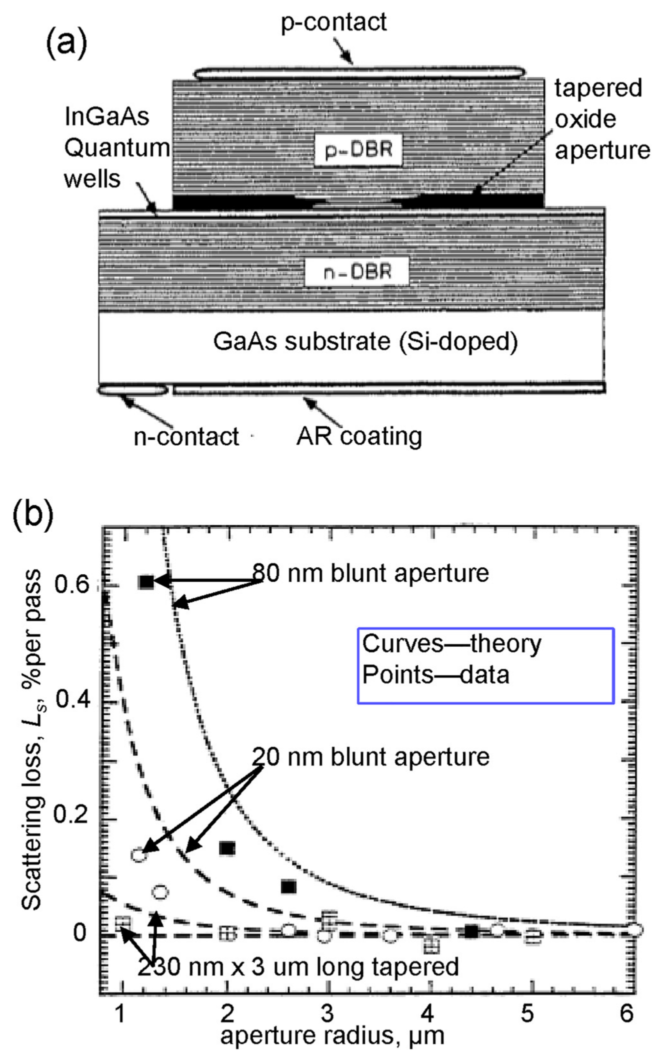

FIG. 10. Theoretical and experimental single pass optical losses in VCSELs with various oxide apertures. [Lowest theoretical dashed curve is for ideal parabolic taper to center of VCSEL—no data provided.] Bottom n-DBR has 18 AlAs-GaAs mirror periods; top p-DBR has 29.5 $Al_{0.67}Ga_{0.33}As$—GaAs periods with interfaces parabolically graded over 22 nm and step doped. Active has three 8 nm $In_{0.18}Ga_{0.82}As$ with 8 nm GaAs barriers. The oxide apertures are above the active before the first mirror layer. Apertures are formed by oxidation of AlAs layers, placed at the standing wave null, next to $Al_{0.9}Ga_{0.1}As$. Oxidation is performed at 450 °C in water-saturated N_2. Adapted with permission from Hegblom *et al.*, IEEE J. Sel. Top. Quantum Electron. **3**, 379 (1997). Copyright 1997, IEEE.

FIG. 11. Microphoto of an 8-wavelength photonic-integrated-emitter (PIE) array. CWDM wavelength spans of ∼33 nm with element powers of ∼2–7 mW were measured @ 15 mA/element (Ref. 23). Modulation speeds of >3 GHz with low crosstalk were also observed with improved electrode patterns. More information is found in Ref. 23.

operation at moderate temperatures.[17,18] This can accomplished because the gain maximum moves toward longer wavelengths about 4× faster (3.3 nm/10 °C) than does the cavity mode (0.8 nm/10 °C); so if the mode is placed at a longer wavelength than the gain maximum at 20 °C, then as the device is heated, the gain maximum moves toward the mode, eventually overtaking it, thereby compensating for the normal reduction in output power with increasing temperatures until it moves past. In part (a), we note that the threshold currents are nearly constant for temperatures from 25 to 45.5 °C, and that the device operates with useful outputs to over 100 °C. In part (b), it is directly shown that the threshold current and the current for some power out does not vary much over a wide temperature range.

Figure 8 illustrates what can be achieved with the same design described and characterized in Fig. 7(b), if the larger chips are mounted to a good heat sink—in this case with a diamond heat spreader. As can be seen, this enables a CW output power of about 113 mW with a room temperature heat sink, again another milestone at the time.[19]

Although strained InGaAs QWs with AlAs-GaAs DBRs proved to give the best VCSEL performance and reliability, the industry adopted an 850 nm wavelength standard due mainly to the existence of fiber that was optimized for this wavelength in the 1990s. Thus, many researchers focused their efforts on GaAs QWs with AlAs-AlGaAs DBRs, which provided VCSELs that emitted at 850 nm, but with reduced performance relative to the strained InGaAs QWs that emitted at ∼980 nm. Therefore, realizing the many advantages of strain, we developed a strained-layer QW technology that added Al to our InGaAs materials to pull the wavelength down to 850 nm.

Figure 9 shows the first VCSEL results published with strained AlGaInAs QWs.[20] This followed work on edge-emitters to perfect the material.[33] These results compared very well to the state-of-the-art for 850 nm VCSELs of the time (1996).[34]

For these results, the n^+ GaAs substrates were misoriented 2° toward <111> to reduce O_2 incorporation, and after growth the wafers were annealed by RTA for 10 s at 900 °C.

With oxide or etched apertures, the current was constricted to a certain diameter above the active region, and it had been observed that lateral optical diffraction and scattering loss was somewhat limited because of the first-order lensing or waveguiding effect it provided.[35] However, a blunt aperture was far from a perfect lens (parabolic index variation) that was known to be needed from prior laser theory. Measurements had shown that optical loss, not due to free-carrier absorption, remained a major limitation on smaller devices. Therefore, we proposed to make this intracavity aperture into a better lens to reduce optical loss.[21]

Figure 10 gives the results of some modeling and data that indicates the potential of using tapered apertures compared to blunt apertures from VCSELs that were fabricated with oxide apertures. The theory uses an iterative mode recirculation algorithm to both find the mode and the round-trip loss.[22] Not surprisingly, the improvement is especially important for smaller radius devices, where diffraction and aperture scattering loss would be particularly large. It is interesting to note that the measured data show more improvement than predicted from the modeling in the case of "blunt" apertures. This is probably due to the fact that there is also some significant tapering on the "blunt" apertures because of the manner in which they are constructed. That is, all of these apertures, and most in the literature, are formed from a layer of high Al content AlGaAs next to a modest Al content AlGaAs.

Because of the layer index requirements in the VCSEL, the Al content in both layers is generally quite high, usually pure AlAs or very high Al-fraction AlGaAs for the high Al layer and close to ∼90% for the adjacent lower Al-fraction layer. Thus, as the high Al content layer oxidizes laterally, the lower Al content layer begins to oxidize vertically from the already oxidized layer. For example, if the lower Al content layer oxidizes at only 5% of the rate of the higher Al-content layer (the approximate ratio for 90% compared to 100%Al), we can see that it will oxidize vertically 100 nm at the edge of the sample for every 2000 nm the high Al-content layer oxidizes laterally, and it tapers linearly to the end of this high Al-content layer—so if we began with a 20 nm high Al content layer thickness, after 2000 nm of lateral oxidation, we will have a oxide taper from 20 to 120 nm in thickness over 2 μm. This is a significant taper!

A number of novel geometries were explored during the 1990s to respond to the expanding demand for data bandwidth and VCSEL performance needed for Datacom. Figure 11 shows a multiwavelength VCSEL array with eight different wavelength emitters all integrated within a 60 μm diameter, so that eight data channels could be simultaneously launched into a 60 μm core multimode fiber simply by butt-coupling this VCSEL to it.[23] Corresponding resonant-cavity detector arrays, analogous to the asymmetric resonant-cavity modulators in Sec. II above were also investigated.[36] (Note that each wavelength channel experiences ∼9 dB inherent loss in this scheme.)

In order to make such devices, the MBE growth of the VCSELs was interrupted following growth of the active region and

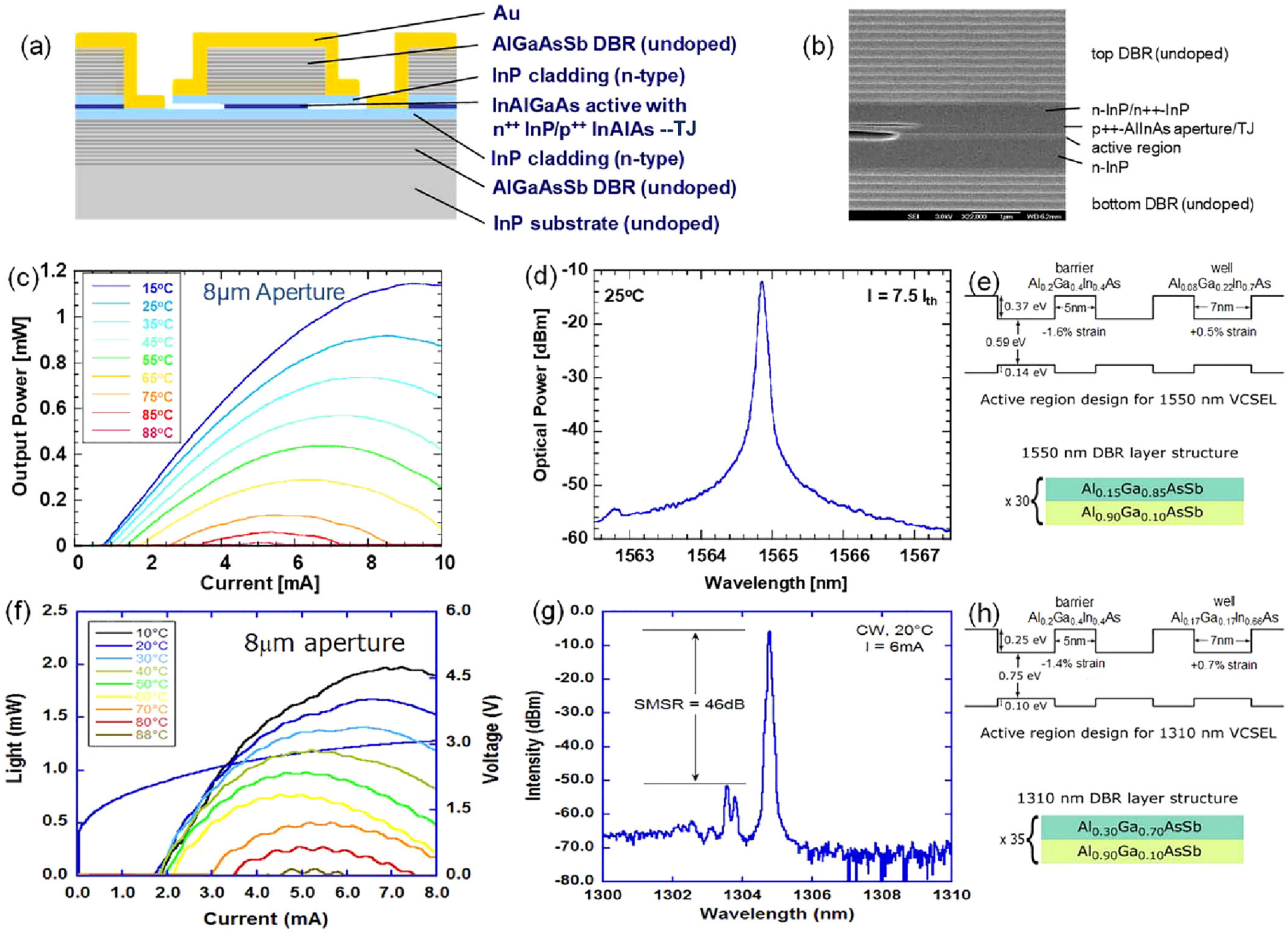

FIG. 12. InP-based 1310 and 1550 nm all-epitaxially grown VCSELs by MBE. (a) Schematic showing layers, mesa etching, and underetching following oxidation; (b) SEM cross section showing separate oxidation of AlInAs tunnel junction (TJ) layer and active region; (c) power-out vs current-in for a range of temperatures up to 88 °C for the VCSEL characterized by the spectrum in (d) (Ref. 24) that peaks at ∼1565 nm at 25 °C; (e) active MQW and DBR mirror designs for (c) and (d); (f) power-out vs current-in for a range of temperatures up to 88 °C for the device characterized by the spectrum in (g) (Ref. 25) that peaks at 1305 nm at 20 °C; (h) active MQW and DBR mirror designs for (f) and (g). More information is found in Refs. 24 and 25.

first four top AlAs-GaAs mirror periods. The fourth GaAs mirror layer was grown 0.91 λ thick instead of 0.25 λ thick measured in the medium. Then, to get the eight different effective cavity lengths, this layer was successively patterned and very accurately etched using a three-level binary-coded anodic etching process over the VCSEL areas. Next, the wafer was reinserted into the MBE and the rest of the top mirror layers completed. Finally, the VCSEL array elements were completed in parallel in a single process sequence as used for other oxide-apertured VCSELs.

B. More recent VCSEL highlights

At the turn of the 21st century, it seemed clear that in-plane cavity, edge-emitters would dominate the long-haul communications and high-power sensor marketplace. It also seemed clear that such high-performance components would tend to be high-cost and the market volume low. However, there still appeared to be the higher-volume short-to-medium-haul Datacom market, the longer-distance data-center market, and the lower-power sensor market, which all used single-mode fibers, that might support an effort on 1310 and 1550 nm VCSELs. Although there had been some successful work with wafer-bonded[37] and dielectric-mirror VCSELs[38] that operated in this range, we believed an all-epitaxial device that could mimic our successes with the shorter wavelength work would be worth exploring.

Thus, we designed and began to grow all-epitaxial AlGaAsSb/AlGaInAs/InP VCSELs by MBE. Given existing experience at UCSB with growing the antimonides in our system-B,[39] the quaternaries

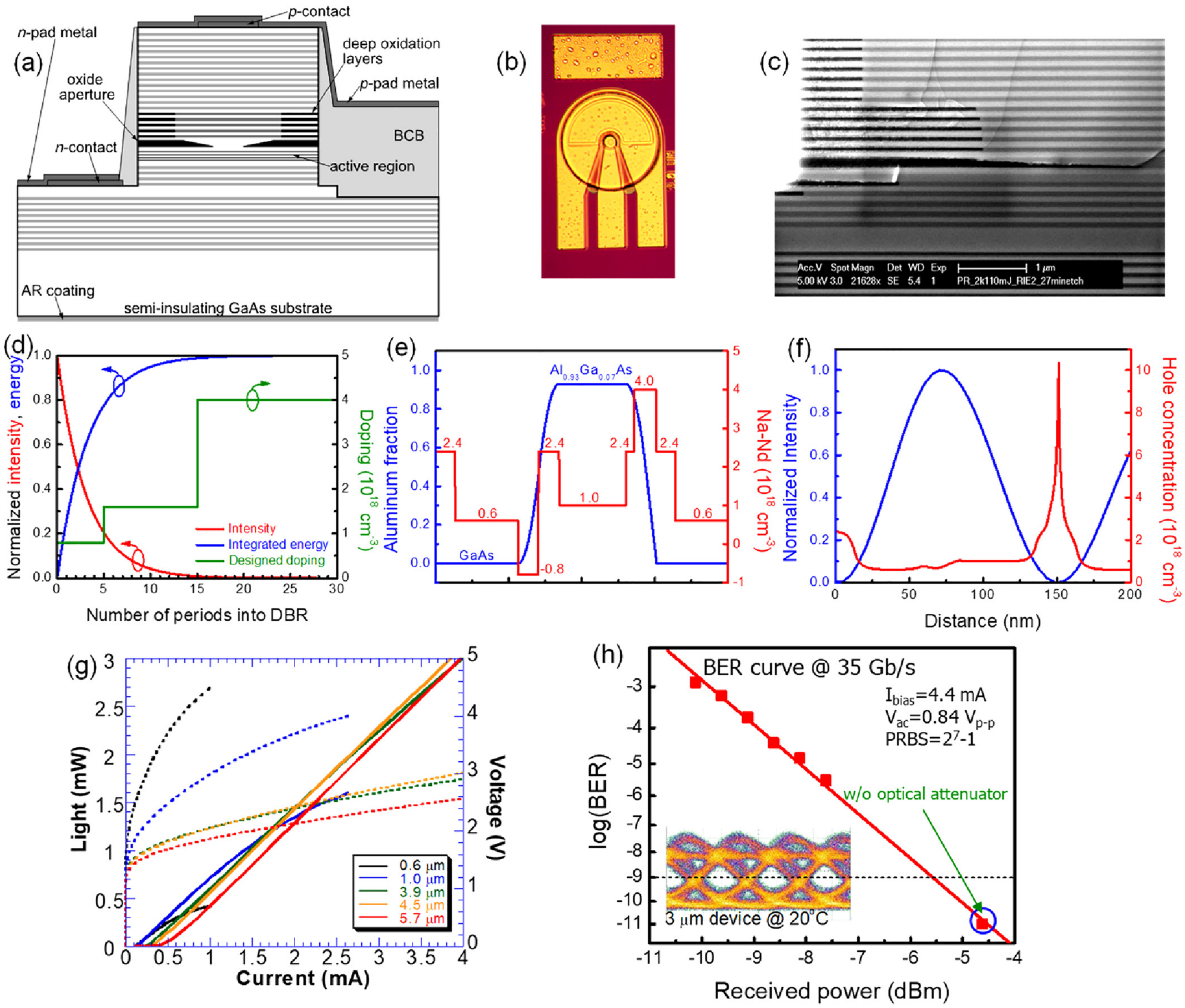

FIG. 13. (a) Schematic of high-speed, high-efficiency VCSEL @ 980 nm. (b) Microphoto of top metallization. (c) SEM cross section showing depths of wet oxidation in mirrors, deep oxidation layers and tapered aperture; top p-DBR mirror has 25 periods of $Al_{0.85}Ga_{0.15}As$-GaAs on top of five periods of $Al_{0.93}Ga_{0.07}As$-GaAs for deep oxidation; aperture layer is $\lambda/2$ thick with $Al_{0.93}Ga_{0.07}As$ on top of 20 nm of AlAs; active has high-barrier $Al_{0.5}Ga_{0.5}As$ layers surrounding three 8 nm $In_{0.185}Ga_{0.815}As$ QWs with 8 nm GaAs barriers; the bottom DBR mirror first has 4 periods of n-doped $Al_{0.9}Ga_{0.1}As$-GaAs, then a 5/4-λ n^+ contact layer, and finally 14 periods of undoped AlAs-GaAs. (d) Designed doping, optical intensity, and integrated energy vs number of periods into the top p-DBR. (e) Designed doping over one p-mirror period. (f) Hole concentration and optical mode intensity over one p-mirror period. (g) Optical output and terminal voltage vs current in for five different device diameters. (h) Log bit-error-rate vs received power and inset eye-diagram @ 35 Gb/s for a 3 μm device. As described in Ref. 29.

were not a major challenge, especially with Prof. Gossard's contributions to digital superlattices.[40] Actually, growing the InP on top of many micrometers of the quaternaries was a bit more difficult, given that InP cannot adjust its lattice constant very much.

Figure 12 gives results for both 1310 (actually 1305 nm)[25] and 1550 (actually 1565 nm)[24] AlGaAsSb-DBR/AlGaInAs-Active/InP VCSELs. They have a number of that features enable high-yield, high-performance VCSELs with potential low-manufacturing costs.

Key features include (1) high-index-of-refraction differences within the Sb-based DBR mirrors, which give nearly the same index contrast as for the AlGaAs system @ 850 nm; (2) embedded $n^{++}InP/p^{++}AlInAs$ tunnel junctions just above the MQW active

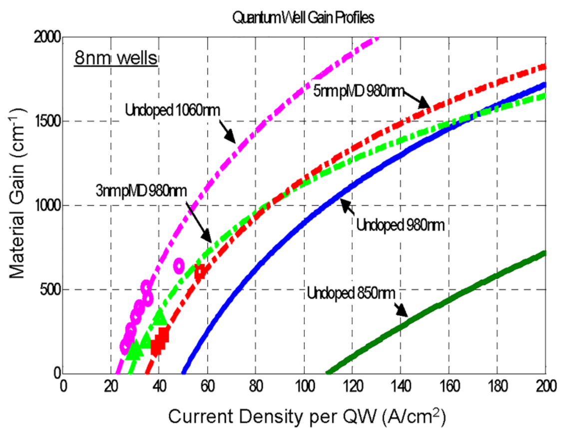

FIG. 14. Material gain of 8 nm quantum wells of GaAs/AlGaAs (green-solid) and strained InGaAs/GaAs; gain only measured at lower quantum state with little population in upper state. p-type modulation doping (pMD) of the 8 nm GaAs barriers between and beside the InGaAs 980 nm wells by doping at 2e18 over either 3 or 5 nm in barrier center. Adapted with permission from Coldren *et al.*, *Proceedings of IEEE Photonics Society Summer Topical Meeting*, Paper TuD2.1, Playa Del Carmen, Mexico, July 19, 2010 (IEEE, Washington, DC, 2010). Copyright 2010, IEEE.

region that enables two binary n-type InP cladding/contact layers for both low electrical and thermal resistance to the active area as well as undoped mirrors; (3) built-in aperturing layers with the AlInAs tunnel junction and high-Al fraction AlGaInAs active barriers for low optical loss and little current spreading; and (4) a single all-epitaxial growth step to avoid complex multistep bonding or critical postdeposition processes for mirrors.

Meanwhile, high-volume shorter distance links (≤30 m) with multimode fibers (or even printed waveguides on circuit boards) for Datacom and interconnects within supercomputers or switching racks called for low-cost, high-speed, high-efficiency shorter wavelength VCSELs. Thus, an effort was established to make the highest-speed, highest-efficiency VCSEL using all of the tricks developed previously as well as a new CB_4 doping system for low-diffusion high-carbon doping in our newest Gen-III system.

Figure 13 summarizes some of the design aspects and results for these new VCSELs.[28–30] As can be seen, some sophisticated bandgap engineering and modulation doping was incorporated to reduce the p-mirror resistance without increasing optical loss. Also, intracavity deep-oxidation layers were added by increasing the aluminum fraction in the first five mirror layers from 85% to 93% to increase the lateral oxidation by about 3× and thereby reduce capacitance without decreasing the contact resistance. In addition,

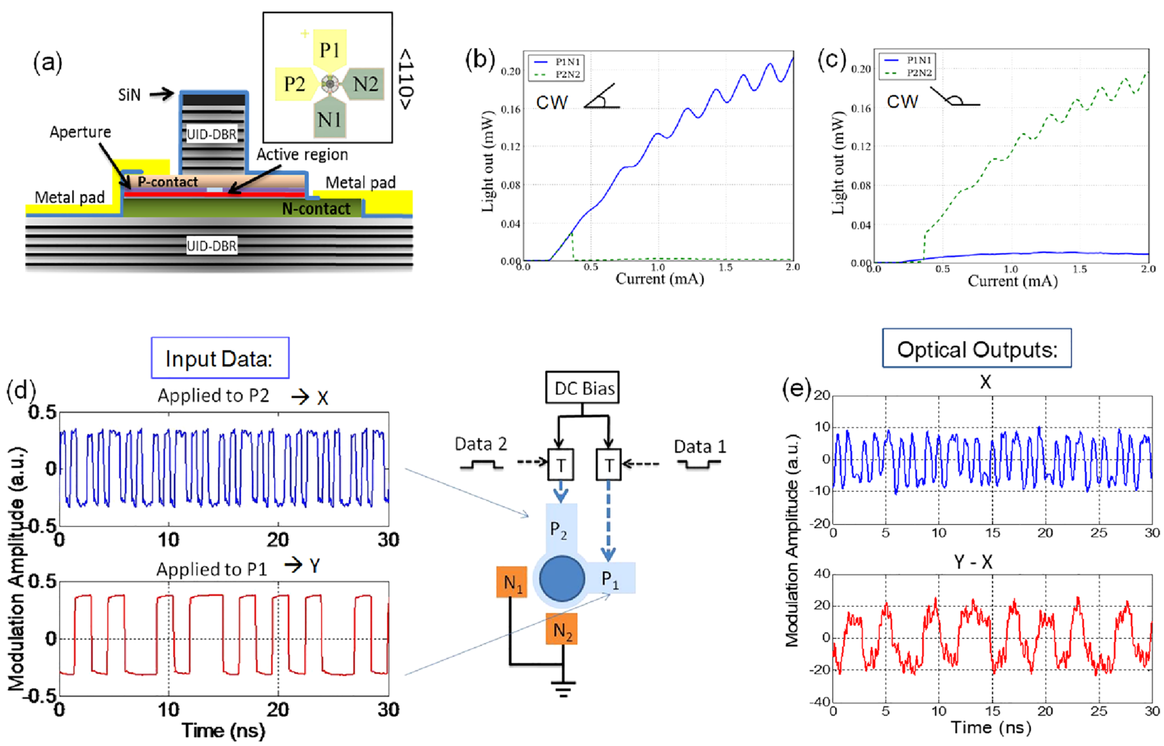

FIG. 15. Multiterminal polarization-modulated VCSEL. (a) Schematic cross section and top labeling of electrodes for the two channels; (b) light-out in two orthogonal polarizations vs current-in for current applied across P1-N1; (c) light-out in two orthogonal polarizations vs current-in for current applied across P2-N2; (d) data applied to two electrode pairs and schematic of experiment; (e) optical outputs: X is on polarization as in (c)—a replica of the signal to P2; however, the operation Y-X is required to remove crosstalk from the orthogonal polarization as in (b) to obtain a replica of the signal to P1. (a)–(c) described in Ref. 26; (d) and (e) described in Ref. 27.

the tapered aperture was made somewhat blunter than the 3 μm long design illustrated in Fig. 11 for a smaller optical mode by increasing the composition of the aluminum to 93% in the AlGaAs next to the AlAs that leads the oxidized aperture point. All of these features improve efficiency and modulation speed.

At the time of initial publication (2007), the data rate efficiency of 286 fJ/bit was a new record for a VCSEL,[28] and this record stood for four years.[41] A few years later (2010), a similar device was used in a full link test at IBM, and the full-link value (without timing recovery) was 0.9 pJ/bit, also a new milestone.[42]

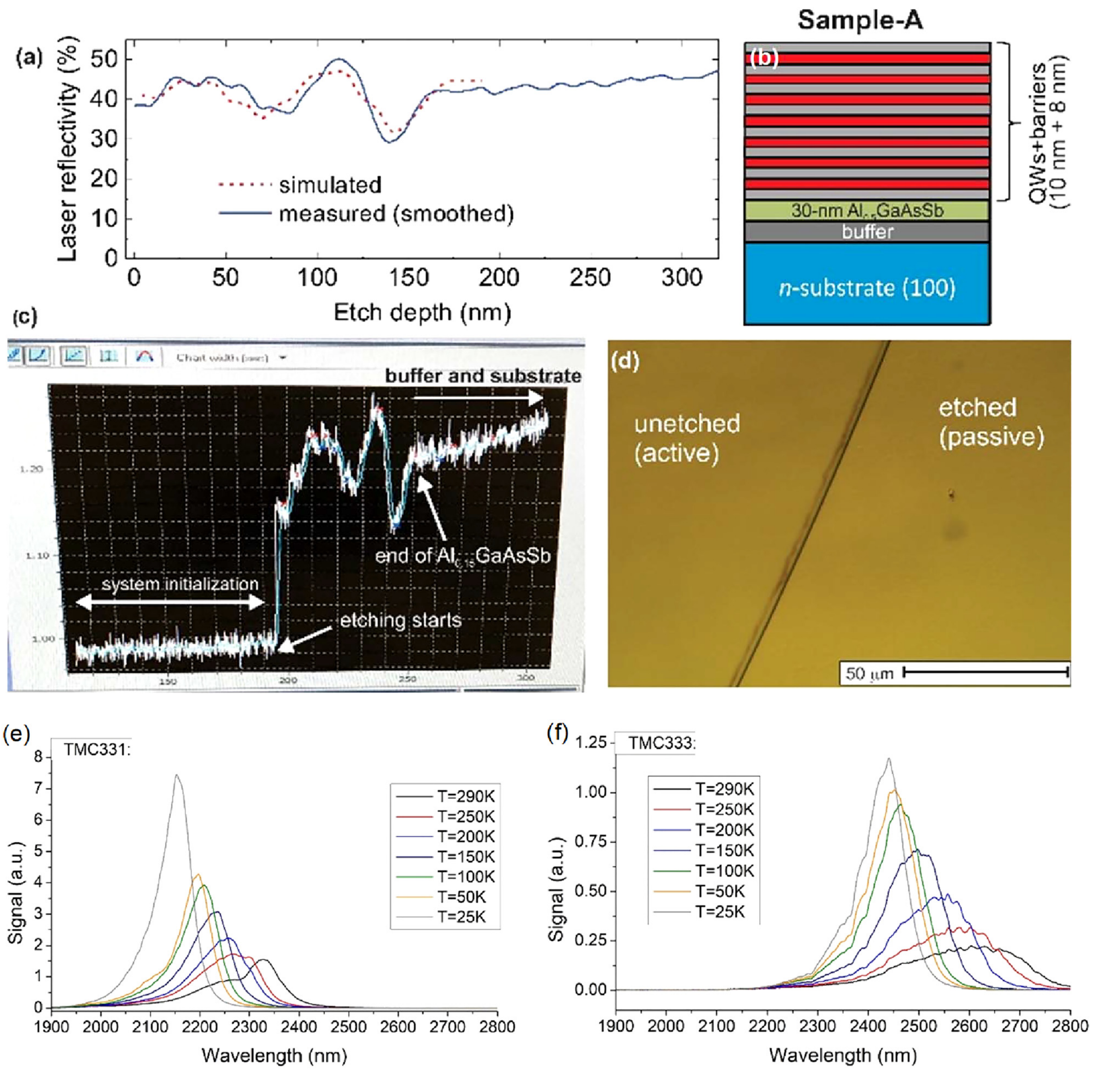

FIG. 16. Selective dry etching of MQW active from AlGaAsSb/GaSb and PL spectra. (a) Comparison of simulation and experimental laser reflectivity monitor data for Cl_2/N_2 reactive-ion-etching of the MQW layers; (b) schematic of grown samples containing seven MQW periods with 10 nm $In_{0.53}Ga_{0.47}As_ySb_{1-y}$ wells and 8 nm GaSb barriers with a final 350 nm layer of GaSb followed by an $Al_{0.5}Ga_{0.5}AsSb$ lower cladding/end-etch layer; (c) actual laser-monitor data (note larger time window); (d) microphoto of wafer surface comparing etched and unetched regions; (e) active-region PL spectra at various temperatures for the test sample; and (f) PL spectra for a sample with a higher In fraction in the QWs. [(a)–(d): Adapted with permission from Arafin *et al.*, Opt. Mater. Express **9**, 1786 (2019). Copyright 2019, OSA; (e)–(f): unpublished].

The data-rate-efficiency record of ~160 fJ/bit set by Furukawa in 2011[41] was short lived, since this was then one of the recognized figures-of-merit to satisfy the increasing demand for improved data-link efficiency both in data centers and super computers. Accordingly, VCSELs with efficiencies of 81 fJ/bit[43] and then 69 fJ/bit[44] soon followed later in 2011 and 2012, respectively, from the TU-Berlin/VI-Systems team.

The Furukawa result benefitted from the use of a 1060 nm highly strained InGaAs MQW active.[41] In fact, as summarized in Fig. 14, we had done an earlier MBE study of highly strained and modulation-doped quantum-well gain regions to identify candidates for improved optical modulation speed and efficiency,[45] which clearly pointed out that the most highly strained InGaAs quantum wells at 1060 nm would require about half the current for a given gain as well as provide significant increases in the differential gain. In a laser, the maximum modulation frequency is proportional to the square root of the differential gain, and the threshold current would almost be halved in switching from 980 to 1060 nm.[46] This explains the Furukawa result.

Another method of increasing bit rate on a single optical beam is the use both polarizations. In order to avoid polarization multiplexing hardware and to do this in a single device, switching between VCSEL polarizations as well as the modulation of the individual polarizations was explored. As others had investigated,[47] we utilized the concept of asymmetric current injection to attempt to distort the carrier k-vector distribution in the quantum-well gain regions, and thus, to introduce some gain anisotropy and thereby favor a particular lasing polarization.

Figure 15 summarizes some of the design concepts and results.[26,27] As shown in part (a), four electrodes are used with pairs of p- and n-contacts opposite each other to intracavity contacts together with some degree of electrical isolation to implement some degree of lateral current flow in the active region. As the data shows, the CW optical polarization can be switched by switching currents between the two pairs of contacts, but more importantly, two different data streams can be simultaneously applied to the two pairs of contacts, and then be remotely deciphered. This experiment suggested that up to 16 Gb/s might be transmitted by such a multiterminal VCSEL, even though it was parasitically bandwidth limited to a single-channel bit rate of 8 Gb/s in this case.[27]

The most recent effort that my group led was in direct collaboration with Prof. Palmstrøm to fabricate short-wave infrared (SWIR) lasers based on GaSb, initially in the 2–3 μm wavelength range. InGaAsSb/AlGaAsSb/GaSb MQW gain regions and AlAsSb/GaSb DBR mirrors were considered for VCSELs and this same MQW gain region with AlGaAsSb cladding regions were considered for edge-emitters. Figure 16 summarizes some results of growth and processing.[31] The Gen-III system was again employed. Smooth layers with good photoluminescence were grown and the necessary processing technology for lasers was also developed.

IV. SUMMARY AND CONCLUSIONS

In this paper, I have reviewed a segment of the work that Prof. Arthur Gossard has enabled while at UC-Santa Barbara—some highlights of work on vertical-cavity modulators and lasers, all-epitaxially grown by MBE. Although Art was not always a coauthor on the published papers, his contributions in guiding the graduate students and postdocs as well as in keeping the MBE lab running extremely well were always key to the success of the projects.

Although *JVST* guidelines mention that one should avoid claims that results are the *first* or have the *best* characteristics in some important recognized aspect at the time of reporting, I have endeavored to limit the selection of highlighted results to only those that must be described in this manner for accuracy. My goal is to point out that Prof. Gossard has enabled some highly impactful work that has had and continues to have a major influence in our scientific and business communities. For example, VCSELs have penetrated many markets today, and the volume of sales is measured in the tens of millions of devices per month. Many of the designs developed and demonstrated in Art's MBE lab are incorporated within these devices, and moreover, many of the student coauthors referenced in this paper are either in leadership positions or are directly producing such products within the major manufacturers today. Many others who worked in Art's MBE lab can also be added to that group.

Art continues to be involved in a number of important MBE projects as outlined in other papers in this issue.

ACKNOWLEDGMENTS

Although this paper focuses on the contributions of Gossard, I also want to acknowledge the extremely important contributions of John English in training and mentoring all of the graduate students involved with MBE growth as well as his many scientific contributions to the research reported. I want to acknowledge funding support from AFOSR for the modulator work, and DARPA-MTO via the Optoelectronics Technology Center for supporting much of the VCSEL work. Funding from and collaboration with Honeywell, Raytheon, IBM, Hewlett-Packard, and Rockwell Scientific are gratefully acknowledged as well.

DATA AVAILABILITY

Data sharing is not applicable to this article as no new data were created or analyzed in this study.

REFERENCES

[1] G. D. Boyd, D. A. B. Miller, D. S. Chemla, S. L. McCall, A. C. Gossard, and J. H. English, Appl. Phys. Lett. **50**, 1119 (1987).

[2] D. A. B. Miller, Opt. Eng. **26**, 368 (1987).

[3] R. J. Simes, R. H. Yan, R. Geels, L. A. Coldren, J. H. English, and A. C. Gossard, *CLEO'88,* Paper TuE2, Anaheim, Apr. 26, 1988 (OSA, Washington, DC, 1988).

[4] R. J. Simes, R. H. Yan, R. Geels, L. A. Coldren, J. H. English, A. C. Gossard, and D. G. Lishan, Appl. Phys. Lett. **53**, 637 (1988).

[5] R. H. Yan, R. J. Simes, and L. A. Coldren, IEEE Photonics Technol. Lett. **1**, 273 (1989).

[6] R. H. Yan, R. J. Simes, L. A. Coldren, and A. C. Gossard, Appl. Phys. Lett. **56**, 1626 (1990).

[7] K. K. Law, M. Whitehead, J. L. Merz, and L. A. Coldren, Electron. Lett. **27**, 1863 (1991).

[8] D. A. B. Miller, D. S. Chemla, T. C. Damen, A. C. Gossard, W. Wiegmann, T. H. Wood, and C. A. Burrus, Phys. Rev. Lett. **53**, 2173 (1984).

[9]R. Geels, R. H. Yan, J. W. Scott, S. W. Corzine, R. J. Simes, and L. A. Coldren, *Proceedings of Conference on Lasers and Electro-Optics*, Paper WM1, Anaheim, Apr. 27, 1988 (OSA, Washington, DC, 1988).
[10]S. W. Corzine, R. Geels, J. W. Scott, and L. A. Coldren, *Proceedings of IEEE Lasers & Electro-Optics Society Annual Meeting*, Paper OE1.2, Santa Clara, Nov. 2, 1988 (IEEE, Washington, DC, 1988).
[11]L. A. Coldren, J. W. Scott, and R. H. Yan, U.S. patent 4,873,696 (10 October 1989).
[12]S. W. Corzine, R. S. Geels, J. W. Scott, R. H. Yan, and L. A. Coldren, IEEE J. Quantum Electron. **25**, 1513 (1989).
[13]J. L. Jewell, A. Scherer, S. L. McCall, Y. H. Lee, S. J. Walker, J. P. Harbison, and L. T. Florez, Electron. Lett. **25**, 1123 (1989).
[14]R. S. Geels, S. W. Corzine, J. W. Scott, D. B. Young, and L. A. Coldren, *Proceedings of Optical Fiber Communication Conference*, Paper PD31-1, San Francisco, Jan. 24, 1990 (OSA, Washington, DC, 1990).
[15]R. S. Geels and L. A. Coldren, Electron. Lett. **27**, 1984 (1991).
[16]R. S. Geels, S. W. Corzine, B. Thibeault, and L. A. Coldren, *Proceedings of Optical Fiber Communication Conference*, Paper WB3, San Jose, Feb. 2, 1992 X473 (OSA, Washington, DC, 1992).
[17]S. W. Corzine, J. W. Scott, R. S. Geels, D. B. Young, B. Thibeault, M. Peters, and L. A. Coldren, *Proceedings of IEEE LEOS Summer Topical Meeting on Optics*, Paper ThB5, Santa Barbara, Aug. 7, 1992 (IEEE, Washington, DC).
[18]D. B. Young, J. W. Scott, F. H. Peters, B. J. Thibeault, S. W. Corzine, M. G. Peters, S. L. Lee, and L. A. Coldren, IEEE Photonics Technol. Lett. **5**, 129 (1993).
[19]F. H. Peters, M. G. Peters, D. B. Young, J. W. Scott, B. J. Thibeault, S. W. Corzine, and L. A. Coldren, Electron. Lett. **29**, 200 (1993).
[20]J. Ko, B. J. Thibeault, Y. Akulova, E. R. Hegblom, D. B. Young, and L. A. Coldren, *IEEE LEOS Annual Meeting*, Paper TuDD3, Boston, Nov. 19, 1996 (IEEE, Washington, DC, 1996).
[21]L. A. Coldren, B. J. Thibeault, E. R. Hegblom, G. B. Thompson, and J. W. Scott, Appl. Phys. Lett. **68**, 313 (1996).
[22]E. R. Hegblom, D. I. Babic, B. J. Thibeault, and L. A. Coldren, IEEE J. Sel. Top. Quantum Electron. **3**, 379 (1997).
[23]S. Y. Hu, J. Ko, and L. A. Coldren, IEEE Photonics Technol. Lett. **10**, 766 (1998).
[24]S. Nakagawa, E. Hall, G. Almuneau, J. K. Kim, D. A. Buell, H. Kroemer, and L. A. Coldren, Appl. Phys. Lett. **78**, 1337 (2001).
[25]D. Feezell, L. A. Johansson, D. A. Buell, and L. A. Coldren, IEEE Photonics Technol. Lett. **17**, 2253 (2005).
[26]Y. Zheng, C. H. Lin, and L. A. Coldren, Electron. Lett. **46**, 1619 (2010).
[27]A. V. Barve, A. Mehta, A. Husain, and L. A. Coldren, *IEEE Optical Interconnects Conference*, Paper TuC5, San Diego, May 5, 2014 (IEEE, Washington, DC).
[28]Y. C. Chang, C. S. Wang, and L. A. Coldren, Electron. Lett. **43**, 1022 (2007).
[29]Y.-C. Chang and L. A. Coldren, IEEE J. Spec. Top. Quantum Electron. **15**, 704 (2009).
[30]Y. C. Chang and L. A. Coldren, U.S. patent 7,916,768 B2 (29 March 2011).
[31]S. Arafin, A. P. McFadden, B. Paul, S. M. N. Hasan, J. A. Gupta, C. J. Palmstrøm, and L. A. Coldren, Opt. Mater. Express **9**, 1786 (2019).
[32]C. C. Barron, C. J. Mahon, B. J. Thibeault, G. Wang, J. R. Karin, L. A. Coldren, and J. E. Bowers, *Device Research Conference*, Paper VIB-9, Santa Barbara, Jun. 23,1993 (IEEE, Washington, DC, 1993); *ibid. IEEE LEOS'93*, Paper SP1.2, San Jose, Nov. 15, 1993 (IEEE, Washington, DC, 1993).
[33]J. Ko, M. J. Mondry, D. B. Young, S. Y. Hu, L. A. Coldren, and A. C. Gossard, Electron. Lett. **32**, 351 (1996).
[34]J. K. Guenter, R. A. Hawthorne, D. N. Granville, M. K. Hibbs-Brenner, and R. A. Morgan, Proc. SPIE **2683**, 102 (1996).
[35]K. L. Lear, K. D. Choquette, R. P. Schneider, and S. P. Kilcoyne, Appl. Phys. Lett. **66**, 2616 (1995).
[36]O. Sjolund, D. A. Louderback, E. R. Hegblom, J. Ko, and L. A. Coldren, IEEE J. Quantum Electron. **35**, 1015 (1999).
[37]N. M. Margalit *et al.*, IEEE J. Sel. Top. Quantum Electron. **3**, 359 (1997).
[38]Y. Qian, Z. H. Zhu, Y. H. Lo, D. L. Huffaker, D. G. Deppe, H. Q. Hou, B. E. Hammons, W. Lin, and Y. K. Tu, IEEE Photonics Technol. Lett. **9**, 866 (1997).
[39]G. Tuttle, H. Kroemer, and J. H. English, J. Appl. Phys. **67**, 3032 (1990).
[40]M. Sundaram, A. Wixforth, R. S. Geels, A. C. Gossard, and J. H. English, J. Vac. Sci. Technol. B **9**, 1524 (1991).
[41]S. Imai *et al.*, IEEE J. Sel. Top. Quantum Electron. **17**, 1614 (2011).
[42]S. Nakagawa, *Industrial Forum—Asia Conference on Photonics (ACP2011)*, Shanghai, China, Nov. 13, 2011 (OSA, Washington, DC, 2011).
[43]P. Moser, W. Hofmann, P. Wolf, J. A. Lott, G. Larisch, A. Payusov, N. N. Ledentsov, and D. Bimberg, Appl. Phys. Lett. **98**, 231106 (2011).
[44]P. Moser, J. A. Lott, P. Wolf, G. Larisch, A. Payusov, G. Fiol, N. N. Ledentsov, W. Hofmann, and D. Bimberg, Proc. SPIE **8276**, 82760J (2012).
[45]L. A. Coldren, Y. C. Chang, Y. Zheng, and C. H. Lin, *Proceedings of IEEE Photonics Society Summer Topical Meeting*, Paper TuD2.1, Playa Del Carmen, Mexico, Jul. 19, 2010 (IEEE, Washington, DC, 2010).
[46]L. A. Coldren, S. W. Corzine, and M. Mašanović, *Diode Lasers and Photonic Integrated Circuits*, 2nd ed. (Wiley, NY, 2012), Chap. 5.
[47]L. M. Augustin, E. Smalbrugge, K. D. Choquette, F. Karouta, R. C. Strijbos, G. Verschaffelt, E. J. Geluk, T. G. van de Roer, and H. Thienpont, IEEE Photon. Technol. Lett. **16**, 708 (2004).

Monolithic Indium Phosphide Dual Laser Photonic Integrated Circuit for Remote Sensing Lidar

Joseph Fridlander[1], Fengqiao Sang[1], Victoria Rosborough[1], Simone Tommaso Šuran Brunelli[1], Jeffrey Chen[2], Kenji Numata[2], Stephan Kawa[2], Mark Stephen[2], Larry Coldren[1], Jonathan Klamkin[1]

[1]*Electrical and Computer Engineering Department, University of California Santa Barbara, Santa Barbara, CA 93106 USA*

[2]*NASA Goddard Space Flight Center, Greenbelt, MD 20771 USA*

Abstract: A dual laser indium phosphide photonic integrated circuit for remote sensing lidar was realized. A twentyfold improvement in the long-term frequency stability of the master laser was demonstrated using an on-chip phase modulator.

1. Introduction

Integrated path differential absorption (IPDA) lidar is an active remote sensing lidar commonly used for earth science and sensing of trace gases in the atmosphere [1]. To enable deployment on smaller space platforms and subsequently more frequent science and monitoring, compact implementations will be required. The indium phosphide (InP) photonic integrated circuit (PIC) platform is ideal for this application [2]. In this work, we have designed and fabricated a monolithic InP PIC with an IPDA architecture suitable for monitoring carbon dioxide (CO_2) sources and sinks by stepping through multiple points across an absorption line at a wavelength of 1572.335 nm [3].

By engineering the epitaxial structure and laser gratings, InP PICs can be used for IPDA lidar over a broad range of wavelengths that include the O, C, and L optical bands. Furthermore, several photonic devices can be monolithically integrated with lasers, thus significantly reducing system cost, size, weight, and power compared to lidar counterparts constructed from stand-alone discrete optical components. Here we report the subsystem operation of our fabricated InP lidar PIC onto which we have monolithically integrated two sampled grating distributed Bragg reflector (SGDBR) lasers, a phase modulator (PM), and a pulse carver [4,5].

2. Test Setup and Measurement

Figure 1 shows a simplified block diagram of the IPDA lidar PIC and subsystem test setup. An SGDBR master laser (ML) is stabilized using a frequency modulation technique [6] utilizing an on-chip PM. The PM is modulated at 125 MHz and a modulation depth of π. Frequency modulated light is coupled off chip to a CO_2 gas cell reference using a lensed fiber. Coherent phase detection of a beat note generates an error signal proportional to the frequency deviation from the line center. The filtered error is fed back to the ML phase section to correct the laser wavelength.

Figure 2(a) shows the PM efficiency at a 10 mA forward bias with a comparison to a commercial-off-the-shelf lithium niobate PM. The efficiency is measured using a fiber coupled setup similar to [7], where the optical modulation is transferred to the RF domain and demodulated using an IQ receiver. The drive levels indicated are assumed for 50Ω loads. Figure 2(b) shows the frequency discriminating error signal and absorption as the ML is swept across the absorption line. The long-term ML frequency stability is characterized by generating a beat note between the ML and a stable bench-top external cavity laser. A frequency counter measures the beat frequency over a 10-minute period for 1-second gate times. As illustrated in Fig. 2(c), the peak-to-peak and standard deviation in the ML frequency stability improved twentyfold from 151 MHz and 30.2 MHz without feedback to 7.6 MHz and 1.54 MHz with feedback, respectively.

Since CO_2 has diurnal vertical transport, the absorption line is sampled at points offset from the center. This maintains uniform measurement sensitivity to concentrations in the lower troposphere. To accomplish this, a slave laser (SL) is offset phase locked to the stabilized ML using an optical phase locked loop (OPLL). A beat note between the two lasers is detected off chip and processed by the OPLL. The OPLL charge pump output is filtered and fed back to the SL phase section to maintain wavelength stability at offsets from the ML ranging from 1-15 GHz. The accuracy and precision of the SL offset to the stabilized ML is obtained by beating the two lasers and comparing the results with and without OPLL operation. The results are illustrated in Fig. 2(d) over 10 minutes for 1-second gate times for a 2 GHz SL OPLL offset setting. In this case the mean frequency offset was measured to be 2.000087 GHz with a standard deviation of 5.08 MHz. The accuracy and stability are degraded somewhat due to systematic sources of noise in the setup such as coupling from the PM driver to the ML. Figure 2(e) shows the spectra of a stabilized ML and overlapped locked SL waveforms ranging in offset from 1-15 GHz.

Finally, an on-chip semiconductor optical amplifier (SOA) is used to generate amplified SL 1 µs pulses at a 133 µs period to eliminate crosstalk from cloud scattering. Figure 2(f) shows the SL pulses generated using the on-chip SOA pulse carver. The pulses are driven using a pulsed current source and detected with a photodiode (PD) and transimpedance amplifier (TIA). The pulse is then viewed on an oscilloscope, which shows rise and fall times of 262 ns and 169 ns, respectively. Because the pulse extinction is below the PD noise floor, we estimate the extinction ratio at DC using a power meter and obtain more than 40 dB extinction between the on and off states at 100 mA and 10 mA, respectively. Such a high extinction ratio is critical to avoid power robbing from a booster EDFA before transmission to free space. The SL peak power, directly coupled from the PIC with a lensed fiber, exceeds 3 dBm.

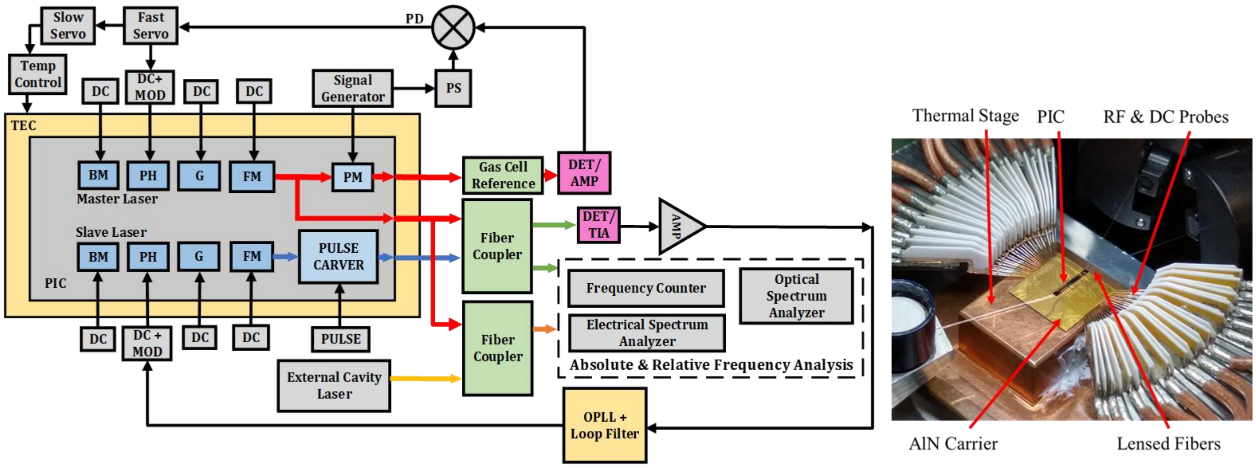

Fig. 1. PIC subsystem characterization test setup and photograph of PIC on carrier under test.

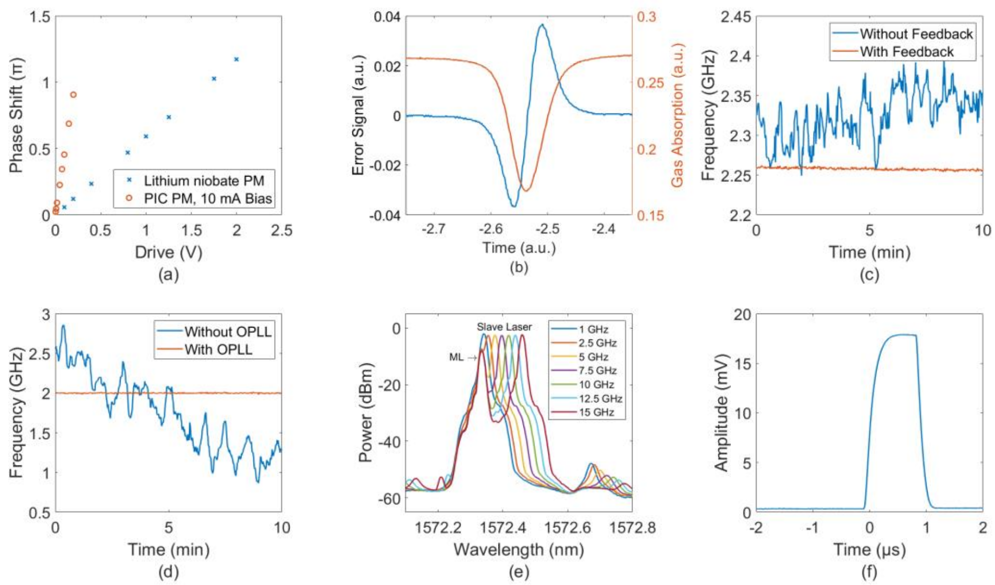

Fig. 2. (a) PM efficiency for 10 mA bias; (b) error signal and gas absorption; (c) ML stability for 1-second gate times; (d) SL stability, 2 GHz offset from ML; (e) ML/SL overlapped spectra at 1-15 GHz offsets; (f) SL amplified 1 μs pulse.

4. Conclusions

We designed and fabricated an IPDA remote sensing lidar monolithic InP PIC with two SGDBR lasers, a PM, and pulse carver. We illustrated efficient device operation and subsystem performance of the PIC. The results show a stabilized ML and SL offset locked up to 15 GHz. This demonstration illustrates the feasibility to realize compact lidar instruments for space platforms. Gas sensing measurements will be carried out in future work.

5. References

[1] J.B Abshire, *et al*., Tellus B 62, 770-783 (2010).
[2] H. Zhao et al., in IEEE Journal of Selected Topics in Quantum Electronics, vol. 25, no. 6, pp. 1-10, Nov.-Dec. 2019.
[3] K. Numata, et al., Opt. Express 20, 14234-14243 (2012).
[4] J. Fridlander, et al., in Conference on Lasers and Electro-Optics, OSA Technical Digest, paper SF3O.3.
[5] V. Rosborough, et al., presented at the Integrated Photonics Research Conf., IM2A.5, (2019).
[6] G.C Bjorklund, Opt. Lett. 5, 15-17 (1980).
[7] B. Arar, Appl. Opt. 56, 1246-1252 (2017).

Residual Amplitude Modulation Reduction in Integrated Indium Phosphide Phase Modulators

Victoria Rosborough[1*], Joseph Fridlander[1], Fengqiao Sang[1], Fabrizio Gambini[1], Simone Tommaso Šuran Brunelli[1], Jeffrey R. Chen[2], Stephan Kawa[2], Kenji Numata[2], Mark Stephen[2], Larry Coldren[1], Jonathan Klamkin[1]

[1]*Electrical and Computer Engineering Department, University of California Santa Barbara, Santa Barbara, CA 93106 USA*
[2]*NASA Goddard Space Flight Center, Greenbelt, MD 20771 USA*
**rosborough@ucsb.edu*

Abstract: A novel indium phosphide Mach-Zehnder interferometer with directional couplers was realized to compensate residual amplitude modulation in integrated phase modulators. The change in transmission for π phase shift was reduced from 3.85 dB to 1.98 dB.

OCIS codes: (130.3120) Integrated optics devices; (130.4110) Modulators

1. Introduction

Low residual amplitude modulation (RAM) phase modulators (PMs) are important for a host of applications, including precision spectroscopy, LIDAR, and quantum communications [1,2]. These applications would also benefit from reduced instrument size, weight, power consumption, and cost. Indium phosphide (InP)-based photonic integrated circuits (PICs) combine lasers, modulators, photodetectors, and passive components such as directional couplers on a single chip, greatly reducing footprint and improving reliability [3,4]. Typical InP PMs, however, suffer from bias-dependent high RAM, thereby motivating novel phase modulator implementations and/or RAM reduction for InP PICs [5].

In this work, we present an adaptation of the shift-and-dump phase shifter (SDPS) that was first demonstrated in silicon [6,7] to InP phase modulators for RAM reduction. The SDPS is a Mach-Zehnder interferometer-based device with directional couplers at the input and output (see top of Fig. 2(a)). By choosing the correct PM length and directional coupler splitting ratios, the device yields an almost constant total loss despite varying loss in the modulated arm as the phase changes. The ideal condition for the SDPS, as given in [6] is:

$$E_{out}\left(\varphi_1 + {}^{j\alpha_1}/_{2}\right) = E_{out}(0)e^{j\varphi_1} \tag{1}$$

With the device configuration shown at the top of Fig. 2(a), eqn. 1 becomes:

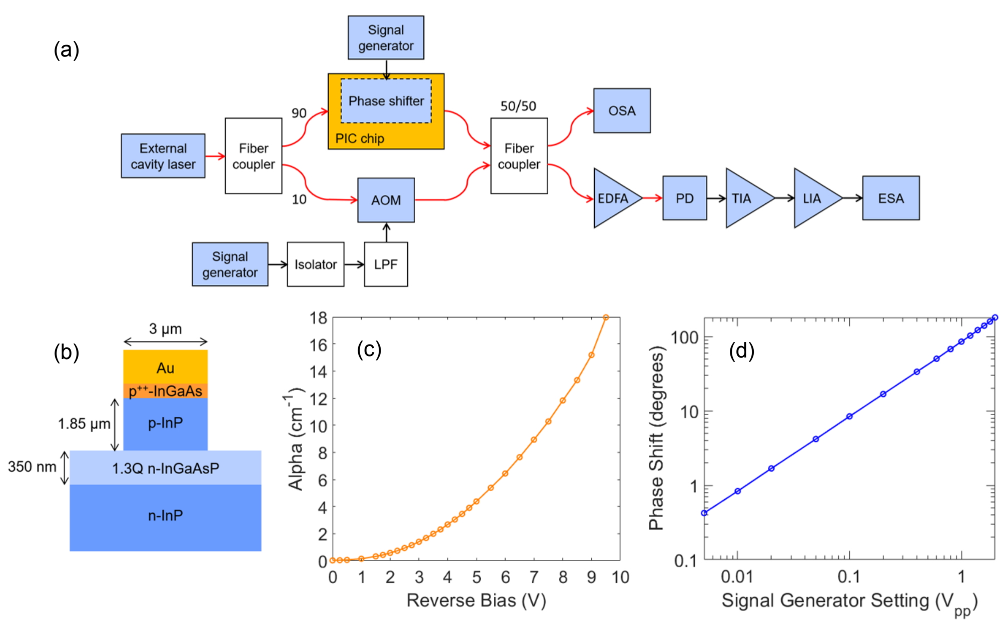

Figure 1. (a) Test setup used to measure straight PM efficiency. LPF = low pass filter, AOM = acousto-optic modulator, OSA = optical spectrum analyzer, EDFA = erbium-doped fiber amplifier, PD = photodiode, TIA = transimpedance amplifier, LIA = lock-in amplifier, ESA = electrical spectrum analyzer. (b) Cross-section of PM. (c) Waveguide loss as a function of reverse bias. (d) Straight PM efficiency.

$$e^{j\varphi_1}\sqrt{(1-\kappa_1)(1-\kappa_2)}\left(1-e^{-\alpha_1 L/2}\right)+e^{\left(j\varphi_2-\alpha_2 L/2\right)}\sqrt{\kappa_1\kappa_2}\left(1-e^{j\varphi_1}\right)=0 \quad (2)$$

where φ_1 and α_1 are the maximum phase shift and corresponding loss on the modulated arm and φ_2 is a constant bias applied to the top arm with accompanying loss α_2.

2. Straight Phase Modulator Characterization

To determine optimal values for the directional coupler splitting ratios, κ_1 and κ_2, and the SDPS arm length, L, the waveguide PM loss as a function of reverse bias and modulation efficiency must be determined. A cross-section of the PM waveguide is shown in Fig. 1(b). Phase change is accomplished by the Franz-Keldysh effect in the bulk indium gallium arsenide phosphide (InGaAsP) waveguide layer. To measure the loss as a function of reverse bias, a test structure with an integrated laser followed by a 2.5-mm long PM was used. With the laser on, the photocurrent at the PM was recorded for increasing reverse bias and converted to the loss values shown in Fig. 1(c). The method described in [8] was used to measure the modulation efficiency and the test setup is shown in Fig. 1(a). Figure 1(d) plots the linear component of the Fourier spectrum of the phase modulation and yields a modulation efficiency of approximately 30°/(V·mm). The PM was modulated at 500 kHz around a bias point of -1.5 V.

3. SDPS Design, Fabrication, and Characterization

An optical micrograph of the fabricated SDPS is shown at the bottom of Fig. 2(a). Based on the results from characterizing the straight PM it was determined that $\kappa_1 = \kappa_2 = 0.15$ for an arm length of 816 µm. The splitting ratio of the fabricated directional couplers was measured to be $\kappa = 0.12$. The black line in Fig. 2(b) shows the measured change in transmission through the SDPS as a function of reverse bias up to V_π. The total change in transmission level over π phase shift is 1.98 dB, whereas the expected change in transmission for the equivalent length straight PM, shown in blue, is 3.85 dB, representing almost a 50% decrease. The orange line is the calculated transmission for an SDPS with $\kappa_1 = \kappa_2 = 0.12$ and shows a transmission change of 1.41 dB, demonstrating that our device came close to the achievable transmission flattening.

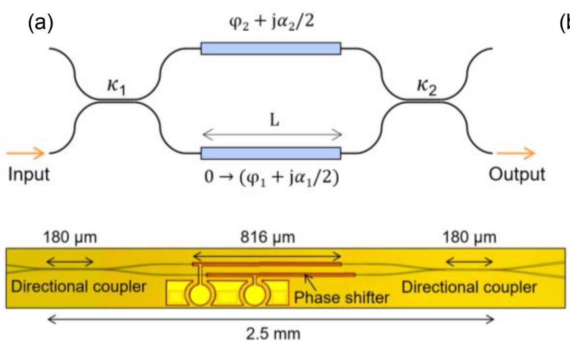

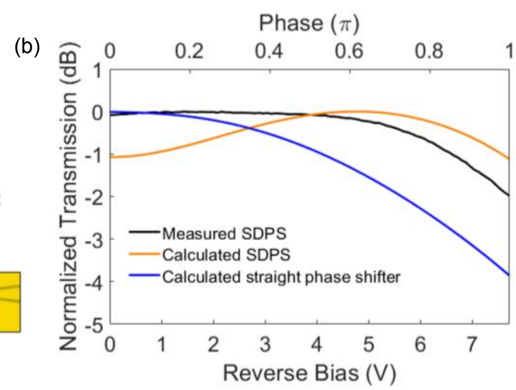

Figure 2. (a) Top: SDPS structure adapted from [6] Bottom: fabricated SDPS. (b) Measured change in transmission with reverse bias for SDPS (black) and expected change in transmission for the SDPS (orange) and straight PM of equivalent length (blue).

4. Conclusion

The device presented in this work reduces RAM in InP PMs by compensating for loss due to electro-absorption. The change in transmission for π phase shift was reduced from 3.85 dB to 1.98 dB for an 816-µm long PM. This implementation represents progress towards integrated laser stabilization for compact remote LIDAR sensors for small form factor satellites.

5. Acknowledgements

The authors acknowledge NASA for support through the ROSES Advanced Component Technology program. A portion of this work was performed in the UCSB Nanofabrication Facility.

6. References

[1] K. Numata, et al., "Frequency stabilization of distributed-feedback laser diodes at 1572 nm for lidar measurements of atmospheric carbon dioxide," *Applied Optics*, **50** (7) 1047—1056 (2011).
[2] P. Sibson, et al., "Integrated silicon photonics for high speed quantum key distribution," *Optica*, **4** (2) 172—177 (2017).
[3] J. Fridlander, et al., "Photonic integrated circuits for precision spectroscopy," presented at CLEO conf., SF30.3, (2020).
[4] V. Rosborough, et al., "Monolithic integration of widely-tunable DBR and DFB lasers with one-step grating formation," presented at OSA Advanced Photonics Congress IPR, IM2A.5, (2019).
[5] S. Andreou, et al., "Steady state analysis of the effects of residual amplitude modulation of InP-based integrated phase modulators in Pound-Drever-Hall frequency stabilization," *IEEE Photonics Journal*, **11** (3) (2019).
[6] N. Dupuis, et al., "Nanosecond-scale shift-and-dump Mach-Zehnder switch," *Optics Letters*, **44** (18) 4614—4616 (2019).
[7] Dupuis et al., "Electro-optic phase modulator with no residual amplitude modulation," US Patent 9912413B1 (2018).
[8] B. Arar, et al., "Method for in-depth characterization of electro-optic phase modulators," *Applied Optics*, **56** (4) 1246—1252 (2017).

INTEGRATED PHOTONICS TECHNOLOGY FOR EARTH SCIENCE REMOTE-SENSING LIDAR

Fengqiao Sang[1], Joseph Fridlander[1], Victoria Rosborough[1], Simone Tommaso Šuran Brunelli[1], Jeffrey Chen[2], Kenji Numata[2], Randy Kawa[2], Mark Stephen[2], Larry Coldren[1], Jonathan Klamkin[1]

[1]Electrical and Computer Engineering Department, University of California, Santa Barbara, CA, USA
[2]NASA Goddard Space Flight Center, Greenbelt MD, USA

ABSTRACT

We present recent progress on a photonic integrated lidar system for carbon dioxide (CO_2) active remote sensing at 1572.335 nm. With integration, the cost, size, weight and power (CSWaP) of the system are significantly improved. System and subsystem level results are demonstrated.

***Index Terms*—** Photonic integrated circuits, remote-sensing, lidar sensing

1. INTRODUCTION

Photonic integrated circuits (PICs) have been developed during the past few decades. With the growth of the data center and communication industries, integrated photonic technology has developed and matured rapidly in recent years. This gives us the opportunity to leverage PIC technology for remote science systems.

NASA Goddard Space Flight Center (GSFC) has spent several years developing a CO_2 remote sensing system based on laser absorption spectroscopy and the University of California, Santa Barbara (UCSB) is a leader in PIC technology [1-4]. We are collaborating to develop a PIC based CO_2 active lidar sensor based on NASA's current bench-top system [5,6]. The new system is designed and fabricated using an indium phosphide (InP) platform. One of the fabricated PICs, shown in Figure 1, has dimensions of 8300 μm by 700 μm. Integration significantly improved the cost, size, weight and power (CSWaP) of the lidar, which makes it ideal for implementation on small platforms, including CubeSats, drones, and space balloons.

In this work, we present the latest progress on this platform, including successful demonstration of laser wavelength stabilization and locking to the CO_2 line of interest, and the optical phase lock between the master and slave lasers, and the sampling of the CO_2 absorption line.

2. PIC PLATFORMS

There are many semiconductor material platforms useful for developing PIC technology. A popular one is silicon photonics (SiPh), which is currently growing quickly in both industry and academia. The SiPh platform uses silicon as its optical medium. It has the advantage of using complementary metal oxide semiconductor (CMOS) technology. CMOS reduces fabrication process development cost significantly and achieves sub-micron (down to tens of nanometers) resolution, also enabling monolithic integration of PICs and electronics integrated circuits. This makes it an ideal platform for data communication, where high speed electric and photonic communication interfaces are required. But the SiPh platform has a major disadvantage – silicon has an indirect bandgap and so is hard to be used to fabricate light sources, such as lasers [7]. Many researchers are trying to overcome this challenge via growth or bonding of direct bandgap materials on silicon, and though much progress has been made, but light sources of quality comparable to direct bandgap, group III-V materials, such as InP and GaAs, InGaAs and GaN, have not yet been achieved [8,9].

Another popular PIC platform is InP because it has the advantage that it can be used to make high-quality lasers, and high-speed modulators and photodiodes. The InP

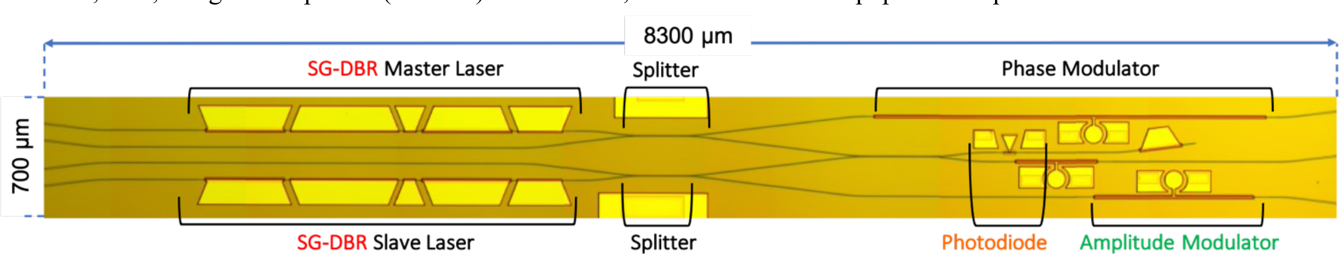

Figure 1: Microscope image of fabricated PIC.

IGARSS 2021 - 2021 IEEE International Geoscience and Remote Sensing Symposium | 978-1-6654-0369-6/21/$31.00 ©2021 IEEE | DOI: 10.1109/IGARSS47720.2021.9553656

platform has matured over the past decades and is widely used today for manufacturing lasers and modulators in the near infrared (NIR) region. Therefore, the groundwork has been laid to monolithically integrate all the necessary components together into a PIC. Compared to the SiPh platform, there are not that many InP multi-project wafer (MPW) services available for researchers and commercial use. Most InP foundries are only accessible for a company's internal use. Therefore, many researchers and companies choose to use academic nanofabrication facilities, such as the nanofabrication facility at UCSB. Those facilities do not provide a process design kit (PDK) for components, but do provide standard recipes for general-use tools. Under such circumstances, users get another degree of freedom when designing and optimizing their devices, but they also take the risk of not having a proven process with predictable performance.

3. ARCHITECTURE AND PIC DESIGN

The PIC was designed and fabricated based on an InP platform, using the two-laser architecture as shown in Figure 2. The first laser, the master laser, is locked to an external CO_2 reference cell, and the second laser, the slave laser, is locked to the master laser through an optical phase lock loop (OPLL).

The blue region in Figure 2 represents the monolithically integrated components, which include two lasers, a semiconductor optical amplifier (SOA), a photodiode (PD), a phase modulator (PM), and passive splitters. Figure 1 shows one of the PICs that was designed and fabricated and later used for system level testing. On this PIC, both the master and slave lasers are sampled-grating distributed Bragg reflector (SG-DBR) lasers, which provide over 40 dB side mode suppression ratio (SMSR), and a 38 nm wavelength tuning range from 1566 nm to 1604 nm. Power splitting in the PIC was achieved with directional couplers instead of multi-mode interferometers (MMIs) to minimize reflections back into the laser. The phase modulator modulates the master laser output with a 125 MHz phase signal. The modulated master laser output passes through the CO_2 cell and an error signal is detected using coherent phase detection. The detected error signal is fed back to the master laser to stabilize the master laser to the CO_2 absorption line. The integrated photodiode detects the beat note signal between the master and slave lasers. The beat note signal goes to the OPLL electronics that are used to offset lock the slave laser to the master laser. The slave laser is stepped in frequency to map the CO_2 absorption line in the gas being sampled. The SOA after the slave laser is used as an amplitude modulator to generate a pulsed signal by modulating the SOA from zero bias where it acts as an optical absorber to forward bias where it acts as an optical amplifier.

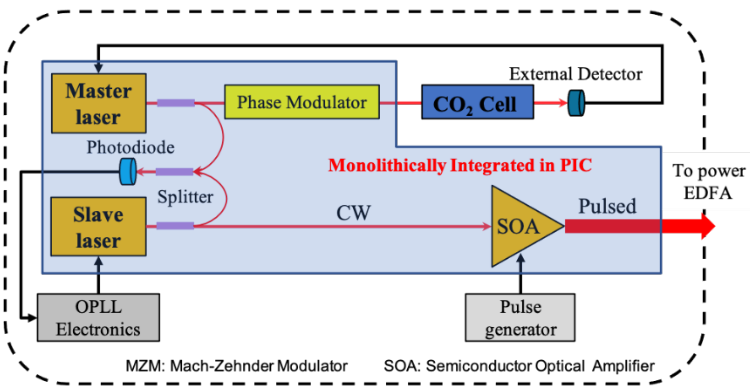

Figure 2: System architecture.

4. TEST AND RESULT

We mounted the PIC shown in Figure 1 on a carrier for system level testing, as shown in Figure 3. In the setup, two lensed fibers were used to externally couple the output light. An additional lensed fiber couples light from the back of the laser to monitor the output. The PIC was mounted in the center of the carrier and the device contacts were wire-bonded to the corresponding carrier pads to reroute the signal to RF & DC probes.

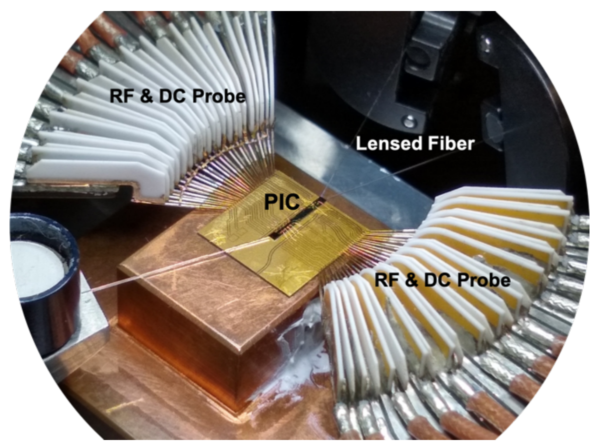

Figure 3: Camera image of PIC test setup.

In this setup, we successfully stabilized the master laser to the CO_2 absorption peak at 1572.335 nm by modulating the on-chip phase modulator at 125 MHz with a modulation depth of π and feeding the error signal back into to the phase section of the laser. The comparison is shown in Figure 4(a). Without the feedback enabled, the peak-to-peak and standard deviation of the frequency drift over 10 minutes was 151 MHz and 30.2 MHz respectively. With the feedback enabled the peak-to-peak and standard deviation of the frequency drift over 10 minutes was reduced to 7.6 MHz and 1.54 MHz, an improvement of over 20 times.

In addition, the slave laser was successfully locked to the master laser. In Figure 4(b-c), the slave laser was locked to the master laser with offsets from 1 GHz to 15 GHz, and stabilization data was recorded and compared at a 2 GHz frequency offset. The results showed that with OPLL disabled and enabled, the peak-to-peak and standard

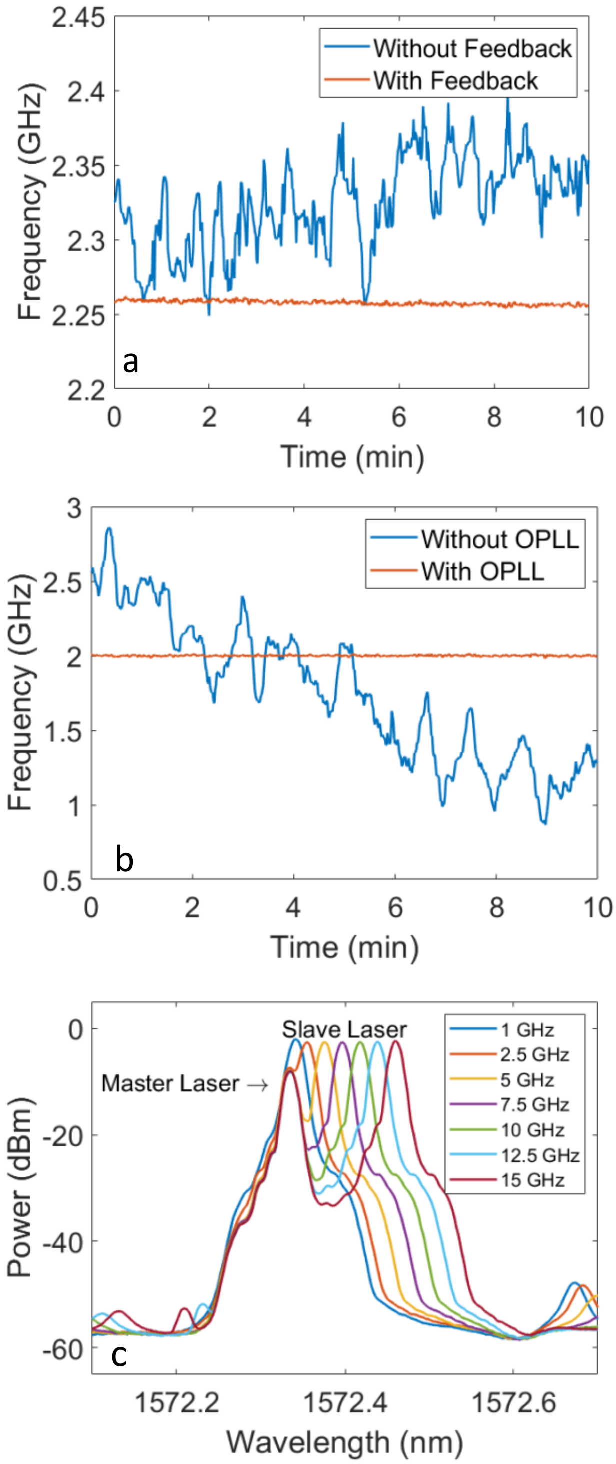

Figure 4: (a) Master laser wavelength stabilization. (b) Slave laser to master laser phase lock with 2 GHz offset. (c) Laser spectra with slave laser offset locked to master laser at 1 -15 GHz.

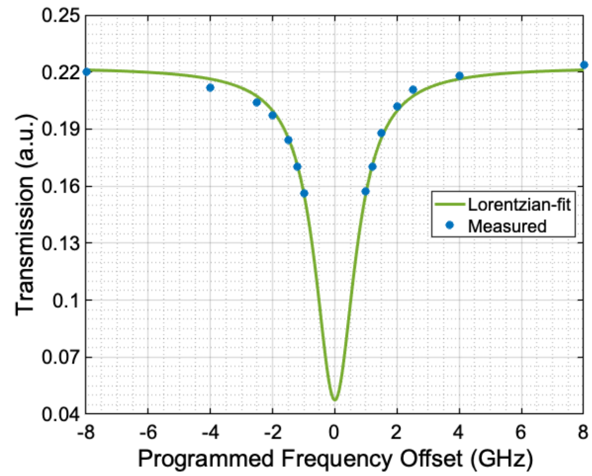

Figure 5: Measured absorption of the CO_2 test cell.

deviation of the frequency drift improved from 1.99 GHz and 478 MHz to 30.26 MHz and 5.07 MHz respectively with 1 second gate times for 10 minutes measurement.

Finally, we demonstrated the sampling of the CO_2 absorption line around 1572.335 nm using a CO_2 test cell with a different pressure than the CO_2 reference cell. As illustrated in Figure 5, 14 wavelengths around 1572.335 nm were sampled. Each point is an average of 1000 measurements taken over 100 µs. The CO_2 absorption line was recoverable based on a Lorentzian fit of the sampled data points.

4. CONCLUSION

We designed and fabricated InP based PICs for a CO_2 remote active sensing application. We demonstrated efficient device operation and subsystem performance of the PIC, and also successfully demonstrated sampling of the CO_2 absorption line at 1572.335 nm. This work showed and proved the possibility of implementing PIC technology for remote active sensing applications, especially for small platforms, such as CubeSats and drones.

5. REFERENCES

[1] Klamkin, J., Zhao, H., Song, B., Liu, Y., Isaac, B., Pinna, S., ... & Coldren, L. (2018, October). Indium phosphide photonic integrated circuits: Technology and applications. In 2018 IEEE BiCMOS and Compound Semiconductor Integrated Circuits and Technology Symposium (BCICTS) (pp. 8-13). IEEE.

[2] Zhao, H., Pinna, S., Sang, F., Song, B., Brunelli, S. T. Š., Coldren, L. A., & Klamkin, J. (2019). High-power indium phosphide photonic integrated circuits. IEEE Journal of Selected Topics in Quantum Electronics, 25(6), 1-10.

[3] Stephen, M., Klamkin, J., Coldren, L., Fridlander, J., Rosborough, V., Sang, F., ... & Kawa, R. (2019, July). Integrated Micro-Photonics for Remote Earth Science Sensing (Impress) Lidar. In IGARSS 2019-2019 IEEE International Geoscience and Remote Sensing Symposium (pp. 4853-4856). IEEE.

[4] Fridlander, J., Rosborough, V., Sang, F., Nickerson, M., Chen, J., Numata, K., ... & Klamkin, J. (2020, May). Photonic Integrated Circuits for Precision Spectroscopy. In CLEO: Science and Innovations (pp. SF3O-3). Optical Society of America.

[5] Numata, K., Chen, J. R., & Wu, S. T. (2012). Precision and fast wavelength tuning of a dynamically phase-locked widely-tunable laser. Optics express, 20(13), 14234-14243.

[6] Numata, K., Chen, J. R., Wu, S. T., Abshire, J. B., & Krainak, M. A. (2011). Frequency stabilization of distributed-feedback laser diodes at 1572 nm for lidar measurements of atmospheric carbon dioxide. Applied optics, 50(7), 1047-1056.

[7] Canham, L. (2000). Gaining light from silicon. Nature, 408 (6811), 411-412.

[8] Liang, D., & Bowers, J. E. (2010). Recent progress in lasers on silicon. Nature photonics, 4(8), 511-517.

[9] Sysak, M. N., Liang, D., Jones, R., Kurczveil, G., Piels, M., Fiorentino, M., ... & Bowers, J. E. (2011). Hybrid silicon laser technology: A thermal perspective. IEEE Journal of Selected Topics in Quantum Electronics, 17(6), 1490-1498.

ACKNOWLEDGMENTS

The authors acknowledge funding from NASA's Earth Science Technology Office (ESTO) Advanced Component Technology (ACT) program. A portion of this work was performed in the UCSB Nanofabrication Facility.

OSA Optical Sensors and Sensing Congress 2021 (AIS, FTS, HISE, SENSORS, ES) © OSA 2021

Photonic Integration for Low Size, Weight, and Power (SWaP) Remote Gas Spectroscopy

Victoria Rosborough[1*], Joseph Fridlander[1], Fengqiao Sang[1], Fabrizio Gambini[2,3], Simone Tommaso Šuran Brunelli[1], Jeffrey R. Chen[4], Stephan Kawa[4], Kenji Numata[4], Mark Stephen[4], Larry Coldren[1], Jonathan Klamkin[1]

[1]*Electrical and Computer Engineering Department, University of California Santa Barbara, Santa Barbara, CA 93106 USA*
[2]*University of Maryland Baltimore County, Baltimore, MD 21250 USA*
[3]*NASA Goddard Space Flight Center / CRESST II, Greenbelt, MD 20771 USA*
[4]*NASA Goddard Space Flight Center, Greenbelt, MD 20771 USA*
**rosborough@ucsb.edu*

Abstract: Subsystem operation of a photonic integrated circuit for low size, weight, and power remote gas sensing was demonstrated. Precision lidar system specifications for laser tuning, photodiode bandwidth and pulse extinction ratio were satisfied. A twentyfold improvement in long-term laser frequency stability was achieved. © 2021 The Author(s)
OCIS codes: (250.5300) Photonic integrated circuits; (280.3640) Lidar

1. Introduction

Active remote sensing of CO_2 would provide improved temporal and spatial resolution compared to the passive spectrometer measurement systems now in use [1]. A candidate integrated path differential absorption lidar system for NASA's Active Sensing of CO_2 Emissions over Nights, Days and Seasons (ASCENDS) mission was developed with commercial-off-the-shelf components at NASA Goddard Space Flight Center [2]. Using integrated photonics, an equivalent lidar system can be realized at a fraction of the size, weight, and power consumption (SWaP) [3]. A photonic integrated circuit (PIC) remote sensing module would not only be more compact and cost effective, but potentially more robust due to a decrease in the number of bulk optical connectors. In this work, we present an indium phosphide (InP) PIC for remote CO_2 sensing that translates the ASCENDS design for use in small form-factor platforms.

2. PIC Architecture and Fabrication

Figure 1 shows a photo of the fabricated PIC and illustrates the lidar operation. A master laser is stabilized to the 1572.335-nm absorption line center (ν_0) of CO_2 using a frequency modulation technique [4]. Part of the light from the master laser goes to an integrated phase modulator and is then coupled off-chip to a CO_2 reference cell. A beat note detected at the output of the CO_2 cell results in an error signal that provides feedback to the phase section of the master laser. A slave laser is offset-locked to the master laser via an optical phase locked loop (OPLL). The slave laser frequency is stepped through a discrete set of values to sample the atmospheric absorption line. After the slave laser steps to a new frequency, an amplitude modulator carves a high extinction ratio (>40 dB) pulse, which is coupled off-chip to an erbium doped fiber amplifier (EDFA). The 1-μs pulses are separated by 133 μs to eliminate crosstalk from cloud scattering [5].

An InP-based material system was chosen for the PIC because it is mature, exhibits a compatible wavelength range, and provides monolithic integration of both active and passive components. The PIC was fabricated at the UC Santa Barbara Nanofabrication Facility using an offset quantum well (OQW) epitaxial design that allows the gain material to be selectively etched away in the passive regions.

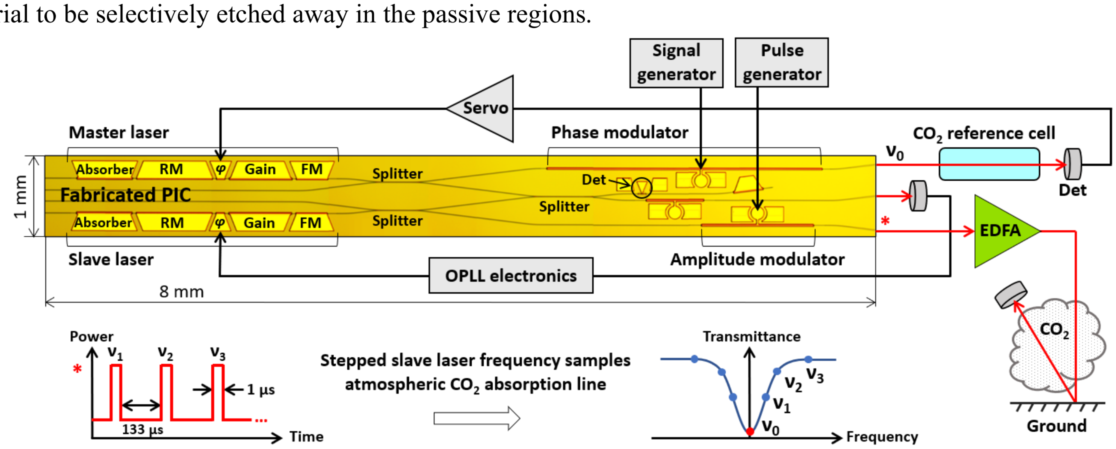

Figure 1. PIC and LIDAR system architecture for CO_2 monitoring. RM = rear mirror; FM = front mirror; φ = phase section; Det = detector.

3. Subsystem Characterization

We have demonstrated independent operation of each of the subsystems described above. Figure 2(a) shows the reference cell gas absorption overlaid with the error signal used to lock the master laser to the CO_2 absorption line. The error signal is proportional to the deviation from the line center. Fig. 2(b) plots the beat note used to characterize the master laser frequency stability. With feedback to the master laser, the peak-to-peak frequency deviations improved from 151 MHz to 7.6 MHz over 10 minutes for one-second gate times. The standard deviation in the frequency also experiences a twentyfold improvement from 30.2 MHz without feedback to 1.54 MHz with feedback. Figure 2(c) illustrates the slave laser frequency stability with and without the OPLL over 10 minutes for one-second gate times. For a programmed frequency offset of 2 GHz, the standard deviation in the slave laser frequency was 5.08 MHz and the average frequency offset from the master laser was 2.000087 GHz. Plotted in Fig. 2(d) is the frequency stepping of the slave laser from 1 to 15 GHz offset from the master laser frequency of 1572.335 nm. An integrated photodetector was included in the PIC (circled in Fig. 1) for on-chip detection of the beat note between the master and slave laser for the OPLL. Due to a fabrication defect, an off-chip detector was needed to demonstrate the slave laser locking. However, characterization of other integrated photodiodes did show the desired 15 GHz 3-dB bandwidth operation as shown in Fig. 2(e). Finally, a 1-μs pulse with an extinction ratio of at least 40 dB at the output of the amplitude modulator is shown in Fig. 2(f). The pulse extinction ratio was estimated using a DC measurement because the power level in the off state was below the photodiode noise floor.

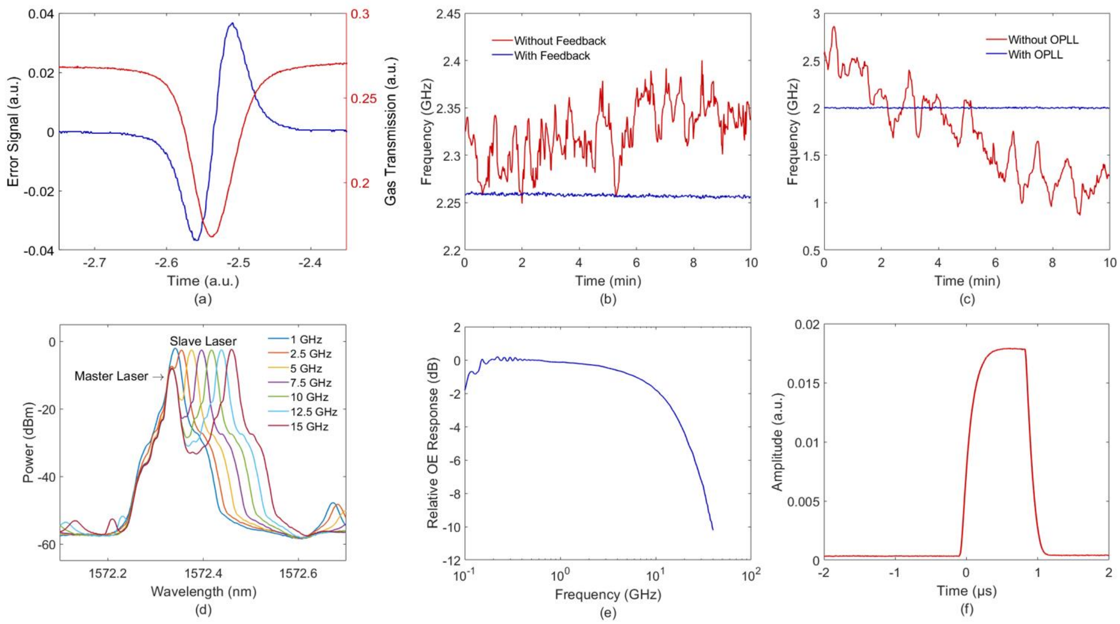

Figure 2. (a) error signal and gas absorption; (b) master laser frequency stability; (c) OPLL beat note for slave laser offset 2 GHz from master laser; (d) overlaid master and slave laser spectra for slave laser offsets of 1-15 GHz; (e) integrated photodiode response showing 15 GHz 3-dB bandwidth; (f) 1-μs pulse from amplitude modulator.

4. Conclusion

An InP PIC for low-SWaP CO_2 lidar was designed, fabricated, and evaluated for system level specifications. Integrated master and slave lasers were successfully stabilized for slave laser frequency offsets of up to 15 GHz. An integrated pulse carver achieved a 40-dB extinction ratio. Future work includes packaging with compact electronic control boards and demonstration of CO_2 sensing.

5. Acknowledgements

The authors acknowledge NASA for support through the ROSES Advanced Component Technology program. A portion of this work was performed in the UCSB Nanofabrication Facility.

6. References

[1] S. M. R. Crowell, et al., “On the ability of space-based passive and active remote sensing observations of CO2 to detect flux perturbations to the carbon cycle,” *J. Geophysical Research: Atmospheres*, **123**, 1460—1477, (2018).

[2] K. Numata, et al., “Precision and fast wavelength tuning of a dynamically phase-locked widely-tunable laser,” *Optics Express*, **20** (13) 14234—14243 (2012).

[3] J. Fridlander, et al., “Photonic integrated circuits for precision spectroscopy,” presented at CLEO conf., SF30.3, (2020).

[4] G.C. Bjorklund, *Optics Letters*, **5** (1) 15-17 (1980).

[5] K. Numata, et al., “Frequency stabilization of distributed-feedback laser diodes at 1572 nm for lidar measurements of atmospheric carbon dioxide,” *Applied Optics*, **50** (7) 1047—1056 (2011)

JOURNAL OF
Optical Communications
and Networking

INTREPID program: technology and architecture for next-generation, energy-efficient, hyper-scale data centers [Invited]

ADEL A. M. SALEH,[1,*] KATHARINE E. SCHMIDTKE,[2] ROBERT J. STONE,[2] JAMES F. BUCKWALTER,[1] LARRY A. COLDREN,[1] AND CLINT L. SCHOW[1]

[1]Department of Electrical and Computer Engineering, University of California, Santa Barbara, Santa Barbara, California 93106, USA
[2]Facebook, Menlo Park, California 94025, USA
*Corresponding author: AdelSaleh@ece.ucsb.edu

Received 14 July 2021; revised 30 September 2021; accepted 3 October 2021; published 29 October 2021 (Doc. ID 437858)

The INTREPID program is developing power-efficient coherent optics for package-level integration with future switch integrated circuits as a path to realizing higher-radix switches for flatter networks. The link architecture is underpinned by coherent quadrature phase-shift keying (QPSK) polarization-multiplex transceivers at 200 Gb/s per λ, further enhanced with wavelength division multiplexing (WDM) to enable energy-efficient 800 or 1600 Gb/s inter-switch fiber connections. The technology is compatible with conventional three-level data center designs as well as a two-level data center design introduced here, which includes an added layer of passive, arrayed waveguide grating routers (AWGRs) or WDM circuit switches to further improve the cost, energy efficiency, and latency of the network.

https://doi.org/10.1364/JOCN.437858

1. MOTIVATION

Data centers have become a key component of the world's information infrastructure and play an ever-increasing role in storing, processing, and routing the data that we rely upon in our personal and professional lives. Indeed, the number of Internet users is projected to exceed 5 billion within the next several years [1]. Data center traffic is now measured in 10's of zetabytes (10^{21}), with intra-data-center traffic making up >70% of the total and increasing at a >23% compound annual growth rate (CAGR) [2]. Consequently, in order to improve overall data center productivity and efficiency, a key focus must be placed on maximizing the bandwidth and efficiency of intra-data-center communications. Today these interconnects, which are generally accepted to be limited to distances under 2 km, are implemented as concatenations of electrical-optical-electrical (E-O-E) interconnections that suffer degraded efficiency due to requiring multiple 50 Ω high-speed electrical interfaces to switching application-specific integrated circuits (ASICs). The electrical input/output (I/O) cells in these switching chips must be designed for worst-case electrical channels and therefore can consume of the order of 50% of the total power for the switches.

The INTREPID project, part of the Advanced Research Projects Agency–Energy (ARPA-E) ENergy-efficient Light-wave Integrated Technology Enabling Networks that Enhance Dataprocessing (ENLITENED) program, was launched in 2017 as a collaboration between University of California, Santa Barbara (UCSB) and Facebook [3] and is still ongoing. The project focus is twofold: (1) developing a technology platform to integrate efficient high-speed photonic interfaces directly into chip packages and (2) exploring new network architectures that incorporate photonic routing and/or switching that are made possible by the expanded optical link budgets enabled by analog coherent link architectures. The efficiency targets of the co-packaged optical interfaces are aggressive, scaling to sub-pJ/bit for multimode (MM) vertical-cavity surface-emitting laser (VCSEL)-based short-reach server links and to less than 10 pJ/bit for single-mode (SM) analog coherent data-center-scale interconnects. Achieving these targets will enable highly integrated solutions for the 102 Tb/s switch generation, and beyond that can potentially offer substantial expansions in switch radix with simultaneous improvements in efficiency compared to aggressive projections of conventional module-based transceiver technology. Such large, highly efficient switches can enable flatter networks with higher bandwidth to improve the overall efficiency of data centers of all scales.

Our focus is on the integration of photonic I/O with electrical switch cores since the network switches are the points of highest bandwidth concentration and where efficient photonic I/O can have the greatest impact. Fat-tree networks, schematically depicted in Fig. 1(a), are the workhorse topology for data center networks due to their superior performance and scaling properties that fundamentally depend on switch radix,

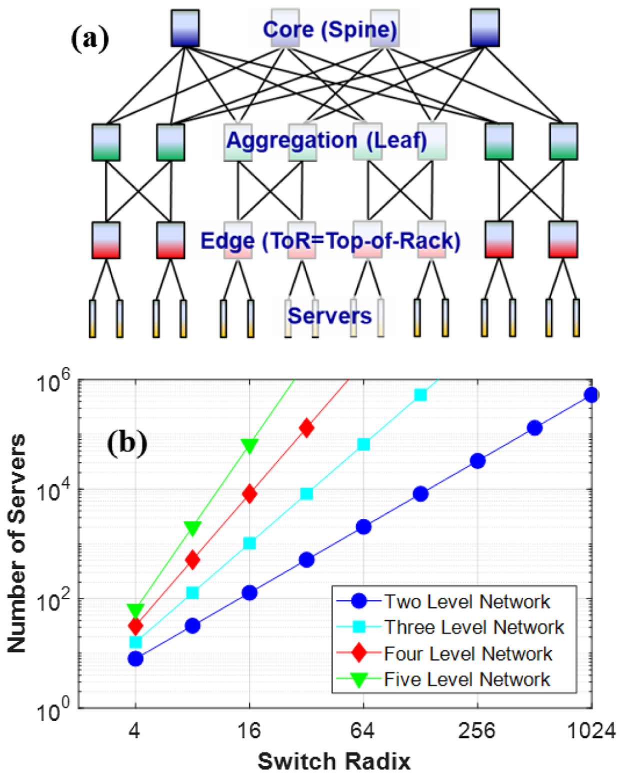

Fig. 1. (a) Illustration of a fat-tree network and (b) scaling properties: number of connected servers as a function of switch radix.

as shown in Fig. 1(b). The top of rack (ToR) switches require two types of interconnects: short distance (<3 m) for server connections and longer distance (<2 km) for connections to switches in the next level of the hierarchy. For the longer fabric links above the ToR, the use of a SM fiber is essentially a requirement due to its substantial advantages in operational management, cost, and support for bandwidth scaling through wavelength division multiplexing (WDM).

2. CO-PACKAGING FOR HIGHER RADIX SWITCHES

Our approach is conceptually illustrated in Fig. 2, representing what is often called "co-packaged optics (CPO)." Co-packaging has become a significant focus for the field over the last several years, and, an industry group led by Microsoft and Facebook, the CPO Collaboration, was recently launched with the goal of open development and broad commercial adoption of switch packages with integrated optical I/O [4]. By bringing all high-speed data on and off packages optically, instead of through conventional electrical interfaces that rely on ball grid array (BGA) or land grid array (LGA) connectors, the primary packaging bottleneck that limits the bandwidth and efficiency of today's systems is overcome. Integrating photonic interfaces into switch chip packages enables electrical connections at chip-scale pitch (e.g., C4 at ∼130 µm) instead of package-scale pitch (e.g., BGA/LGA at ∼1 mm). The electrical paths between the photonics and electronics are minimized, potentially enabling a >10× improvement in the efficiency of the ASIC to photonic I/O electrical links,

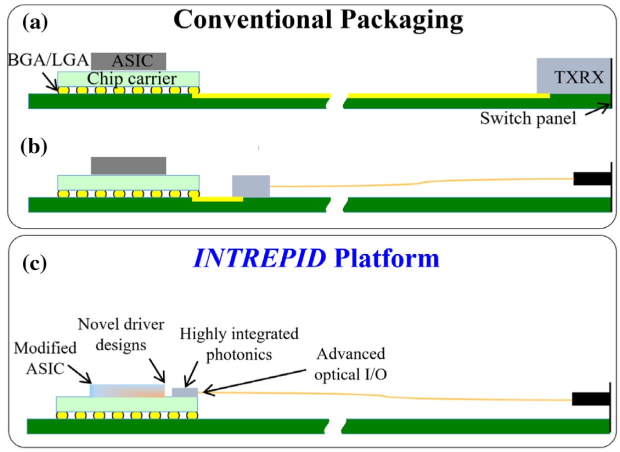

Fig. 2. Conceptual illustration of conventional optical module packaging in switches: (a) pluggable optics: pluggable transceiver (TXRX) modules, (b) on-board optical modules, and (c) optics in chip package: the integrated platform under development.

with a concurrent enhancement of bandwidth density of up to ∼60×. General trends of electrical chip I/O show a direct dependence on channel loss, with 30 dB of channel loss (a typical target for general purpose electrical I/O) degrading efficiency by 10−20× [5]. Conversely, the short interconnects within a chip package have low channel loss and therefore can be designed for maximum efficiency. A 2 cm electrical interconnect demonstrated an efficiency of 1.4 pJ/bit, >14× more efficient compared to typical general purpose I/O cells that consume ∼20 pJ/bit [6].

Figure 3 presents a conceptual view of the modular photonic integration platform we envision applied to a ToR switch, encompassing the co-design of interface circuitry to the digital switch core, the I/O bridge, electronic/photonic interposers, and SM and MM photonics with array fiber coupling.

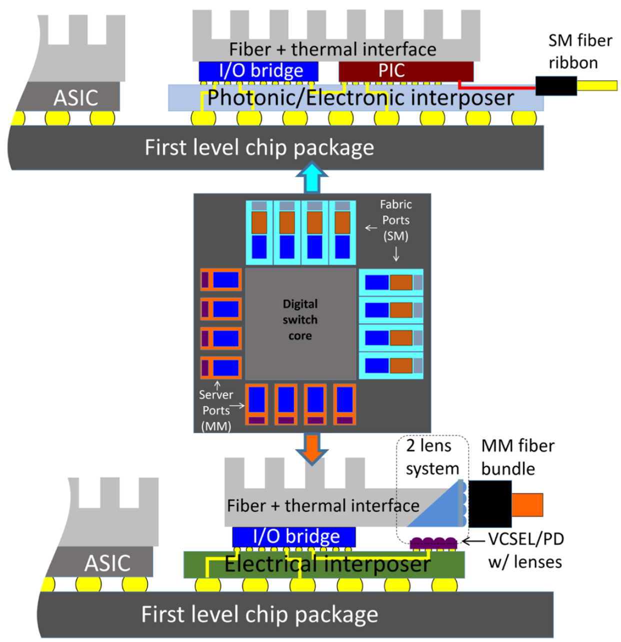

Fig. 3. Implementation concepts for integrating optics into first-level chip packages.

Switches for the higher levels of the network will integrate only SM photonics for the reasons discussed above.

3. ENERGY-EFFICIENT ANALOG COHERENT LINKS

For interconnects above the ToR/end of row (EoR) tier, we are developing low-cost, low-power coherent WDM photonic interconnects purpose-built for the longer fabric links required in the data center. Tailoring the transceiver to data center requirements requires optimization for a different set of metrics compared to current long-haul and metro coherent technology, specifically: (1) low-power consumption, (2) expanded link budgets, (3) low cost, and (4) low latency. Future scalability to higher data rates is possible through higher-order modulation formats, polarization modulation, and additional wavelengths. For data centers, the significantly larger link budget is a key advantage for coherent links, enabling reduced link power (lower required source laser power), lower cost (relaxed alignment tolerances/device specifications), and novel network architectures that incorporate all-optical routing/switching. Expansions of link budget of the order of 20 dB are possible [7], and our analysis shows that link budgets of 13 dB can be achieved with wall-plug link efficiencies better than 5 pJ/bit [8]. This level of tolerance to link loss allows for the incorporation of an arrayed waveguide grating router (AWGR) or active photonic switching layer without requiring complex and costly integrated optical gain in such components. Furthermore, the high selectivity offered by coherent reception significantly reduces the optical crosstalk requirements between channels for photonic routing/switching devices.

The INTREPID analog coherent links under development drastically reduce power and complexity compared to current digital coherent technology that relies heavily on digital signal processing (DSP) to compensate for chromatic dispersion (CD), polarization mode dispersion (PMD), and nonlinear effects in dense WDM (DWDM) links. The INTREPID links operate in the O-band near the zero-dispersion wavelength for standard SM fiber (1264–1338 nm), meaning CD and PMD will not have to be compensated, as they contribute negligible performance penalties for links up to 2 km. Furthermore, to eliminate the need for inefficient high-resolution analog to digital converters (ADCs) and DSP-based carrier recovery, we are developing optical phase locked loops (OPLLs) that lock and track the phase, frequency, and polarization of the receiver local oscillator (LO) to the incoming signal [9]. Highly integrated OPLLs have been demonstrated to enable robust and high-performance "analog coherent" receivers that operate with very low uncorrected bit error rate (BER, $<10-12$) and do not rely upon costly, high-power ADCs and DSPs [10,11]. The analog coherent receivers we are developing are optimized for power efficiency through photonic device and circuit co-design, choice of modulation format (quadrature phase-shift keying, QPSK), and close integration of electronics and photonics to minimize loop delays and maximize noise tolerance.

The baseline link architecture for the analog coherent links targets 200 Gbps/λ, achieved through QPSK modulation (2 bits per symbol) at 56 Gbd, with polarization multiplexing to achieve an additional factor of two in bandwidth per wavelength. Scaling to higher bandwidths is supported by adding additional wavelength channels, between 4 and 8, to provide solutions for 800G and 1.6T links. A block diagram of a 4λ analog coherent link is presented in Fig. 4. A comprehensive simulation framework has been developed to model and optimize the energy efficiency of the link architecture. The model includes all of the required components, including driver and receiver plus OPLL circuitry, source and LO lasers, polarization multiplexing and control structures, optical 90° hybrids, and high-speed photodetectors. Details of the simulation framework can be found in [8], and we project that the analog coherent links can support link budgets of 13 dB operating at an uncorrected BER of 10^{-12}, with a wall-plug energy efficiency of ~5 pJ/bit. Forward error correction (FEC), such as the common KR4-FEC (BER $< 2.1 \times 10^{-5}$), is widely used for data center links. The operating point of the analog coherent links can be tuned to achieve even better energy efficiency if FEC is utilized.

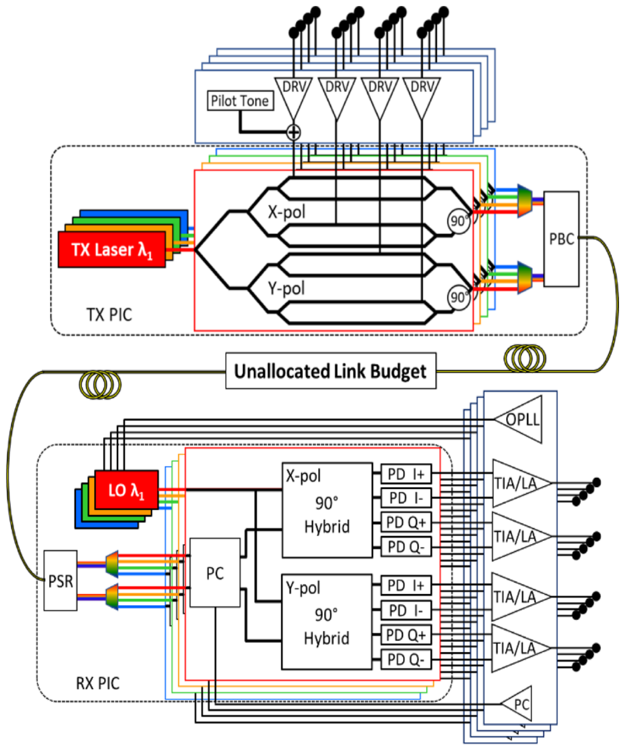

Fig. 4. High-level schematic of 4λ PM-QPSK analog coherent link architecture. DRV, modulator driver; LO, local oscillator; PBC, polarization beam combiner; TIA/LA, transimpedance amplifier/limiting amplifier; PSR, polarization splitter/rotator; PD I/PD Q, photodiode in/quadrature phase; PC, polarization controller; OPLL, optical phase locked loop controller.

First-generation functional prototypes of the key hardware components have been demonstrated, including InP and SiP coherent receiver photonic integrated circuits (PICs), high-speed drivers and receivers, and transmitter PICs [12,13]. Full coherent receivers consisting of PICs integrated with electrical amplifier integrated circuits (ICs) have been demonstrated to operate at 80 Gb/s [14] and 100 Gb/s [15], with the latter result exhibiting an efficiency of <1 pJ/bit. Other notable results include monolithically integrated optical receivers operating at 50 Gb/s [16,17], optical transmitters operating at 50 Gb/s [18], a novel architecture to implement feed-forward equalization in the optical or electrical domains [19], and a transimpedance amplifier achieving a record data rate of 108 Gb/s [20].

4. EFFICIENT VCSEL LINKS FOR SERVER CONNECTIONS

For server links, VCSEL technology provides a viable path to low-cost, short-distance links with sub-pJ/bit efficiency. VCSEL links have demonstrated the best wall-plug efficiency of any high-speed optical links [21] and have achieved data rates that were previously thought unattainable [22]. VCSEL links, implemented as active optical cables, are currently ubiquitous for 100G ToR-to-aggregation layer connections [23]. Due to their simplicity, efficiency, and low cost, VCSEL links have the potential to displace copper interconnections within the rack between servers and ToR switches. The VCSEL links we are developing can serve these <3 m applications and can also support migration from ToR to EoR switches (<30 m) if demanded by the evolution of data center architectures (see Section 5).

The majority of the efforts for hardware development in the INTREPID program are devoted to developing low-power coherent links, as these are a missing piece of technology that has not been demonstrated and that can make a significant impact on data center networks. VCSEL links, on the other hand, are continuing to be developed and advanced by multiple groups and companies, including another program funded under ARPA-E ENLITENED, MOTION, led by IBM [24]. The VCSEL links developed under INTREPID utilize proven equalization techniques [25] to realize single-pJ/bit full-link efficiencies at data rates of 50 Gb/s and above [13]. Novel implementations of transmitter equalizers have yielded low-power operation at high data rates, including a <3 pJ/bit VCSEL driver operating up to 52 Gb/s [26] and a full optical link operating up to 50 Gb/s at an efficiency of 9.5 pJ/bit [27].

5. DATA CENTER NETWORK ARCHITECTURE

A. Alternative Data Center Designs

As mentioned earlier, one of the primary goals of the INTREPID project is to utilize CPO to enable the use of large electronic packet switches to flatten the data center (i.e., to reduce the number of switching levels for a given number of servers). The largest switch size available to date has a throughput of 25.6 Tb/s [28], which is expected to double about every two years. Thus, we will target future switch sizes of 51.2 and 102.4 Tb/s. Furthermore, in our design examples, we will consider hyper-scale data centers supporting of the order of hundreds of thousands of servers, each of a bit rate of 50 or 100 Gb/s.

1. Conventional, Three-Level Data Center Design (Design Type 1)

One can achieve the above objectives using a traditional three-level folded-Clos (fat-tree) data center design, which

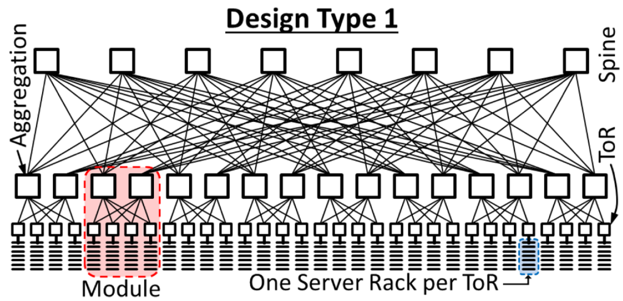

Fig. 5. Conventional, three-level, folded-Clos (fat-tree) data center utilizing large spine and aggregation switches of the same size and smaller ToR switches.

is depicted in Fig. 5. This design, which we will refer to as *Design Type 1*, employs large electronic switches in both the top switching level (spine) and the intermediate switching-level (aggregation) layers and smaller ToR switches in the bottom level. Each ToR switch supports one rack of servers, as indicated in the figure. The *module* shown in the figure, which is often called *server pod* in the literature, represents a grouping of switches and server racks that repeats across the data center and is connected to each of the spine switches.

Let T be the throughput of a spine or an aggregation switch, which will be referred to as the *large switch*, and let τ be the throughput of a ToR switch. Let R be the bit rate per inter-switch fiber link, which is assumed to employ SM fibers. The ToR switches are connected from below to servers via links of a bit rate of σ per server. The radix (i.e., the number of fiber ports) of a packaged large switch is $N = T/R$. Moreover, one can define the *effective* radix of a ToR switch as $M = \tau/R$.

Each spine switch has all of its N fiber ports (each at a bit rate of R) directed downward, and (assuming no *oversubscription*, which will be considered in Section 5.B) each aggregation switch has $N/2$ of its fiber ports directed upward and $N/2$ directed downward. Moreover, each ToR switch has $M/2$ fiber ports directed upward (each at a bit rate of R), and $(M/2) \times (R/\sigma)$ ports (each at a bit rate of σ) directed downward to the servers. (Note that the reason we call M the *effective* radix of a ToR switch is because this would have been the radix if all of its ports were of the same bit rate of R.)

It follows that Design Type 1 has N modules, each containing $N/2$ ToR switches, each supporting one rack of $(M/2) \times (R/\sigma)$ servers, for a total number of servers of $z_1 = (MN^2/4) \times (R/\sigma)$, which can also be written as $z_1 = \tau T^2/(4R^2\sigma)$.

Plots of the number of servers versus the bit rate, R, per inter-switch fiber link (or, equivalently, per integrated switch port) are given in Figs. 6 and 7 for various values of the ToR switch size, τ. The two figures, respectively, correspond to large switch sizes of $T = 51.2$ and 102.4 Tb/s and for server bit rates of $\sigma = 50$ and 100 Gb/s. In each figure, the scale at the top represents the radix, N, of the corresponding integrated switch. The three design points represented by the triangle, circle, and square in each of these figures will be used later for comparisons with other designs.

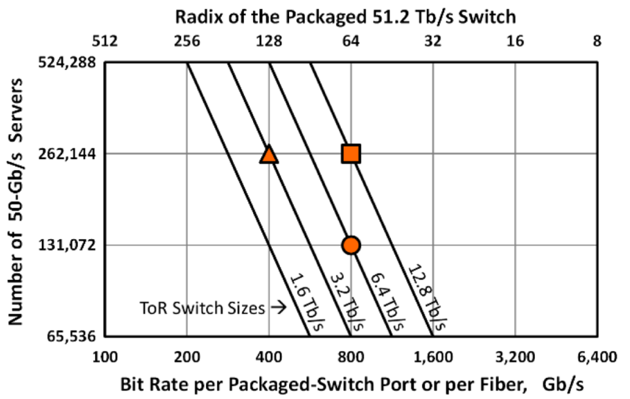

Fig. 6. Number of 50 Gb/s servers versus bit rate per inter-switch fiber link for data center Design Type 1 with a large switch size of 51.2 Tb/s for various ToR switch sizes.

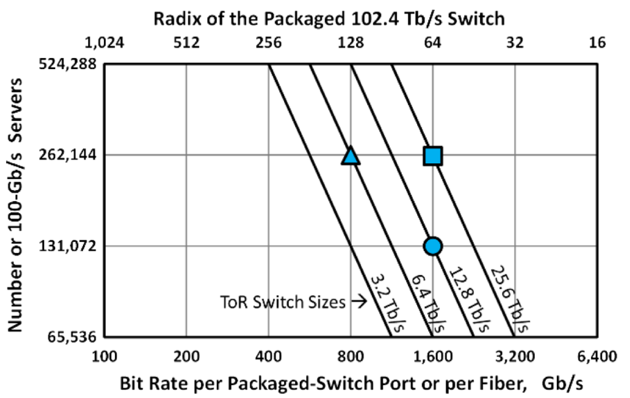

Fig. 7. Number of 100 Gb/s servers versus bit rate per inter-switch fiber link for data center Design Type 1 with a large switch size of 102.4 Tb/s for various ToR switch sizes.

2. *EoR-Based, Two-Level Data Center Design (Design Type 1.5)*

One can further flatten the data center by reducing the number of electronic switching levels from three to only two. To support the same number of servers, however, this requires both (1) using large switches for both the top and bottom switching layers and (2) reducing the bit rate of the inter-switch fiber links, thus increasing the switch radix. This design, which will be referred to as *Design Type 1.5*, is depicted in Fig. 8. As shown in the figure, the large bottom switches are called EoR switches. Because of its large size (compared to a ToR switch), each EoR switch supports a row of multiple racks of servers, not just one. Note that a module in Design Type 1.5 consists of only one EoR switch and its associated multiple server racks.

Let the throughput of each of the spine and EoR switches be T (which is the same as the throughput of the large switches in Design Type 1), and let σ be the bit rate per server. Furthermore, let R' be the bit rate of the inter-switch fiber links, and let $N' = T/R'$ be the corresponding radix of a spine switch, which is the same as the effective radix of an EoR switch. In general, $R' \ll R$ and $N' \gg N$, but this will be made more precise shortly.

Following the same analysis used in the above design, and assuming no oversubscription, one can show that

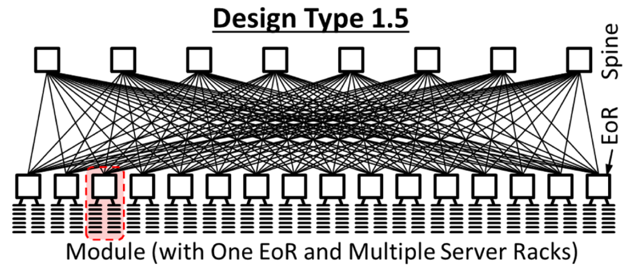

Fig. 8. Flat data center design with only two levels of large electronic switches of the same size.

Design Type 1.5 has N' EoR switches, each supporting $(N'/2) \times (R'/\sigma)$ servers (placed in multiple racks), for a total number of servers of $z_{1.5} = (N'^2/2) \times (R'/\sigma)$, which can also be written as $z_{1.5} = T^2/2R'\sigma$.

Using the above formulas and noting that $T = NR = N'R'$, one can show that Design Types 1 and 1.5 will have the same number of servers, i.e., $z_1 = z_{1.5}$, if $R' = R/(M/2)$ and, thus, $N' = N \times (M/2)$, where, as mentioned before, $M = \tau/R$ is the effective radix of a ToR switch in Design Type 1. One can get some numerical examples by considering the three design points of Design Type 1 represented by the shaded shapes in Figs. 6 and 7. The corresponding values of the effective ToR radixes are given by $M = 8$ for the circle and triangle design points and $M = 16$ for the square design point.

Thus, for Design Type 1.5 to have the same number of servers as Design Type 1, it follows that Design Type 1.5 requires $M/2 =$ four or eight times the number of fibers required in Design Type 1. This makes Design Type 1.5 not desirable from a practical point of view. On the other hand, because of its flat, two-level design, it has the advantage of lower cost, latency, and energy consumption because of the elimination of an electronic switching level and its associated transceivers.

3. *EoR/AWGR-Based, Two-Level Data Center Design (Design Type 2)*

We now introduce a novel data center design, which will be referred to as *Design Type 2*, that retains all the performance advantages of Design Type 1.5, while requiring the same number of interconnect fibers as in Design Type 1. The new design is compatible with the INTREPID transceiver technology of the inter-switch links. As mentioned in Section 3, this technology is based on the use of WDM and polarization-multiplexed, analog QPSK modulation with coherent reception (which results in $\mu = 4$ bits per symbol). Our current goal is to have $\nu = 4$ wavelengths per fiber with a modulation symbol rate of $\rho = 50$ GBaud. In this case, the bit rate per wavelength is $r = \mu\rho = 200$ Gb/s, and the bit rate per fiber is $R = \nu r = 800$ Gb/s. In the future, we plan to double R to 1600 Gb/s, without changing the modulation format, by either doubling ρ to 100 GBaud (which results in $r = 400$ Gb/s per wavelength) or doubling ν to eight wavelengths per fiber.

Besides being highly energy-efficient, this modulation/reception technique also yields a link budget of more than 10 dB [8]. This large link budget, combined with WDM, enables the realization of the novel data center architecture of

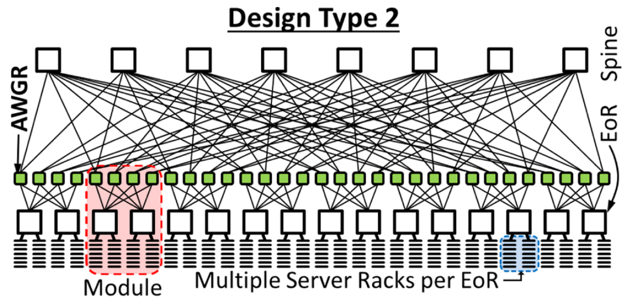

Fig. 9. Novel data center architecture utilizing two levels of large (spine and EoR) electronic switches of the same size, interconnected with WDM fibers, with an added layer of AWGRs (small, shaded boxes).

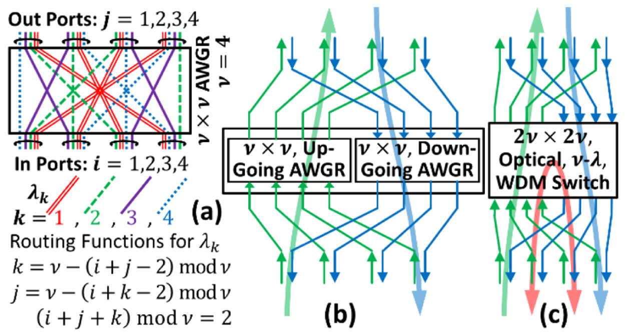

Fig. 10. (a) Routing pattern of a $\nu \times \nu$ AWGR. (b) Connecting a pair of AWGRs to handle the up- and down-going traffic. (c) A $2\nu \times 2\nu$ WDM circuit switch may replace each AWGR pair in the future to provide wavelength-level circuit switching flexibility (see Section 5.D.2).

Design Type 2, which is depicted in Fig. 9. As shown in the figure, this is a folded-Clos architecture with only two electronic switching levels (spine and EoR), with all switches having the same large size (as was the case in Design Type 1.5) and with a layer of passive, $\nu \times \nu$ AWGRs inserted in the fiber links between the two switching levels. (This architecture resembles that described in [29].) The bit rate per fiber in this design is the same as that used in Design Type 1. Moreover, the same WDM-based transceivers are employed here. The function of the AWGRs is to statically demultiplex, shuffle, then remultiplex the wavelengths in the various fibers such that the electronic switches in the two switching levels surrounding the AWGRs will be inter-connected in a folded-Clos pattern at a *single-wavelength* level. For example, for a fiber bit rate of $R = 800$ Gb/s, with $\nu = 4$ wavelengths per fiber, the bit rate of each connection becomes $r = R/\nu = 200$ Gb/s. In effect, this design has identical connectivity and, hence, also identical performance advantages as Design Type 1.5 (with $R' = r$), while having the same number of fibers as in Design Type 1. Also, as in Design Type 1.5, each EoR switch supports a row of multiple racks of servers, not just one.

Note that Design Type 2 does not require tunable transceivers.

Each shaded box in Fig. 9 actually consists of a pair of AWGRs, one for the up-going traffic and the other for the down-going traffic. Figure 10(a) shows the wavelength routing pattern of a typical AWGR, and Fig. 10(b) shows how a pair of AWGRs is to be connected to the up-going and down-going fibers.

Let T be the throughput of each of the spine and the EoR switches, R be the bit rate of the inter-switch fiber links, ν be the number of wavelengths per fiber, $r = R/\nu$ be the bit rate per wavelength, σ be the bit rate per server, and $N = T/R$ be the radix of a spine switch, which is the same as the *effective* radix of an EoR switch.

Each spine switch has all of its N fiber ports directed downward. Each AWGR has ν fiber ports directed upward and ν fiber ports directed downward. Moreover (assuming no oversubscription), each EoR switch has $N/2$ fiber ports directed upward and $(N/2) \times (R/\sigma)$ ports (each at a bit rate of σ) directed downward to the servers.

It follows that Design Type 2 has N modules, each containing ν EoR switches, each supporting $(N/2) \times (R/\sigma)$ servers (placed in multiple racks), for a total number of servers of $z_2 = \nu(N^2/2) \times (R/\sigma)$, which can also be written as $z_2 = T^2/2r\sigma$, which is independent of R or ν. For Design Types 1 and 2 to have the same number of servers, i.e., $z_1 = z_2$, one must have $\nu = M/2$, where M is the effective radix of a ToR switch in Design Type 1. This condition can also be written as $2\nu R = \tau$; i.e., the throughput of an AWGR pair in Design Type 2 is equal to the throughput of a ToR switch in Design Type 1.

Plots of the number of servers versus the bit rate, R, per inter-switch fiber link (or, equivalently, per integrated switch port) are given in Figs. 11 and 12 for various values of the number of wavelengths per fiber, ν. The two figures, respectively, correspond to switch sizes of $T = 51.2$ and 102.4 Tb/s and for server bit rates of $\sigma = 50$ and 100 Gb/s. In each figure, the scale on the right shows the bit rate per wavelength, r, and the top scale represents the radix, N, of the corresponding integrated switch. The three design points in each of these figures represented by the triangle, circle, and square give the same data center designs (in terms of the number of servers and the bit rate per fiber) as those given in Figs. 6 and 7, respectively, for Design Type 1. More specifically, in each of the four figures, the circle design point corresponds to ($N = 64$, $M = 8$, $\nu = 4$, and z = 131,072 servers), the triangle design point corresponds to ($N = 128$, $M = 8$, $\nu = 4$, and z = 262,144 servers), and the square design point corresponds to ($N = 64$, $M = 16$, $\nu = 8$, and z = 262,144 servers).

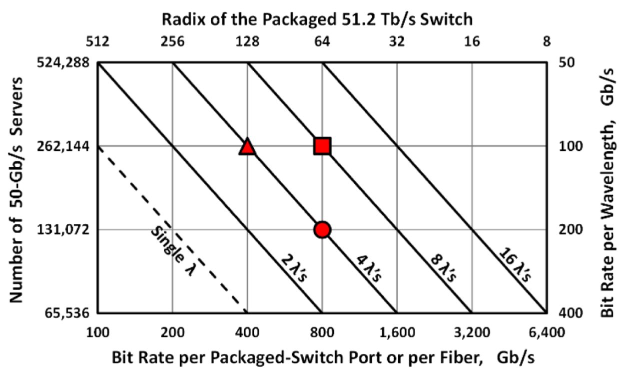

Fig. 11. Number of 50 Gb/s servers versus bit rate per inter-switch fiber link for Design Type 2 with a switch size of 51.2 Tb/s and for various values of the number of λ's per fiber.

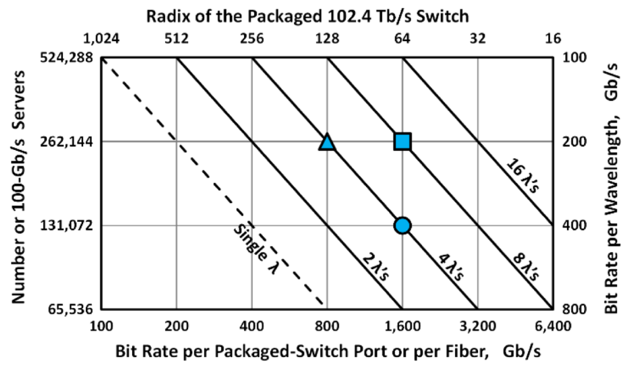

Fig. 12. Number of 100 Gb/s servers versus bit rate per inter-switch fiber link for Design Type 2 with a switch size of 102.4 Tb/s and for various values of the number of λ's per fiber.

Each of the dashed lines in Figs. 11 and 12 represents the case of a single-wavelength design, i.e., $\nu = 1$. Mathematically, this represents the limiting case of having Design Type 2 with a single wavelength and 1×1 AWGRs, which implies that there are no AWGRs. In this case, Design Type 2 reduces to Design Type 1.5 with $R' = r$ and $N' = T/r$.

B. Comparing the Traditional, Three-Level Data Center Design Type 1 and the EoR/AWGR-Based, Two-Level Data Center Design Type 2

1. Oversubscription Ratio

Before comparing the two designs, we will generalize the results for arbitrary values of the *oversubscription ratio*, which we will denote by Ω. This is defined for a given electronic switching layer as the ratio of the bandwidth below the layer to that above the layer. In general, $\Omega \geq 1$. As is often done in practice, we will assume that oversubscription occurs only in the bottom switching layer, i.e., the ToR switches in Design Type 1 and the EoR switches in Design Type 2. Designs with $\Omega = 1$, which have been considered so far, imply that the ports of each switch are arranged such that the bandwidth above and below the switch are equal. This has the advantage of eliminating packet blocking, thus improving the latency. On the other hand, designs with $\Omega > 1$ imply that the bandwidth above the switch is smaller than that below the switch. This can result in an appreciable decrease in the number of the switches required in the interconnect network, as well as a corresponding increase in the number of supported servers. However, it can lead to some packet blocking. The resulting latency penalty may not be a problem if the servers in the data center are not fully utilized. While this is generally not desirable, it is often the case in practice because of unpredictable workload variations.

2. Summary of Design Formulas

Table 1 summarizes the design formulas for data center Design Types 1 and 2 as a function of Ω. An implicit assumption in the table is that the bit rate per fiber, R, which is the same for Design Types 1 and 2, is generated by ν wavelengths, each of bit rate $r = R/\nu$, as would be the case when using the INTREPID WDM transceiver technology. (It should be noted that, in general, since Design Type 1 is based on using direct point-to-point fiber links between corresponding switch ports, any other modulation format, WDM or not, can be used as long as the total bit rate per fiber is R.)

Table 1. Design Formulas for Data Center Design Types 1 and 2

Design	Inter-Switch-Fiber Bit Rate	Electronic Switch Type (or AWGR)	Throughput	Radix[a] of Switch (or AWGR)	Number of Up Ports	Number of Down Ports[b]	Number of Switches (or AWGRs)	Total Number of Inter-Switch Transceivers	Total Number of Servers[c]
Design Type 1	R	Spine	T	$N = T/R$	0	N	$\frac{MN/2}{1+\Omega}$	$\frac{2MN^2}{1+\Omega}$	$(MN^2/2) \times \left(\frac{\Omega}{1+\Omega}\right) \times \left(\frac{R}{\sigma}\right)$
		Aggregation			$N/2$	$N/2$	$\frac{MN}{1+\Omega}$		
		ToR	τ	$M = \tau/R$	$\frac{M}{1+\Omega}$	$\frac{(R/\sigma)M\Omega}{1+\Omega}$	$N^2/2$		
Design Type 2	$R = \nu r$	Spine	T	$N = T/R$	0	N	$\frac{\nu N}{1+\Omega}$	$\frac{2\nu N^2}{1+\Omega}$	$\nu N^2 \times \left(\frac{\Omega}{1+\Omega}\right) \times \left(\frac{R}{\sigma}\right)$
		EoR			$\frac{N}{1+\Omega}$	$\frac{(R/\sigma)N\Omega}{1+\Omega}$	νN		
		AWGR	$2\nu R$	2ν	ν	ν	$\frac{N^2}{1+\Omega}$		

Defining the Rest of the Variables: Number of λ per Fiber $= \nu$, Bit rate per $\lambda = r$
Oversubscription Ratio $= \Omega \geq 1$, Bit Rate per Server $= \sigma$

note: [a] For ToR and EoR switches, this represents an *effective* switch radix.
[b] For ToR and EoR switches, this is the number of server ports.
[c] When $\nu = M/2$, the two designs will have the same number of servers.

3. Numerical Comparisons between Design Types 1 and 2

Numerical comparisons between Design Types 1 and 2 are given in Table 2 for the design scenarios represented by the circle, triangle, and square design points in Figs. 6, 7, 11, and 12. The results are presented for both 51.2 and 102.4 Tb/s switch sizes and for two representative values of the oversubscription ration, namely, $\Omega = 1{:}1$ and $\Omega = 3{:}1$. (Design Type 1.5 is not included in the comparisons because, as mentioned above, it does not represent a practical design on its own since it requires a large number of fibers.)

In all design scenarios, note that the large number of ToR switches required in Design Type 1 are eliminated in Design

Table 2. Comparing Different Scenarios of Design Types 1 and 2

Switch Size	Design Parameters	Design Point in Figs. 6, 7, 11, and 12: Circle		Triangle		Square	
T = 51.2 Tb/s	ToR Switch Size, τ, Tb/s	6.4		3.2		12.8	
	Server Bit Rate, σ, Gb/s	50		50		50	
	Bit Rate per λ, r, Gb/s	200		100		100	
	Fiber Bit Rate, R, Gb/s	800		400		800	
T = 102.4 Tb/s	ToR Switch Size, τ, Tb/s	12.8		6.4		25.6	
	Server Bit Rate, σ, Gb/s	100		100		100	
	Bit Rate per λ, r, Gb/s	400		200		200	
	Fiber Bit Rate, R, Gb/s	1,600		800		1,600	
Both Switch Sizes	# of λs per Fiber, ν	4		4		8	
	Radix of Large Switch, N	64		128		64	
	Radix of ToR Switch, M	8	--	8	--	16	--
Data Center Design Type →		1	2	1	2	1	2
Oversubscription Ratio, Ω: 1:1	# of Transceivers	32,768	16,384	131,072	65,536	65,536	32,768
	# of ToR Switches	2,048	--	8,192	--	2,048	--
	# of Large Switches	384	384	768	768	768	768
	# of $\nu \times \nu$ AWGRs	--	2,048	--	8,192	--	2,048
	# of Servers	**131,072**		**262,144**		**262,144**	
3:1	# of Transceivers	16,384	8,192	65,536	32,768	32,768	16,384
	# of ToR Switches	2,048	--	8,192	--	2,048	--
	# of Large Switches	192	320	384	640	384	640
	# of $\nu \times \nu$ AWGRs	--	1,024	--	4,096	--	1,024
	# of Servers	**196,608**		**393,216**		**393,216**	

Type 2 and replaced by an equal or smaller number of AWGRs. This is quite advantageous, since the cost of an AWGR is much less than that of a ToR switch. Moreover, the AWGRs eliminate the latency and power consumption associated with the ToR switches.

Note also the dramatic 50% reduction in the number of required transceivers in Design Type 2 compared to that in Design Type 1, which results in further reduction of cost and power consumption.

In all cases for $\Omega = 1{:}1$, the total required number of large switches is the same for Design Types 1 and 2. Thus, this does not affect the comparison. On the other hand, for $\Omega = 3{:}1$, the total required number of large switches in Design Type 1 is 60% of that required in Design Type 2. This will result in increased cost and power consumption for Design Type 2 associated with this part of the interconnect network. However, this increase will be more than offset by the corresponding elimination of the ToR switches and the dramatic reduction in the number of transceivers.

4. Considerations for ToR- versus EoR-Based Architectures

There are important differences between ToR-based designs, e.g., the conventional Design Type 1, and EoR-based designs, e.g., Design Type 2. (Additional considerations for using AWGRs in Design Type 2 will be discussed in Section 5.D.1.) Because of its relatively small size, a ToR switch supports only one rack of servers. Thus, the length of the links between the ToR switch and any server within its rack is of the order of a meter. Thus, these links have typically been copper-based. On the other hand, an EoR switch supports multiple racks of servers. In this case, the length of the links between the EoR switch and its servers can be of the order of several meters. Thus, these links should be realized using fiber-optic technology, e.g., based on VCSELs and MM fibers as described in Section 4.

Another important consideration is that a ToR switch failure will disable only one rack of servers, which is tolerable, while an EoR switch failure will disable multiple racks of servers, which might not be acceptable. A good way to mitigate this, which is depicted in Fig. 13, is to use double redundancy by homing each server to two different EoR switches within the same module. Ideally, both connections would be used during the non-failed state to provide high-bandwidth server connectivity. Then, upon failure of one EoR switch, the servers connected to it would still be connected to the rest of the system at half the bit rate, instead of being totally disconnected, as would be the case with no redundancy. A totally different option is to implement a one-for-N protection scheme, which would require the use of optical protection switches and somewhat longer fiber runs between the EoR switches and the servers. To reduce the number of fibers and to enable the longer fiber runs in this case, one can use coarse WDM (CWDM) and SM fibers in the links to the server racks instead of using VCSELs and MM fibers.

C. Disaggregated Data Centers

In a legacy data center, each server has its own storage, memory, processor, accelerator, etc. Depending on the overall workload,

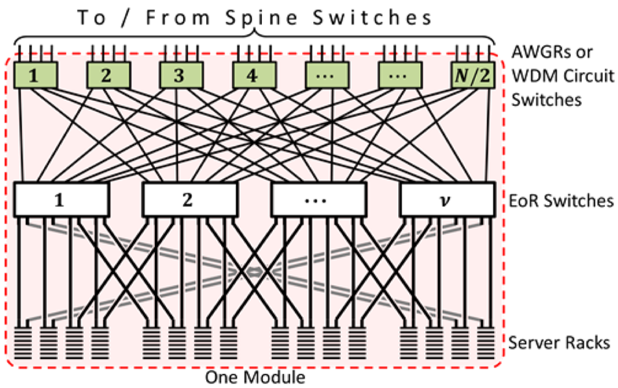

Fig. 13. Illustration of server double-homing redundancy to protect against a failure of an EoR switch within a module in Design Type 2.

these resources may not be used efficiently, i.e., they may be oversubscribed in one server while underutilized in another. The concept of a disaggregated data center involves placing a large part of these resources in a common location in the data center outside the servers, then sharing them among the servers [30]. The sharing results in increased utilization of the resources, leading to savings in cost and energy. But, to avoid bottlenecks between the servers and the shared resources, the connectivity between them needs to have high bandwidth and low latency [31]. Figure 14 shows a disaggregated data center based on Design Type 1, where some of the original server modules are replaced by various shared resources. A high-performance computing (HPC) cluster is included among the shared resources, which provides computationally intense functions such as artificial intelligence and machine learning (AI/ML). One of the desirable characteristics of this disaggregated design is that the EoR switches run across the entire data center, providing uniform interfaces to the servers and to the shared resources. Note that the path from a server to the shared resources involves passing through five electrical packet switches, and similarly in the reverse direction, which is likely to introduce a level of latency that may be too high for some applications.

To reduce latency and increase the bandwidth, various interesting, disaggregated data center architectures utilizing optical switches have been proposed in [32,33]. Here, we present a

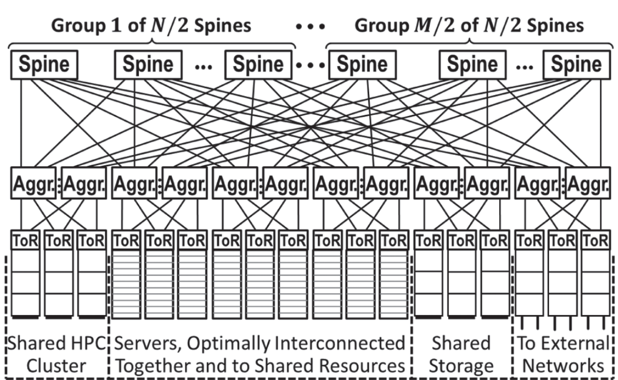

Fig. 14. Conventional disaggregated data center architecture based on Design Type 1.

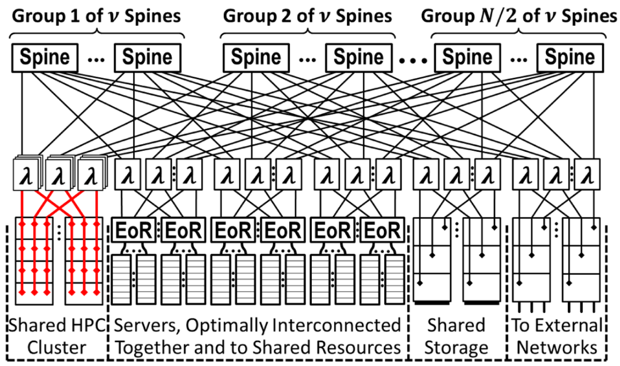

Fig. 15. Disaggregated data center based on Design Type 2. The λ boxes represent optical wavelength routing devices (AWGRs) or optical WDM circuit switches.

modified, scalable, low-latency architecture that is based on our Design Type 2. The new architecture is shown in Fig. 15.

Each of the λ boxes shown in Fig. 15 represents either a pair of $\nu \times \nu$ optical routing devices (AWGRs) or an optical $2\nu \times 2\nu$ WDM circuit switch (see Fig. 10). Note that the λ boxes run across the entire data center and provide uniform all-optical interfaces to the shared resources and to the EoR switches supporting the servers. The path from a server to the shared resources here passes through only two electrical packet switches, which will clearly reduce latency in comparison to the architecture of Fig. 14, where such a path passes through five electrical switches.

Considerations for and comparisons between using AWGRs or WDM circuit switches in data center architectures based on Design Type 2 are discussed next.

D. Contrasting the Use of AWGRs versus WDM Circuit Switches

As indicated by the results of Section 5.B.3, the enhanced economy and reduced power consumption of our novel data center Design Type 2 over those of the conventional Design Type 1 stem from including the layer of passive optical wavelength routing devices (AWGRs). Moreover, as mentioned earlier, Design Type 2 can be enhanced further by replacing the $\nu \times \nu$ AWGRs by $2\nu \times 2\nu$ WDM circuit switches (see Fig. 10). Here, we discuss various considerations for using these types of devices and contrast the differences between them.

1. Using AWGRs

Because of their wavelength dependence, there needs to be reasonable wavelength registration across each group of 2ν transceivers at the ports of the electronic switches connected to each of these devices. The degree of wavelength registration needs only to be sufficient for the various wavelengths to pass through the passbands of the AWGR. Generating wavelengths with this required stability across a large temperature operating range using uncooled lasers has been demonstrated [34]. This also requires the AWGRs to be reasonably athermal.

Because we use polarization multiplexing, another important requirement of the AWGRs is that they need to be polarization independent, or at least to have small polarization-dependent loss, so that they are compatible with the polarization control scheme that we are using [9]. Photonic fabrication technologies have been developed that are capable of achieving the above AWGR requirements of being athermal, polarization independent, and to have flat passbands (e.g., see [35]).

Because the AWGRs are passive devices, and because the associated transceivers are not tunable, Design Type 2 represents a conventional packet-switched network with *fixed* inter-switch connections (same as in Design Types 1 and 1.5). Hence, this AWGR-based design requires no changes in the underlying IP and/or Ethernet protocols.

2. Using WDM Circuit Switches

Using optical circuit switches to enhance the performance of data centers has been widely reported in the literature [36–43]. Here, we focus on architectures related to replacing the AWGRs in our Design Type 2 by WDM circuit switches in a similar way as initially suggested in [29,39,43]. The mode of operation that we are envisioning for the WDM circuit switches is to reconfigure them in a quasi-static regime (e.g., in seconds or longer) to respond to slowly changing types of workloads or computational scenarios. In this case, the added latency introduced by the reconfiguration process of the WDM switches will, on average, be negligible in comparison to other latencies in the system. Thus, in effect, since the path of a signal through a WDM switch is all-optical, its latency will be comparable to that of a static AWGR. But, the ability to reconfigure the WDM switches to match slow changes in the workload will increase utilization of the servers, thus reducing the system-wide latency and increasing the overall energy efficiency.

Note that the existing underlying Ethernet and IP protocols need not be changed, since the data center network reconfigurability that we require is sufficiently slow. On the other hand, if one wants to extend the vision to have the WDM switches respond to fast workload variations (e.g., in sub-milliseconds), then whole new protocols would be needed. This would be quite a challenging and costly task, which we are not currently considering.

Another important advantage of using the WDM switches, instead of the AWGRs, is that they can accommodate the variety of bandwidth requirements of the different types of end devices connected to a disaggregated data center. For example, consider the architecture of Fig. 15 with each of the fiber links having $\nu = 4$ wavelengths, with $r = 200$ Gb/s per wavelength, for a total of $R = 800$ Gb/s per fiber. If the λ boxes in the figure are AWGRs, the connectivity of all end devices would be at 200 Gb/s per port. If WDM switches are used instead, the connectivity of the end devices can be provisioned to achieve 200, 400, or 800 Gb/s per port. The high-bandwidth connectivity is quite desirable, especially in the latency-sensitive connections to the shared HPC cluster.

We are conducting various investigations under a different program on suitable types of WDM switches based on microring resonators [44–46]. Another promising type of WDM switches, which is based on microelectromechanical systems (MEMS) technology, has also been reported in the literature [47]. All of these WDM switches, as well as other types reported in the literature, are not polarization-independent because they have a significant amount of polarization-dependent loss. Work is in progress on reducing the polarization dependence of these switches and, at the same time, on modifying the polarization control scheme that we are currently employing [9] to accommodate any residual polarization-dependent loss. Other schemes involving polarization diversity are also being considered.

3. Comparing Packet Latencies

As a demonstration of the difference in packet latency performance among various versions of Design Type 1 and Design Type 2 (with AWGRs or with WDM switches), consider a data center performing a computational task that involves multiple servers that are distributed across the data center. A reasonable measure of the packet latency performance is the estimated average number of electronic packet switches (which we will denote by $\bar{S}$) that need to be traversed to perform the computation as a function of the extent across the data center of the servers involved in the computation. (Note that not all of the servers in that range are necessarily involved in the computation, just a subset of them). The less $\bar{S}$ is, the less the expected latency is, and the better the computational performance is. Figure 16 shows plots representing this scenario for various types of data center designs.

For example, as shown in the figure for Design Type 1, if the servers involved in the computation are all within one rack, $\bar{S}$ would be exactly one (the ToR switch supporting the rack). If the two ends of the servers involved extend beyond one rack, but still within one module, then some of the interconnections among them need to go through an aggregation switch. Thus, $\bar{S}$ will increase towards three (two ToR switches and one aggregation switch). If the servers extend beyond one module, the spine switches will have to get involved, and $\bar{S}$ will increase toward five (two ToR switches, two aggregation switches, and one spine switch).

As shown in Fig. 16, in all cases of Design Type 2, if the servers involved are within an EoR domain, $\bar{S}$ would be exactly one (the EoR switch). This is of course a great improvement over Design Type 1 in that range, since an EoR switch covers multiple racks of servers, while a ToR switch covers just one rack.

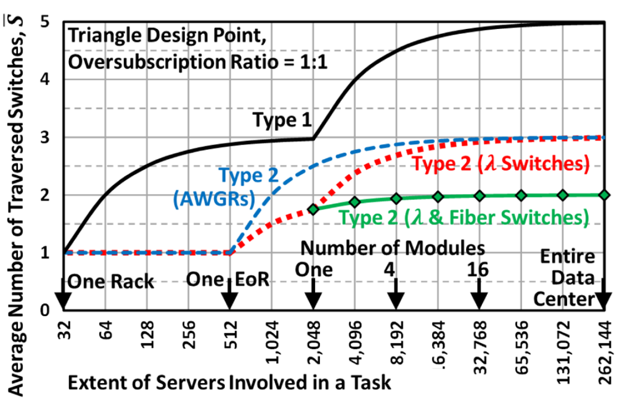

Fig. 16. Average number, $\bar{S}$, of traversed electronic packet switches to perform a computational task involving multiple servers versus the extent of the involved servers across the data center.

In the AWGR case, if the servers extend beyond the domain of one EoR, then the spine switches need to be involved, and $\bar{S}$ will increase toward three (two EoR switches and one spine switch), as the servers involved extend toward the whole data center. Note that the AWGRs cannot directly interconnect two EoRs, even within one module. On the other hand, if WDM circuit switches are used, then, as indicated in Fig. 10, they can loop back the signal and directly interconnect multiple EoRs within a module. But, beyond one module, the spine switches need to be involved, and $\bar{S}$ will increase toward three (two EoRs and one spine).

One can improve the performance further in the range beyond one module by enhancing the architecture by adding an array of fiber switches (e.g., MEMS switches) in a new layer between the WDM switches and spine switches (which is not shown in the figures). In this case, EoR switches can be directly interconnected across multiple modules. Thus, $\bar{S}$ would increase towards only two beyond one module. If we need to interconnect Q modules, each of the fiber switches needs to be connected to just one fiber port of each module, i.e., the fiber switch size would be $2Q \times 2Q$, and the number of such switches would be equal to the number of fiber ports at the top of each module, which is equal to $N/2$, where N is the effective radix of the EoR switch. Admittedly, this represents an added expenditure in the data center, but the added layer of fiber switches can potentially perform other useful functions in the data center such as upgrades, maintenance, and restoration. This subject is still under investigation.

6. SUMMARY AND OUTLOOK

We have summarized the technology and network architectural visions of the INTREPID project. The technology pursues the use of coherent QPSK, polarization-multiplex transceivers enhanced with WDM to enable energy-efficient 800 or 1600 Gb/s inter-switch fiber links. CPO is pursued for integrating the transceivers with next-generation 51.2 and 102.4 Tb/s electronic switching ASICs to enable the realization of future hyper-scale data centers that are flatter and more energy-efficient than current designs. The technology is compatible with conventional three-level data center designs as well as a newly introduced two-level data center design that includes an added layer of passive AWGRs or WDM circuit switches to further reduce cost, power consumption, and latency.

The second phase of INTERPID, which began in late 2020, focuses on robust demonstrations of analog coherent transceiver assemblies and a transition of the technology developed in the program to widespread commercial adoption [48]. The benefits of deploying WDM switches, possibly in combination with fiber switches, in the data center will also be further investigated and quantified to help to make the case for practical deployment of the novel data center architectures proposed here.

Funding. Advanced Research Projects Agency - Energy (DE-AR0000848).

Acknowledgment. The authors thank the ARPA-E team for management and guidance: James Zahler, Michael Haney, and John Qi. The authors greatly appreciate the technical contributions and rewarding collaborations with their colleagues at Facebook (James Stewart, Hans-Juergen Schmidtke, Todd Hollmann, and Jimmy Williams) and UCSB (Hector Andrade, Takako Hirokawa, Junqian Liu, Aaron Maharry, Stephen Misak, Luis Valenzuela, and Yujie Xia). The information, data, or work presented herein was funded in part by the Advanced Research Projects Agency - Energy (ARPA-E), U.S. Department of Energy, (DE-AR0000848). The views and opinions of authors expressed herein do not necessarily state or reflect those of the United States Government or any agency thereof.

Disclosures. The authors declare no conflicts of interest.

REFERENCES

1. Cisco, "Cisco annual Internet report (2018–2023)," 2020, https://www.cisco.com/c/en/us/solutions/collateral/executive-perspectives/annual-internet-report/white-paper-c11-741490.html.
2. Cisco, "Cisco global cloud index: forecast and methodology, 2016–2021," 2018, https://virtualization.network/Resources/Whitepapers/0b75cf2e-0c53-4891-918e-b542a5d364c5_white-paper-c11-738085.pdf.
3. C. L. Schow and K. E. Schmidtke, "INTREPID: developing power efficient analog coherent interconnects to transform data center networks," in *Optical Fiber Communication Conference (OFC)*, OSA Technical Digest (Optical Society of America, 2019), paper M4D.9.
4. "Co-packaged optics collaboration," http://www.copackagedoptics.com/.
5. ISSCC, "ISSCC 2020 trends," 2020, http://isscc.org/wp-content/uploads/sites/17/2020/03/isscc2020.press_kit_final.pdf.
6. T. O. Dickson, Y. Liu, S. V. Rylov, A. Agrawal, S. Kim, P.-H. Hsieh, J. F. Bulzacchelli, M. Ferriss, H. A. Ainspan, A. Rylyakov, B. D. Parker, M. P. Beakes, C. Baks, L. Shan, Y. Kwark, J. A. Tierno, and D. J. Friedman, "A 1.4 pJ/bit, power-scalable 16 × 12 Gb/s source-synchronous I/O with DFE receiver in 32 nm SOI CMOS technology," IEEE J. Solid-State Circuits **50**, 1917–1931 (2015).
7. G. P. Agrawal, *Fiber-Optic Communication Systems* (Wiley, 2012).
8. T. Hirokawa, S. Pinna, D. Hosseinzadeh, A. Maharry, H. Andrade, J. Liu, T. Meissner, S. Misak, G. Movaghar, L. A. Valenzuela, Y. Xia, S. Bhat, F. Gambini, J. Klamkin, A. A. M. Saleh, L. Coldren, J. F. Buckwalter, and C. L. Schow, "Analog coherent detection for energy efficient intra-data center links at 200 Gbps per wavelength," J. Lightwave Technol. **39**, 520–531 (2021).
9. J. K. Perin, A. Shastri, and J. M. Kahn, "Design of low-power DSP-free coherent receivers for data center links," J. Lightwave Technol. **35**, 4650–4662 (2017).
10. P. R. A. Binetti, M. Lu, E. J. Norberg, R. S. Guzzon, J. S. Parker, A. Sivananthan, A. Bhardwaj, L. A. Johansson, M. J. Rodwell, and L. A. Coldren, "Indium phosphide photonic integrated circuits for coherent optical links," IEEE J. Quantum Electron. **48**, 279–291 (2012).
11. M. Lu, H. Park, E. Bloch, A. Sivananthan, J. S. Parker, Z. Griffith, L. A. Johansson, M. J. W. Rodwell, and L. A. Coldren, "An integrated 40 Gbit/s optical Costas receiver," J. Lightwave Technol. **31**, 2244–2253 (2013).
12. C. L. Schow, A. A. M. Saleh, and K. E. Schmidtke, "Intrepid update: ARPA-E ENLITENED annual meeting," 2018, https://arpa-e.energy.gov/sites/default/files/Schow_ENLITENED2018.pdf.
13. C. L. Schow, A. A. M. Saleh, and K. E. Schmidtke, "INTREPID update: ARPA-E ENLITENED annual meeting," 2019, https://arpa-e.energy.gov/sites/default/files/UCSB_Schow_ENLITENED_Annual_Meeting.pdf.
14. Y. Xia, L. Valenzuela, A. Maharry, S. Pinna, S. Dwivedi, T. Hirokawa, J. Buckwalter, and C. Schow, "A fully integrated O-band coherent optical receiver operating up to 80 Gb/s," in *IEEE Photonics Conference (IPC)*, Virtual Conference (2021).
15. H. Andrade, Y. Xia, A. Maharry, L. Valenzuela, J. Buckwalter, and C. Schow, "50 GBaud QPSK 0.98 pJ/bit receiver in 45 nm CMOS and 90 nm silicon photonics," in *European Conference on Optical Communications (ECOC)*, Bordeaux, France (2021).
16. H. Andrade, T. Hirokawa, A. Maharry, A. Rylyakov, C. L. Schow, and J. F. Buckwalter, "Monolithically-integrated 50Gbps 2pJ/bit photoreceiver with Cherry-Hooper TIA in 250 nm BiCMOS technology," in *Optical Fiber Communication (OFC) Conference*, San Diego, California, March 2019.
17. H. Andrade, A. Maharry, T. Hirokawa, L. Valenzuela, S. Pinna, S. Simon, C. L. Schow, and J. F. Buckwalter, "Analysis and monolithic implementation of differential transimpedance amplifiers," J. Lightwave Technol. **38**, 4409–4418 (2020).
18. N. Hosseinzadeh, K. Fang, L. Valenzuela, C. L. Schow, and J. F. Buckwalter, "A 50-Gb/s optical transmitter based on co-design of a 45-nm CMOS SOI distributed driver and 90-nm silicon photonic Mach–Zehnder modulator," in *IEEE/MTT-S International Microwave Symposium (IMS)*, Online Conference, June 2020.
19. A. Maharry, H. Andrade, T. Hirokawa, J. F. Buckwalter, and C. L. Schow, "A novel architecture for a two-tap feed-forward optical or electrical domain equalizer using a differential element," in *IEEE Photonics Conference*, San Antonio, Texas, October 2019.
20. L. A. Valenzuela, A. Maharry, H. Andrade, C. L. Schow, and J. F. Buckwalter, "A 108-Gbps, 162-mW Cherry-Hooper transimpedance amplifier," in *IEEE BiCMOS and Compound Semiconductor Integrated Circuits and Technology Symposium*, Online Conference (2020).
21. J. E. Proesel, B. G. Lee, C. W. Baks, and C. L. Schow, "35-Gb/s VCSEL-based optical link using 32-nm SOI CMOS circuits," in *Optical Fiber Communications Conference*, Anaheim, California (2013).
22. D. M. Kuchta, A. V. Rylyakov, F. E. Doany, C. L. Schow, J. E. Proesel, C. W. Baks, P. Westbergh, J. S. Gustavsson, and A. Larsson, "A 71 Gb/s NRZ modulated 850 nm VCSEL-based optical link," IEEE Photon. Technol. Lett. **27**, 577–580 (2015).
23. M. Filer, "Opportunities for co-packaging in future microsoft data center networks," 2021, https://arpa-e.energy.gov/sites/default/files/2021-02/DAY2_Filer_ENLITENED_Phase2_Kickoff.pdf.
24. D. M. Kuchta, "Multi-wavelength optical transceivers integrated on node," 2019, https://arpa-e.energy.gov/sites/default/files/IBM_Kuchta_ENLITENED_Annual_Meeting.pdf.
25. A. V. Rylyakov, C. L. Schow, B. G. Lee, F. E. Doany, C. W. Baks, and J. A. Kash, "Transmitter pre-distortion for simultaneous improvements in bit-rate, sensitivity, jitter, and power efficiency in 20 Gb/s CMOS-driven VCSEL links," J. Lightwave Technol. **30**, 399–405 (2012).
26. L. A. Valenzuela, L. Andrade, N. Hosseinzadeh, A. Maharry, C. L. Schow, and J. F. Buckwalter, "A 2.85 pJ/bit, 52-Gbps NRZ VCSEL driver with two-tap feedforward equalization," in *IEEE/MTT-S International Microwave Symposium (IMS)*, Online Conference, June 2020.
27. A. Maharry, L. Valenzuela, H. Andrade, I. Kalifa, I. Cestier, M. Galanty, B. Atias, A. Sandomirsky, E. Mentovich, L. Coldren, J. Buckwalter, and C. L. Schow, "A 50 Gbps 9.5 pJ/bit VCSEL-based optical link," in *IEEE Photonics Conference (IPC)*, Virtual Conference (2021).
28. Broadcom, "Broadcom ships Tomahawk 4, industry's highest bandwidth Ethernet switch chip at 25.6 terabits per second," 2019, https://www.broadcom.com/company/news/product-releases/52756.
29. A. A. M. Saleh, "Scaling-out data centers using photonics technologies," in *Photonics in Switching Conference in Advanced Photonics for Communications*, San Diego, California, July 2014.
30. A. D. Papaioannou, R. Nejabati, and D. Simeonidou, "The benefits of a disaggregated data centre: a resource allocation approach," in *IEEE GLOBECOM* (2016).
31. P. X. Gao, A. Narayan, S. Karandikar, J. Carreira, S. Han, R. Agarwal, S. Ratnasamy, and S. Shenker, "Network requirements for resource disaggregation," in *12th USENIX Symposium on Operating Systems Design and Implementation (OSDI)* (2016).
32. R. Lin, Y. Cheng, M. De Andrade, L. Wosinska, and J. Chen, "Disaggregated data centers: challenges and trade-offs," IEEE Commun. Mag. **58**(2), 20–26 (2020).
33. Q. Cheng, Y. Huang, H. Yang, M. Bahadori, N. Abrams, X. Meng, M. Glick, Y. Liu, N. Hochberg, and K. Bergman, "Silicon photonic switch topologies and routing strategies for disaggregated data centers," IEEE J. Sel. Top. Quantum Electron. **26**, 8302010 (2020).
34. B. R. Koch, E. J. Norberg, B. Kim, J. Hutchinson, J.-H. Shin, G. Fish, and A. Fang, "Integrated silicon photonic laser source for telecom and datacom," in *Optical Fiber Communication Conference*

and Exposition/National Fiber Optics Engineers Conference (OFC/NFOEC) (2013).
35. A. J. Zilkie, P. S. Srinivasan, A. Trita, T. Schrans, G. Yu, J. Byrd, D. A. Nelson, K. Muth, D. Lerose, M. Alalusi, K. Masuda, M. Ziebell, H. Abediasl, J. J. Drake, G. Miller, H. Nykanen, E. Kho, Y. Liu, H. Liang, H. Yang, F. H. Peters, A. S. Nagra, and A. G. Rickman, "Multi-micron silicon photonics platform for highly manufacturable and versatile photonic integrated circuits," IEEE J. Sel. Top. Quantum Electron. **25**, 8200713 (2019).
36. N. Farrington, G. Porter, S. Radhakrishnan, H. H. Bazzaz, V. Subramanya, Y. Fainman, G. Papen, and A. Vahdat, "Helios: a hybrid electrical/optical switch architecture for modular data centers," in *SIGCOMM* (2010).
37. G. Porter, R. Strong, N. Farrington, A. Forencich, C.-S. Pang, T. Rosing, Y. Fainman, G. Papen, and A. Vahdat, "Integrating microsecond circuit switching into the data center," in *SIGCOMM* (2013).
38. H. Liu, F. Lu, A. Forencich, R. Kapoor, M. Tewari, G. M. Voelker, G. Papen, A. C. Snoeren, and G. Porter, "Circuit switching under the radar with REACToR," in *USENIX Symposium on Networked Systems Design and Implementation (NSDI)* (2014).
39. A. A. M. Saleh, A. S. P. Khope, J. E. Bowers, and R. C. Alferness, "Elastic WDM switching for scalable data center and HPC interconnect networks," in *OECC/Photonics in Switching Conference*, Niigata, Japan, July 2016.
40. M. Ghobadi, R. Mahajan, A. Phanishayee, N. Devanur, J. Kulkarni, G. Ranade, P.-A. Blanche, H. Rastegarfar, M. Glick, and D. Kilper, "ProjecToR: agile reconfigurable data center interconnect," in *SIGCOMM* (2016).
41. W. M. Mellette, R. McGuinness, A. Roy, A. Forencich, G. Papen, A. C. Snoeren, and G. Porter, "RotorNet: a scalable, low-complexity, optical datacenter network," in *SIGCOMM* (2017).
42. K. Bergman, J. Shalf, G. Michelogiannakis, S. Rumley, L. Dennison, and M. Ghobadi, "PINE: an energy efficient flexibly interconnected photonic data center architecture for extreme scalability," in *IEEE Optical Interconnects Conference* (2018).
43. R. Helkey, A. A. M. Saleh, J. Buckwalter, and J. E. Bowers, "High-performance photonic integrated circuits on silicon," IEEE J. Sel. Top. Quantum Electron. **25**, 8300215 (2019).
44. A. S. P. Khope, M. Saeidi, R. Yu, X. Wu, A. M. Netherton, Y. Liu, Z. Zhang, Y. Xia, G. Fleeman, A. Spott, S. Pinna, C. Schow, R. Helkey, L. Theogarajan, R. C. Alferness, A. A. M. Saleh, and J. E. Bowers, "Multi-wavelength selective crossbar switch," Opt. Express **27**, 5203–5216 (2019).
45. T. Hirokawa, A. Maharry, R. Helkey, J. E. Bowers, A. A. M. Saleh, and C. L. Schow, "Demonstration of a spectrally-partitioned 4x4 crossbar switch with 3 drops per cross-point," in *Optoelectronics and Communications Conference/International Conference Photonics in Switching and Computing (OECC/PSC)* (2019).
46. T. Hirokawa, M. Saeidi, S. Pillai, A. Nguyen-Le, L. Theogarajan, A. A. M. Saleh, and C. L. Schow, "A wavelength-selective multi-wavelength ring-assisted Mach–Zehnder interferometer switch," J. Lightwave Technol. **38**, 6292–6298 (2020).
47. T. J. Seok, J. Luo, Z. Huang, K. Kwon, J. Henriksson, J. Jacobs, L. Ochikubo, S. R. Muller, and C. M. Wu, "Silicon photonic wavelength cross-connect with integrated MEMS switching," APL Photon. **4**, 100803 (2019).
48. "INTREPID Phase 2," 2021, https://arpa-e.energy.gov/sites/default/files/2021-01/DAY1_Schow_ENLITENED_Phase2_Kickoff.pdf.

Adel A. M. Saleh (A'65–M'70–SM'76–F'87–LF'08) obtained a B.Sc. degree from Alexandria University, Egypt, and M.S. and Ph.D. degrees from MIT, Cambridge, MA, in 1963, 1967, and 1970, respectively, all in electrical engineering. He is currently a Research Professor with the Department of Electrical and Computer Engineering and the Institute for Energy Efficiency, University of California, Santa Barbara (UCSB), Santa Barbara, CA, USA, since October 2011, conducting research on optical networking and photonic technology for chip-scale to global-scale networking applications, with emphasis on data centers and high-performance computing. From 2005 to 2011, he was a DARPA Program Manager, where he initiated several research programs on advanced optical networking. From 1999 to 2004, he held leadership positions in the optical networking industry, including Corvis, the first company to commercialize national-scale all-optical networks. From 1970 to 1999, he was with Bell Labs/AT&T Labs Research conducting and leading research on optical and wireless networks. Between 1992 and 1999, he led the AT&T effort on several multi-million-dollar, cross-industry, DARPA-funded consortia that pioneered the vision of all-optical networking in backbone, regional, metro, and access networks. Dr. Saleh received the AT&T Bell Labs Distinguished Technical Staff Award for Sustained Achievement in 1985. He is a Fellow of Optica and a Life Fellow of the IEEE, has published more than 100 journal and conference papers, and has 25 issued patents.

Katharine E. Schmidtke received a B.Sc. degree in physics and mathematics from Keele University, UK, in 1989 and a Ph.D in laser physics and nonlinear optics from the University of Southampton in 1993. She went on to complete postdoctoral research in epitaxial growth of nonlinear optical materials at Stanford University, CA, USA. She has a 25-year career in the optical communications industry including roles at Finisar, JDS Uniphase, and New Focus. For the past 7 years she has worked at Facebook, Menlo Park, CA, where she has driven the technology strategy for data center optical interconnects. She is currently Director of Sourcing for ASICS and Custom Silicon focused on AI/ML applications. Dr. Schmidtke is a Fellow of Optica and has been an invited speaker and served on committees for numerous international conferences, including the Optical Fiber Communication Conference (OFC), the European Conference on Communications (ECOC), and the Optical Interconnects Conference.

Robert J. Stone received his B.Sc. from The University of Sheffield in 1993 and a D.Phil. from The University of Oxford in 1997 in physics. He currently holds the role of Technical Sourcing Manager at Facebook, focusing on next-generation high-speed interconnects. Prior to Facebook, Dr. Stone was a distinguished engineer at Broadcom within the switch architecture team, where he was responsible for the switch IO ecosystem and system design, actively representing Broadcom in a number of industry groups, including IEEE as well as MSA and industry organizations. He has over 20 years of industry experience bringing communications technologies to market and has held both technical and managerial positions at Broadcom, Intel, Infinera, Emcore, Skorpios Technologies, and Bandwidth 9.

James F. Buckwalter (SM'10) received a B.S.E.E. degree with honors in electrical engineering from the California Institute of Technology (Caltech), Pasadena, in 1999; an M.S. degree from the University of California, Santa Barbara (UCSB), in 2001; and a Ph.D. degree in electrical engineering from Caltech in 2006. He is currently a Professor of Electrical and Computer Engineering with UCSB. From 1999 to 2000, he was a Research Scientist with Telcordia Technologies. During Summer 2004, he was with the IBM T. J. Watson Research Center, Yorktown Heights, NY. In July 2006, he joined the faculty of the University of California, San Diego (UCSD) as an Assistant Professor and was promoted to Associate Professor in 2012. He joined UCSB in 2014 as a Full Professor. Dr. Buckwalter was the recipient of a 2004 IBM Ph.D. Fellowship, 2007 Defense Advanced Research Projects Agency (DARPA) Young Faculty Award, 2011 NSF CAREER Award, and 2015 IEEE MTT-S Young Engineer Award. He is a senior member of the IEEE. He has published more than 200 conference and journal papers and advised more than 20 Ph.D. students.

Larry A. Coldren (S'67–M'72–SM'77–F'82–LF'12) received a B.S. in electrical engineering and a B.A. in physics from Bucknell University and joined Bell Laboratories in 1968. Under Bell Lab's support he then attended Stanford University and received M.S. and Ph.D. degrees in electrical engineering in 1969 and 1972, respectively. Following 13 years in the research area with Bell Laboratories, he joined the ECE Department of the University of California, Santa Barbara (UCSB) in 1984. In 1986 he was a founding member of the Materials Department. He became the Fred Kavli Professor of Optoelectronics and Sensors in 1999. From 2009 to 2011, he was acting Dean of the College of Engineering, and in 2017 he became

Professor Emeritus and a Distinguished Research Professor. In 1990, he co-founded Optical Concepts, later acquired as Gore Photonics, to develop novel vertical-cavity surface-emitting laser (VCSEL) technology, and, in 1998, he cofounded Agility Communications, later acquired by JDSU (now Lumentum), to develop widely tunable integrated transmitters and transponders. At UCSB, he has worked on multiple-section widely tunable lasers and efficient VCSELs. He continues to research high-performance InP-based photonic integrated circuits and high-speed, high-efficiency VCSELs for various applications. Prof. Coldren has authored or coauthored over 1000 journal and conference papers, 8 book chapters, a widely used textbook, and 63 issued patents. He is a fellow of IEEE, Optica, IEE, and the National Academy of Inventors, as well as a member of the National Academy of Engineering. He has been a recipient of the 2004 John Tyndall, the 2009 Aron Kressel, the 2014 David Sarnoff, the 2015 IPRM, and the 2017 Nick Holonyak, Jr., Awards.

Clint L. Schow (SM'10–F'18) received B.S., M.S., and Ph.D. degrees from the University of Texas at Austin in 1994, 1997, and 1999, respectively. After positions at IBM and Agility Communications, he spent more than a decade at the IBM T. J. Watson Research Center in Yorktown Heights, NY, as a Research Staff Member and Manager of the Optical Link and System Design group. In 2015, he joined the faculty of the University of California, Santa Barbara. He has led international R&D programs spanning chip-to-chip optical links; VCSEL and Si photonic transceivers; nanophotonic switches; and new system architectures enabled by high-bandwidth, low-latency photonic networks. Dr. Schow has been an invited speaker and served on committees for numerous international conferences, including roles as General Chair for the Optical Fiber Communications Conference (OFC), the Optical Interconnects Conference, and the Photonics in Switching Conference. He is a Fellow of Optica and the IEEE, has published more than 200 journal and conference articles, and has 33 issued patents.

Integrated phase-locked lasers and photonic integrated circuits for remote gas sensing

Jonathan Klamkin[1*], Fengqiao Sang[1], Joseph Fridlander[1], Victoria Rosborough[1], Fabrizio Gambini[2], Simone Tommaso Šuran Brunelli[1], Larry Coldren[1], Jeffrey R. Chen[2], Stephan Kawa[2], Kenji Numata[2], Mark Stephen[2]

[1]*Electrical and Computer Engineering Department, University of California Santa Barbara, Santa Barbara, CA 93106 USA*
[2]*NASA Goddard Space Flight Center, Greenbelt, MD 20771 USA*
**Email:* klamkin@ece.ucsb.edu

2021 27th International Semiconductor Laser Conference (ISLC) | 978-1-6654-4133-9/21/$31.00 ©2021 IEEE | DOI: 10.1109/ISLC51662.2021.9615893

Abstract – An indium phosphide photonic integrated circuit for integrated path differential absorption lidar remote gas sensing was developed. Phase locking of the two integrated lasers and measurement of a carbon dioxide absorption line centered at 1572.335 nm was demonstrated.

I. Introduction

Photonic integrated circuit (PIC) technology enables a significant reduction in the cost, size, weight and power (CSWaP) of systems for free space communication and sensing applications [1-6]. This also enables the possibility to deploy photonic systems on small space platforms including CubeSats [5]. The indium phosphide (InP) PIC platform is able to monolithically integrate lasers, modulators, photodiodes, semiconductor optical amplifiers (SOAs) and passive components [1-6]. In this work, an InP PIC was developed for integrated path differential absorption (IPDA) lidar for remote sensing of carbon dioxide (CO_2) [6-8]. The PIC lidar is designed to scan over 40 GHz range around the center of a CO_2 absorption line at 1572.335 nm. This method requires accurate and fast wavelength tuning. A two-laser PIC comprising of a leader laser and follower laser was developed [7], The leader laser is stabilized with an absolute reference, a CO_2 cell. The follower laser is offset locked to the leader laser through an optical phase lock loop (OPLL) to ensure accuracy of the output wavelength. A SOA following the follower laser is used to encode frequency stepped optical pulses for scanning the 1572.335 nm absorption line. This work represents a significant step toward reducing system CSWaP for IPDA lidar systems for space applications.

II. Photonic Integrated Circuit

The PIC footprint is 0.8 mm × 8.3 mm as shown in Fig. 1. The PIC comprises of two lasers, couplers, a high speed photodiode for beat note detection, a phase modulator for the OPLL, and a SOA for encoding pulses. Both the leader and follower lasers share the same sampled grating distributed Bragg reflector (SGDBR) laser design with a center emission wavelength near 1572 nm. The laser gain medium comprises of seven quantum wells. The SGDBR gain section is 550 µm long, the phase section is 75 µm, and the backside SOA, used for monitoring, is 500 µm long. Both the front and back SGDBR mirrors use a grating period of 244 nm corresponding to a Bragg wavelength at 1573.6 nm. The front mirror consists of 5 grating bursts, while the back mirror consists of 12 grating bursts. Two different directional couplers were used for power splitting. Coupler A has a length of 180 µm and is

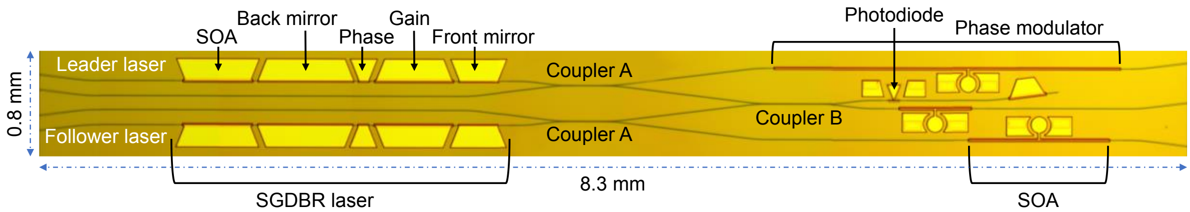

Figure 1: Microscope image of fabricated PIC for IPDA lidar remote gas sensing.

designed for a splitting ratio of 80/20. This coupler design is used to routes most of the leader laser output to the phase modulator for the stabilization, and most of the follower laser output to the SOA pulse encoder. Coupler B, with a length of 320 µm, is designed for a splitting ratio of 50/50. This coupler mixes the two lasers' outputs and then splits for on-chip photodiode beat note detection and off-chip detection or monitoring. The 2500 µm long phase modulator is modulated at 125 MHz to generate a phase signal, which is used to stabilize the leader laser using the absolute CO_2 reference cell. The integrated photodiode demonstrates a bandwidth 15 GHz [6], enabling beat note detection for the OPLL offsetting locking and subsequent sweeping of the follower laser around the center of the absorption line. The 1000 µm long SOA on the follower laser side of the PIC provides greater than 40 dB DC extinction. This is used to generate high extinction pulses for the follower laser output.

III. Measurement Results

The SGDBR lasers used for the leader and follower were characterized and Fig. 2(a) shows exemplary light-current-voltage (LIV) characteristics at various stage temperatures. The laser threshold current is approximately 33 mA at a temperature of 15 °C and the laser outputs greater than 10 mW at a drive current of 200 mA. The lasers tune over a range of more than 40 nm, between 1560 nm to 1600 nm, with more than 45 dB side mode suppression ratio (SMSR) as shown in Fig. 2(b). The lasers also demonstrate a 3-dB linewidth of 4.4 MHz as shown in Fig 2(c). While the lasers can be coarsely tuned using the front and back SGDBR mirrors, the phase section can be used for fine and continuous tuning. As shown in Fig. 2(d), by adjusting the phase section current between 9 and 13 mA, the laser wavelength is tuned passed 1572.335 nm.

In addition to characterizing the lasers, PIC operation was also demonstrated. We successfully demonstrated offset locking between the lasers at 1572.335 nm as shown in Fig.2(e). Here, the leader laser was stabilized with

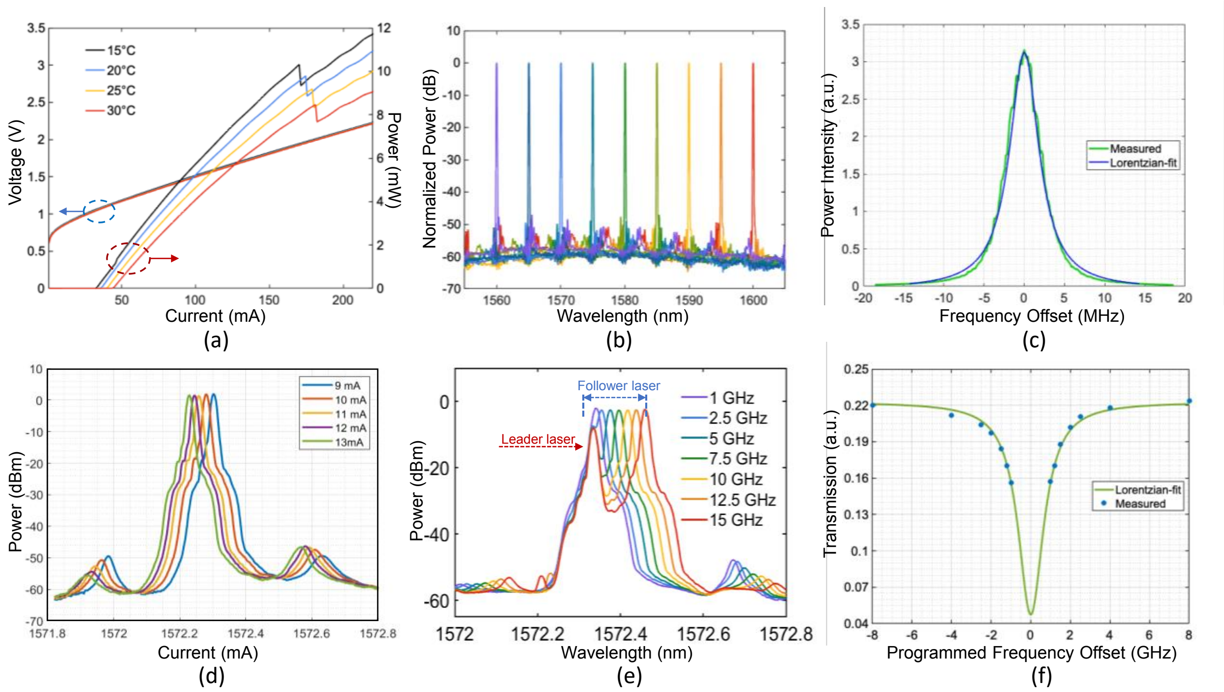

Figure 2. (a) LIV characteristics of SGDBR laser at varying stage temperatures. (b) Laser spectra showing tuning from 1560 nm to 1600 nm. (c) Delayed self-heterodyne linewidth measurement with Lorentzian fit. (d) Laser spectra with continuous tuning around 1572.335 nm using the laser phase section. (e) Spectra of the leader and follower laser as the leader laser is offset locked from 1 GHz to 15 GHz. (f) Measured absorption of a separate CO_2 test cell at 14 wavelength points where each point is an average of 1000 measurements taken over 100 µs.

the CO_2 reference cell, and the follower laser was offset locked to the leader while tuning to offsets between 1 and 15 GHz. Using a separate CO_2 cell for the follower laser output, the CO_2 absorption line was measured. As shown in Fig. 2(f), 14 points were sampled around the CO_2 absorption line centered at 1572.335 nm. Using these sampled points, the overall absorption spectrum was estimated using a Lorentzian fit. These measurements demonstrate the overall operation of the IPDA lidar PIC for CO_2 sensing in a laboratory environment.

IV. Conclusion

We have developed an InP PIC for IPDA lidar remote sensing of CO_2. This PIC enables the stabilization of a leader laser with an absolute CO_2 gas reference cell, and the subsequent offset locking and sweeping of a follower laser to measure the CO_2 absorption line centered at 1572.335 nm. This work represents a major step toward miniaturizing lidar systems for sensing applications and deployment on small space platforms.

V. Acknowledgement

The authors acknowledge funding from NASA's Earth Science Technology Office (ESTO) Advanced Component Technology (ACT) program. A portion of this work was performed in the UCSB Nanofabrication Facility.

VI. References

[1] H. Zhao, et al., IEEE Journal of Selected Topics in Quantum Electronics, 25.6 (2019)
[2] B. J. Isaac, et al., IEEE Journal of Selected Topics in Quantum Electronics, 25.6 (2019)
[3] H. Zhao, et al., IEEE Journal of Selected Topics in Quantum Electronics, 24.6 (2018)
[4] J. Klamkin, et al., IEEE BCICTS, (2018)
[5] M. Krainak, et al., Proc. SPIE 10899, Components and Packaging for Laser Systems V, 108990F (4 March 2019)
[6] J. Fridlander, et al., CLEO: Science and Innovations. Optical Society of America, (2020)
[7] K. Numata, J. R. Chen, S. T. Wu, Optics Express 20.13 (2012)
[8] J. B. Abshire, et al., Tellus B: Chemical and Physical Meteorology 62.5 (2010)

2021 27th International Semiconductor Laser Conference (ISLC) | 978-1-6654-4133-9/21/$31.00 ©2021 IEEE | DOI: 10.1109/ISLC51662.2021.9615662

SGDBR tunable laser on gallium arsenide for 1030 nm lidar applications

Paul Verrinder[1*], Lei Wang[1], Fengqiao Sang[1], Joseph Fridlander[1], Victoria Rosborough[1], Michael Nickerson[1], Guangning Yang[2], Mark Stephen[2], Larry Coldren[1], Jonathan Klamkin[1]

[1]*Electrical and Computer Engineering Department, University of California, Santa Barbara, CA 93106 USA*
[2]*NASA Goddard Space Flight Center, Greenbelt, MD 20771 USA*

*Email: pverrinder@ucsb.edu

Abstract – A sampled grating distributed Bragg reflector tunable laser with a center wavelength of 1032 nm is demonstrated on a gallium arsenide photonic integrated circuit platform. The laser demonstrates a 32 nm tuning range, 37 dB side-mode suppression ratio, and 20 mW of output power.

I. Introduction

Tunable semiconductor lasers are of interest for a variety of applications ranging from fiber optic telecommunications to light detection and ranging (Lidar) and free space optical communications [1-4]. Monolithic integration of tunable lasers with other optical devices (e.g., semiconductor optical amplifiers (SOAs), modulators, photodetectors) on photonic integrated circuit (PIC) platforms is highly desirable for reduction of overall system size, weight, and power (SWaP). This is particularly advantageous for air and space-borne systems where low SWaP is critical. Widely tunable lasers with sampled grating distributed Bragg reflector (SGDBR) mirrors have been demonstrated on indium phosphide (InP) PIC platforms for operation near 1550 nm [2-6]. However, there are applications outside this spectral range that could benefit from similar PIC technology. For example, airborne Lidar systems utilizing wavelengths near 1000 nm have applications in topographical measurements [7] and can take advantage of highly sensitive detectors at this wavelength [8]. In this work, we demonstrate an extended tuning range SGDBR laser on a gallium arsenide (GaAs) PIC platform for operation near 1030 nm.

II. Design and Fabrication

The SGDBR laser presented in this work is a four section laser with gain, phase, and front and back mirror sections. A sideview schematic is shown in Fig. 1(a), and a micrograph image of a fabricated device is shown in Fig. 1(b). The gain section consists of three layers of 5 nm thick indium gallium arsenide ($In_xGa_{1-x}As$) quantum wells (QWs) with $x = 0.271$, surrounded by gallium arsenide phosphide ($Ga_{1-x}AsP_x$) barriers with $x = 0.1$. GaAs waveguide layers are placed above and below the multi-quantum well (MQW) layers and surrounded by aluminum gallium arsenide ($Al_xGa_{1-x}As$) separate confinement heterostructure (SCH) layers, with low aluminum content (graded from $x = 0.1$-0.2). The lower n-type cladding is $Al_{0.75}GaAs$ and the upper p-type cladding is $Al_{0.6}GaAs$. Active-passive integration is accomplished with an offset quantum well (OQW) structure whereby the MQW is selectively removed with etching. This is followed by formation of the gratings and regrowth of the upper SCH and p-cladding layers by metalorganic chemical vapor deposition (MOCVD). This OQW structure creates gain regions integrated with passive waveguide sections for the phase section and grating mirrors, and the platform could be leveraged to realize more complex PICs as well.

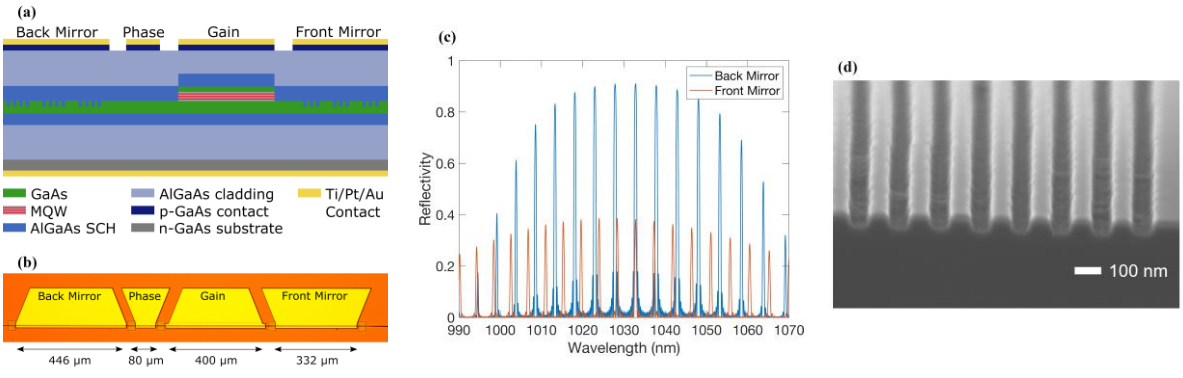

Fig. 1. (a) Schematic diagram of a four-section SGDBR laser and (b) top-view micrograph image of fabricated SGDBR laser. (c) Simulated reflectivity spectrum for front and back mirrors and (d) cross section SEM image of etched gratings.

Wavelength tuning is accomplished by injecting current into the front and back SGDBR mirrors [9]. Prior to regrowth, the gratings are patterned in the GaAs waveguide layer using electron beam lithography (EBL), and etched using inductively coupled plasma reactive ion etching (ICP-RIE) with chlorine (Cl_2) and nitrogen (N_2) chemistry. The grating pitch is 156 nm with 50% duty cycle and the etch depth is 35 nm, resulting in a calculated coupling coefficient for the un-sampled grating of $\kappa = 490\ \mathrm{cm}^{-1}$ and designed Bragg wavelength of 1032.8 nm. Figure 1(d) shows a cross section scanning electron microscope (SEM) image of the fabricated gratings prior to upper cladding regrowth. The total front mirror length is 332 µm with a sampling period of 33.163 µm and 10 grating periods per burst. Similarly, the back mirror is 446 µm long with a sampling period of 29.728 µm and 20 grating periods per burst. These mirrors result in the simulated reflectivity spectra shown in Fig. 1(c). Direct current injection in the mirror sections changes the refractive index and shifts the mirror spectra in Fig. 1(c) to select different modes, effectively tuning the laser's output wavelength.

III. Measurement Results

Figure 2(a) shows the light current voltage (LIV) characteristic of the SGDBR laser from Fig. 1(b). This laser demonstrates a threshold current of 22 mA and up to 20 mW output power from the front mirror (measured by coupling output to an integrating sphere) at 100 mA continuous wave (CW) current injection, without mirror tuning. Power output from the front mirror was then coupled to a lensed fiber and connected to an optical spectrum analyzer (OSA) to observe the laser's spectral output. Figure 2(c) shows a zoomed in view of the free running laser output spectrum with 100 mA applied to the gain section and no mirror or phase section current, demonstrating 37.17 dB side mode suppression ratio (SMSR) and a center wavelength of 1032.63 nm. Current applied to the front and back mirrors was then swept between 0 and 100 mA, while the gain section current was held constant at 100 mA. Figure 2(b) shows the output spectra at 8 different tuning current levels superimposed on one another, demonstrating a tuning range of 32 nm. The peaks above 1032 nm in Fig. 2(b) represent the output with only front mirror tuning, as the front mirror spectrum from Fig. 1(c) is shifted to longer wavelengths with applied current, while the back mirror spectrum remains constant. Similarly, the peaks below 1032 nm represent the laser output with only back mirror tuning. All of the spectra shown here were generated without phase section tuning.

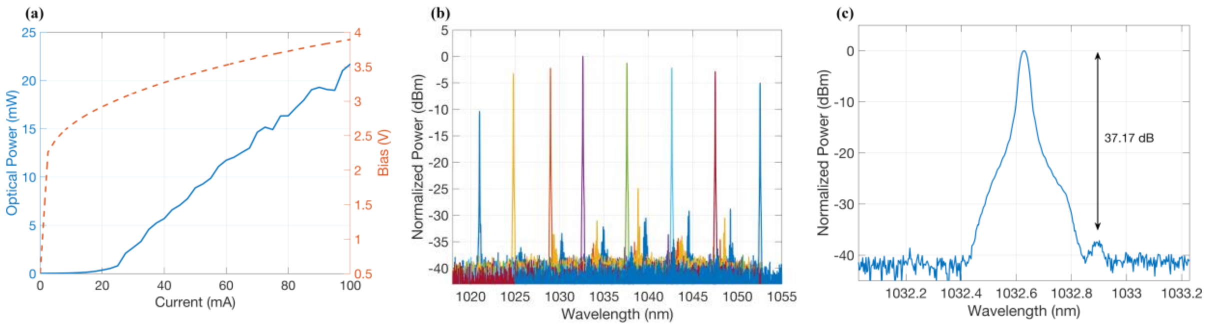

Fig. 2. (a) SGDBR laser LIV curve. (b) Tuning spectra at 8 different tuning mirror current levels and (c) close-up of free running laser spectrum showing 37.17 dB of SMSR and center wavelength 1032.63 nm.

IV. Conclusion

An extended tuning range SGDBR laser on GaAs was demonstrated with operation near 1030 nm, with a 32 nm tuning range, 37.17 dB SMSR, and up to 20 mW CW output power. To the best of the authors' knowledge, this is the first demonstration of a monolithically integrated, in-plane, extended tuning range laser for operation in this wavelength region on a GaAs PIC platform.

V. Acknowledgements

The authors acknowledge funding support from the NASA ESTO Advance Component Technology program. A portion of this work was carried out in the UC Santa Barbara Nanofabrication Facility.

VI. References

[1] L. A. Coldren *et al., J. Light. Technol.*, vol. 22, no. 1, pp. 193–202, 2004
[2] H. Zhao *et al.*, *IEEE J. Sel. Top. Quantum Electron.*, vol. 24, no. 6, pp. 1–6, 2018
[3] B. J. Isaac *et al.*, *IEEE J. Sel. Top. Quantum Electron.*, vol. 25, no. 6, pp. 1–7, 2019
[4] S. Arafin and L. A. Coldren, *IEEE J. Sel. Top. Quantum Electron.*, vol. 24, no. 1, 2018
[5] J. Fridlander, *et al,* Conference on Lasers and Electro-Optics (CLEO) 2020.
[6] V. Lal *et al.*, *J. Light. Technol.*, vol. 35, no. 7, pp. 1320–1327, 2017
[7] A. W. Yu *et al.*, Proc. SPIE 8599, 85990P (2013)
[8] M. A. Krainak *et al.*, *in Proc. SPIE Defense, Security, and Sensing,* Orlando, FL, USA, 2010
[9] V. Jayaraman *et al.*, *IEEE J. Quantum Electron.*, vol. 29, no. 6, pp. 1824–1834, 1993

Advanced Photonics Congress (IPR, Networks, NOMA, PVLED, SPPCom) © OSA 2021

Gallium Arsenide Photonic Integrated Circuit Platform for 1030 nm Applications

Paul Verrinder[1], Lei Wang[1], Joseph Fridlander[1], Fengqiao Sang[1], Victoria Rosborough[1], Michael Nickerson[1], Guangning Yang[2], Mark Stephen[2], Larry Coldren[1], Jonathan Klamkin[1]

Electrical and Computer Engineering Department, University of California, Santa Barbara, CA 93106 USA
NASA Goddard Space Flight Center, Greenbelt, MD 20771 USA
pverrinder@ucsb.edu

Abstract: An active-passive integration platform on GaAs is demonstrated with Fabry Perot lasers exhibiting up to 240 mW total output power, 98.8% injection efficiency, and 3.44 cm^{-1} active loss for operation near 1030 nm.

1. Introduction

Photonic integrated circuits (PICs) allow for the monolithic integration of both active photonic devices such as lasers, modulators, photodetectors, and amplifiers, as well as passive devices. PICs enable a significant reduction in system size, weight and power compared to systems constructed with discrete components. To date, indium phosphide (InP) is the most common PIC platform and is leveraged primarily for telecommunications and data center communications [1]. Recently, InP PICs have begun to impact other areas including free space laser communications, 3D mapping Lidar, and remote gas sensing Lidar [2-5]. Silicon photonics (SiPh) has also matured significantly for communications applications [2]. Outside of the 1310 nm and 1550 nm spectral ranges commonly used for telecommunications, there are other applications that could benefit from the advantages offered by PIC technology. The spectral region near 1000 nm, for example, is heavily utilized. One particular application of interest is airborne topographical Lidar where the form factor of PIC technology would enable deployment on small space platforms [6]. The focus of this work is the development of an active-passive integration platform on gallium arsenide (GaAs) for operation near 1030 nm. GaAs based lasers have been studied for many years, with indium gallium arsenide (InGaAs) quantum wells (QWs) being used for emission wavelengths in the 880-1100 nm range [7]. However, the primary focus in recent years, especially in the longer wavelengths greater than 1000 nm, has been on high power laser diodes or distributed feedback (DFB) and distributed Bragg reflector (DBR) lasers with surface etched gratings [8,9], rather than active-passive integration or widely tunable lasers. The work presented here demonstrates a technique for integrating 1030 nm InGaAs/GaAs QW Fabry Perot (FP) lasers with passive waveguides. This lays a foundation for future development of PIC technology operating near 1000 nm.

2. Material Design and Device Fabrication

The active region consists of three 5 nm $In_xGa_{1-x}As$ (x = 0.271) QWs surrounded by 8 nm $Ga_{1-x}AsP_x$ (x = 0.1) barriers, and GaAs separate confinement heterostructure (SCH) layers. The upper and lower cladding layers are $Al_xGa_{1-x}As$. Active-passive integration is accomplished by growing a partial structure that doesn't include the upper cladding, selectively removing the QW active layers, and then subsequently performing a regrowth of the upper p-cladding and p-contact layer by metalorganic chemical vapor deposition (MOCVD).

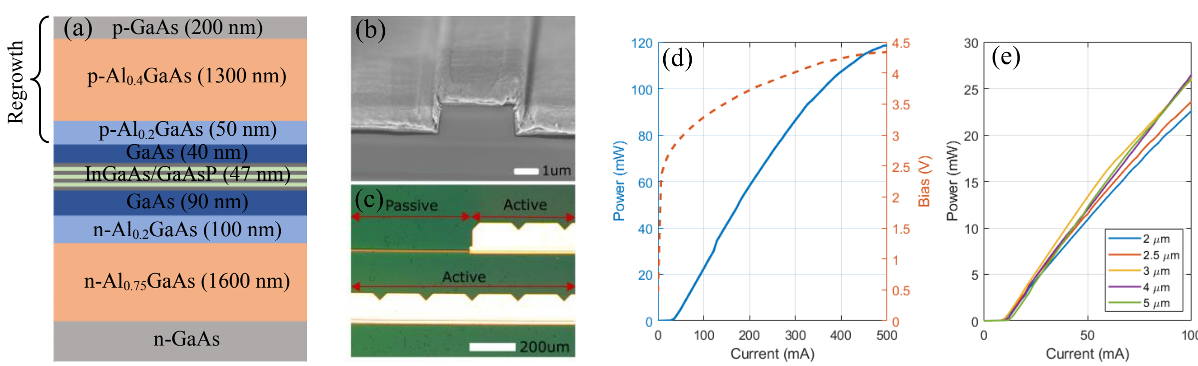

Fig. 1. (a) Layer structure in active section following regrowth. (b) SEM cross section of a cleaved facet 3 µm wide laser and (c) top view optical microscope image of active-passive and all-active FP lasers. (d) Power output from one side of 20x800 µm^2 broad area laser and (e) power from one side of 600 µm long narrow ridge 2-5 µm lasers.

Figure 1(a) reports the layer structure in the active section following regrowth. The QWs are placed closer to the top within the guiding layers, rather than in the middle, to minimize the height of the offset between the active and passive regions. This also allows for efficient optical coupling between the active and passive regions, while still allowing for sufficient overlap between the optical mode and the QWs in the active region. From simulations, the QW confinement factor, Γ_{QW}, is 5.02%, and 96% of the fundamental mode power is coupled from the active region to the passive region. Figures 1(b) and 1(c) show images of fully fabricated devices.

3. Measurement Results

Multiple lasers of varying widths were fabricated, including 20 μm wide broad area lasers, and 2 μm, 2.5 μm, 3 μm, 4 μm, and 5 μm narrow ridge devices with both active and passive sections. These devices were tested under both continuous wave (CW) and pulsed current operation to extract material parameters and device performance characteristics. Figures 1(d) and 1(e) show single sided light-current (LI) characteristics for the 20 μm broad area lasers, and for five different narrow ridge devices, respectively, under CW operation at room temperature. To extract internal loss and quantum efficiency, the broad area devices were tested under pulsed current operation (to mitigate self heating) for various cavity lengths. The inverse of the measured differential efficiency, η_d, is plotted as a function of cavity length with a linear curve fit in Fig. 2(a) to extract internal loss and injection efficiency values of 3.44 cm^{-1} and 98.8%, respectively. Similar measurements were obtained for active-passive FP lasers to extract a passive waveguide loss of 4.05 cm^{-1}. Figure 2(b) shows the spectral output of a 3 μm wide laser at several different CW current injection levels.

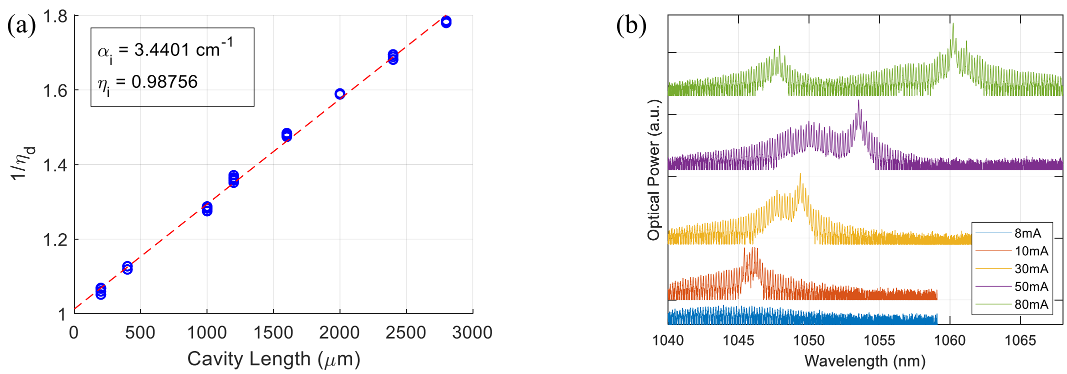

Fig. 2. (a) Inverse of measured differential efficiency as a function of cavity length for 20 μm broad area lasers. (b) Optical spectra under CW current injection for 3 μm wide lasers.

4. Conclusions

An active-passive GaAs PIC platform for 1030 nm operation has been demonstrated. FP lasers were integrated with passive waveguides, demonstrating up to 240 mW total power output from broad area devices, and greater than 50 mW out of narrow ridge devices at 100 mA CW current injection. These devices exhibit state-of-the-art laser performance characteristics with 3.44 cm^{-1} internal loss, 98.8% injection efficiency, 85.5 A/cm^2 transparency current density, and threshold current as low as 9 mA.

5. Acknowledgements

The authors acknowledge funding support from the NASA ESTO Advance Component Technology program.

6. References

[1] F. Kish, *et al.*, *Proc. IEEE*, vol. 101, no. 10, pp. 2255–2270, 2013
[2] J. Klamkin, *et al.*, *Opt. Express*, vol. 22, no. 2, p. 2150, 2014
[3] J. Fridlander, *et al,* Conference on Lasers and Electro-Optics (CLEO) 2020.
[4] H. Zhao *et al.*, *IEEE J. Sel. Top. Quantum Electron.*, vol. 24, no. 6, pp. 1–6, 2018
[5] B. J. Isaac, *et al, IEEE J. Sel. Top. Quantum Electron.*, vol. 25, no. 6, pp. 1–7, 2019
[6] A. W. Yu, *et al*, Proc. SPIE 8599, 85990P (2013)
[7] J. J. Coleman, *Journal on Selected Topics in Quantum Electronics,* vol. 6, no. 6, pp. 1008–1013, 2000
[8] A. Pietrzak, *et al,* Proc. SPIE 10900, 109000K (2019)
[9] S. Spieberger, *et al, Appl. Phys. B Lasers Opt.*, vol. 104, no. 4, pp. 813–818, 2011